A Particle-Surface-Area-Based Formulation of Heterogeneous Ice Nucleation by Mineral Dust Aerosols

Zur Erlangung des akademischen Grades eines

DOKTORS DER NATURWISSENSCHAFTEN

von der Fakultät für Physik des

Karlsruher Instituts für Technologie (KIT)

genehmigte

DISSERTATION

von

Diplom-Meteorologin Monika Niemand

aus Berlin

Tag der mündlichen Prüfung: 22.06.2012

Referent: Prof. Dr. Thomas Leisner

Korreferent: Prof. Dr. Joachim Curtius

This dissertation is dedicated to my family.

"The truth isn't easily pinned to a page. In the bathtub of history the truth is harder to hold than the soap, and much more difficult to find..."
— Terry Pratchett, *Sourcery*

Abstract

Mineral dust is one of the major components of the tropospheric aerosol. It is well known to initiate ice crystal formation in tropospheric clouds. Ice crystal formation affects cloud radiative properties and may initiate or enhance precipitation. In climate and weather models, the quantitative description of aerosol and cloud processes relies on simplified assumptions. This contributes major uncertainties to the prediction of global and regional climate change. Therefore, models need more advanced parameterizations for heterogeneous ice nucleation by atmospheric aerosols.

In this thesis, a new parameterization of immersion freezing on mineral dust aerosols, originating from desert areas, is derived from many experiments carried out at the AIDA cloud chamber facility of the Karlsruhe Institute of Technology. Ice-active surface site densities (n_s) are calculated using the the measured ice number concentration and particle surface area. An exponential function is fitted to n_s versus temperature. n_s takes values between $4 \cdot 10^6 \, \mathrm{m}^{-2}$ at $-12\,°\mathrm{C}$ and $9 \cdot 10^{11} \, \mathrm{m}^{-2}$ at $-36\,°\mathrm{C}$. This parameterization can be used to calculate the ice nuclei (IN) number concentration as a function of temperature and dust particle surface area. It is valid in the temperature range between $-12\,°\mathrm{C}$ and $-36\,°\mathrm{C}$ at or above water saturation. The new parameterization is applied to calculate distribution maps of IN during a Saharan dust event based on model results from the regional scale model COSMO-ART. The results are compared to measurements of IN and aerosol number concentrations at the Taunus Observatory on Mount Kleiner Feldberg, near Frankfurt am Main, Germany, during the dust outbreak. Additionally, the new parametrization is compared to three other parameterizations of heterogeneous ice nucleation during this event. The aerosol number and surface area concentration from the COSMO-ART model simulation are taken as input to the different parameterizations. Though the surface area from the model agrees well with aerosol measurements during the dust event at Kleiner Feldberg, the IN number concentration calculated from the new surface-area-based parameterization is about a factor of 13 less than IN measurements during the same event. Systematic differences of more than a factor of ten in the IN number concentration are also found

among the different parameterizations. Uncertainties in the modeled and measured parameters probably both contribute to this discrepancy.

Dust particles may be coated with organic species during long–range transports through the atmosphere. In this thesis, the effect of secondary organic aerosol (SOA) coating on the ice nucleation efficiency of desert dust particles is studied at the AIDA cloud chamber at mixed–phase and cirrus cloud temperatures. In the temperature range between –22 °C and –29 °C droplet formation occurs in each experiment with coated desert dust particles. Freezing is initiated as soon as water saturated conditions are reached. A suppression of the ice nucleation efficiency by the organic coating of more than a factor of two is observed in the experiments. A variability of more than a factor of ten in the freezing behavior is found among certain uncoated desert dusts. Therefore, the new parameterization can also be used to describe the average freezing behavior of SOA coated desert dust particles.

In the temperature range –39 °C to –45 °C, coated particles exhibit two distinct ice nucleation modes. A suppression of about a factor of two in the deposition mode ice nucleation by the SOA coating occurs in the range 110 % to about 135 % relative humidity with respect to ice. Close to water saturation the ice nucleation ability is enhanced due to water uptake of the water soluble SOA coating and the dust particles freeze via immersion freezing.

Contents

1. Introduction

Aerosols—tiny, airborne solid and liquid particles—from different natural and anthropogenic sources are distributed throughout the atmosphere and have a direct influence on climate as they interact with solar radiation via scattering and absorption. They impact indirectly on climate by affecting cloud formation and precipitation. Their impact strongly depends on their micro-physical properties, such as number concentration, size and shape. Their sizes range from nanometer to micrometer. Certain aerosol particles, such as mineral dust or certain biological particles, are capable of initiating ice crystal formation in clouds. Ice crystal formation is likely to initiate or enhance precipitation. It is subject of ongoing research to develop and improve formulations which can be used in cloud and climate models for calculating the abundance and variability of ice nuclei (IN) number concentration not only as a function of temperature and humidity, but also as a function of aerosol properties.

The scope of this thesis is the experimental investigation of atmospheric ice crystal formation by mineral dust aerosols, which is one of the most abundant aerosol species. For that, the large aerosol and cloud chamber AIDA[1] of the Karlsruhe Institute of Technology was applied. AIDA allows a realistic simulation of tropospheric and stratospheric cloud conditions covering a wide range of temperature and pressure. A parameterization which describes the ice nucleation of mineral dust aerosols was developed from the experimentally gained data for the application in cloud and climate models (chapter 4). Furthermore, the ice nucleation efficiency of chemically aged mineral dust was examined (chapters 5 and 6). The work is integrated in the framework of the Helmholtz Virtual Institute "Aerosol–Cloud–Interactions" coordinated by the Institute for Meteorology and Climate Research (IMK–AAF) at the Karlsruhe Institute of Technology.

---

[1] **A**erosol **I**nteractions and **D**ynamics in the **A**tmosphere

1.1. Background: ice nuclei and dust

Homogeneous and heterogeneous ice nucleation. Ice formation in the atmosphere can occur by homogeneous or heterogeneous nucleation (Pruppacher and Klett, 1997). Homogeneous ice nucleation denotes the spontaneous formation of ice from the water vapor or liquid water phase in the absence of solid particles. Homogeneous ice nucleation from the water vapor phase does not occur in the atmosphere, since it requires very high (up to several hundred percent) supersaturations (Pruppacher and Klett, 1997). Homogeneous freezing of water droplets in the absence of any solid phase occurs at temperatures below $-36\,°\mathrm{C}$ (Figure 1.1 (a)).

(a) homogeneous freezing

(b) deposition nucleation

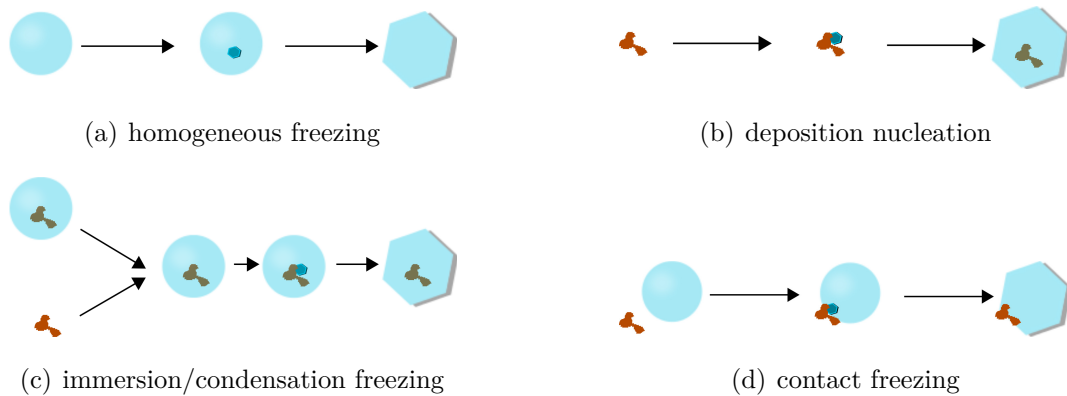(c) immersion/condensation freezing

(d) contact freezing

Figure 1.1.: Ice formation mechanisms. (a) illustrates the homogeneous freezing mechanisms, which occurs in the absence of any solid phases below $-36\,°\mathrm{C}$. (b)–(c) illustrates the heterogeneous nucleation mechanisms, which occur in the presence of solid particles.

Heterogeneous ice nucleation takes place in the presence of ice nuclei (IN), a minor fraction of the tropospheric aerosol, which exhibit specific surface structures to facilitate the formation of ice crystals at higher temperatures and lower supersaturations than required for homogeneous freezing. With IN present, clouds below $0\,°\mathrm{C}$ can start to develop the ice phase. Heterogeneous ice nucleation can occur either through the direct deposition of water from the vapor phase to the dry solid particle surface, at ice supersaturated conditions and below water saturation (Figure 1.1 (b)), or by the freezing of a supercooled liquid phase in contact with the ice nucleus (heterogeneous freezing modes). Three heterogeneous freezing modes are distinguished (Vali, 1985): immersion freezing, condensation freezing and contact freezing. In the immersion freezing mode, the ice nucleus is already immersed in the supercooled liquid when freezing happens (Figure 1.1 (c), upper path). In the condensation freezing mode,

the ice nucleus acts as a cloud condensation nucleus (CCN) and an ice nucleus at almost the same time, and at the same temperature (Figure 1.1 (c), lower path). In the contact freezing mode, freezing is induced by the collision of an aerosol particle with the droplet surface (Figure 1.1 (d)). In addition to the described primary ice formation processes, ice can also be formed by secondary ice formation processes such as rime–splintering (Hallett and Mossop, 1974; Pruppacher and Klett, 1997).

Ice nuclei in the atmosphere. A large variety of different aerosol particles can act as ice nuclei and initiate the ice-phase in atmospheric clouds. Besides mineral dust and volcanic ash particles, also some biological particles (bacteria, pollen and fungi) are capable of serving as IN in tropospheric clouds (Després et al., 2012). Properties that are known to affect IN efficiency are water insolubility, "large" sizes (typically larger than the Aitken[2] size mode, thus greater $0.1\,\mu m$), chemical features, crystallographic features and surface shape (Pruppacher and Klett, 1997). Atmospheric ice nuclei are far less abundant than atmospheric CCN, which initiate cloud droplet formation. Their number concentration is typically a few IN per standard liter at temperatures down to $-20\,°C$, and their occurrence is highly variable in space and time (Pruppacher and Klett, 1997; DeMott et al., 2010). However, their impact on cloud properties and climate is significant. For example, more IN in mid-level clouds increase the number concentration of ice crystals that grow at the expense of liquid water droplets (Wegener–Bergeron–Findeisen process). This mechanism together with the secondary ice formation mechanisms mentioned above may initiate or enhance precipitation (DeMott et al., 2010). Furthermore, an increase in IN number concentration at high altitude cirrus clouds may lead to a net warming effect, by lowering the threshold for ice formation, leading to the development of more cirrus clouds (e.g. DeMott et al., 2010). The sign and magnitude of these effects is not yet sufficiently quantified as emphasized within the Intergovernmental Panel on Climate Change (IPCC, AR4) (Denman et al., 2007).

Dust in the atmosphere. Large desert areas in Northern Africa (Sahara, Bodélé Depression) and Asia (Taklimakan, Gobi) are known as major source areas of atmospheric dust particles (Goudie and Middleton, 2001; Prospero et al., 2002; Tegen, 2003). The amount of dust emitted into the air is estimated to range from $1500\,Tg$ yr^{-1} to $2600\,Tg\,yr^{-1}$ (Forster et al., 2007; Shao et al., 2011). Though desert dust is emitted in extremely dry air, a trajectory analysis by Wiacek et al. (2010) demonstrated that a significant fraction of dusty air masses originating from African and

---

[2]John Aitken (1839–1919), Scottish physicist and meteorologist.

Asian desert areas experience cloud formation conditions after some time of transport and lifting in the troposphere, thereby acting as CCN and IN (Karydis et al., 2011; Twohy et al., 2009; Hoose et al., 2008; Stith et al., 2009). In situ measurements and Lidar studies have demonstrated a link between long–range transported Saharan dust and ice formation in tropospheric clouds (DeMott et al., 2003; Sassen et al., 2003; Ansmann et al., 2008). Klein et al. (2010) measured increased IN number concentrations during a Saharan dust event at the Taunus Observatory on Mount Kleiner Feldberg, near Frankfurt am Main, Germany. In addition, Chou et al. (2011) found that the IN number concentration increases at the high alpine research station Jungfraujoch during Saharan dust events by as much as one order of magnitude, depending on the intensity of the dust event. Aerosol particles originating from deserts or other dry areas are typically composed of a complex mixture of particle sizes, particle morphologies and mineral phases (Schütz and Sebert, 1987; Kandler et al., 2007, 2009). Various mineral particles have been found as residual particles of evaporated cirrus ice crystals (Heintzenberg et al., 1996; Twohy and Poellot, 2005; Targino et al., 2006), and dust particles have been identified as the most abundant type of IN processed from anvil cirrus residual particles (Prenni et al., 2007).

Laboratory measurements of dust IN. The role of mineral dust particles as IN in mixed–phase and cirrus clouds was also investigated in numerous laboratory studies (e.g. Koehler et al., 2010; Welti et al., 2009; Kanji et al., 2008; Möhler et al., 2006) with different experimental techniques, all showing that mineral dust aerosols are very efficient IN in the immersion freezing and deposition nucleation modes. It is also confirmed by numerous studies (e.g. Hung et al., 2003; Zuberi et al., 2002; Knopf and Koop, 2006), that mineral dusts immersed in supercooled liquid solution droplets initiates ice formation at humidities well below that required for homogeneous freezing. In most cases the mineral dust surrogate Arizona test dust (ATD, cf. chapter 3.4) or pure clay minerals, such as montmorillonite, kaolinite or illite were investigated for their ice nucleation ability. Ice nucleation studies on natural Asian dust (AD) and Saharan dust (SD) samples have recently been performed at the AIDA cloud simulation chamber by Möhler et al. (2006), Field et al. (2006), and Connolly et al. (2009). The AIDA cloud simulation chamber is also applied in this thesis and will be introduced in chapter 3. Möhler et al. (2006) investigated the deposition mode ice nucleation efficiency of AD, SD and ATD in the temperature range –50 °C to –77 °C. They found ATD particles to be more efficient than AD and SD. Field et al. (2006) found no difference in the nucleation behavior of SD and AD in the temperature range

–19.7 °C to –53.2 °C. At temperatures higher than –40 °C, both dusts nucleated ice through the immersion freezing mode only. Connolly et al. (2009) investigated the immersion freezing of AD, SD and ATD at temperatures between –12 °C and –33 °C, with ATD being the most efficient freezing nuclei, followed by AD and SD. Koehler et al. (2010) applied a continuous flow diffusion chamber (CFDC) to measure ice nucleation on SD, a Canary Island Dust and ATD in the temperature range –20 °C to –65 °C. They observed the dusts to nucleate ice through the deposition mode at temperatures below –40 °C. At temperatures warmer than –36 °C the dust samples required droplet activation before ice formation. Size-dependence of mineral dust particles on the ice nucleation efficiency in the cirrus cloud and mixed–phase cloud temperature regime was explicitly investigated by, e.g. Archuleta et al. (2005), Welti et al. (2009) and Kanji and Abbatt (2010). They all showed that larger sized particles nucleated ice most efficiently, i.e. small particles require lower temperatures and higher ice supersaturations than larger ones.

Parameterizations of heterogeneous ice nucleation. Simple and widely used parameterizations of heterogeneous ice nucleation are a function of temperature (e.g. Fletcher, 1962), or ice supersaturation (e.g. Meyers et al., 1992). Recently, several different types of parameterizations have been developed for the use in cloud and climate models, relating the probability of heterogeneous ice nucleation to aerosol properties, by assuming proportionality to aerosol particle number concentration (e.g. DeMott et al., 2010), or more commonly, to the available aerosol surface area concentration (e.g. Phillips et al., 2008; Hoose et al., 2010; Niemand et al., 2012). Some parameterizations (e.g. Zobrist et al., 2007; Hoose et al., 2010) are based on classical nucleation theory (see chapter 2.2), some are based upon empirical relations from field measurements (e.g. Phillips et al., 2008; DeMott et al., 2010), or laboratory measurements (e.g. Connolly et al., 2009; Niemand et al., 2012). Parameterizations of heterogeneous ice nucleation, derived from laboratory measurements, are based on experiments with different dust types. This leads to different results when applied in cloud and climate models. The use of different materials to derive parameterizations of heterogeneous ice nucleation, and also the way it is described—either based on thermodynamic considerations or by a fit to the observations—was found to have a great influence on the total indirect aerosol effect (see chapter 2.2 for the different formulations of heterogeneous ice nucleation). For example, Lohmann and Diehl (2006) performed sensitivity simulations with a global climate model. They assumed that dust is entirely composed of the less ice-active kaolinite or the more ice-active montmorillonite clay mineral,

respectively. They found significant implications for the total indirect aerosol effect. The net radiation at the top of the atmosphere varied between $1 \pm 0.3\,\mathrm{W\,m^{-2}}$ and $2.1 \pm 0.1\,\mathrm{W\,m^{-2}}$ in their simulations. Yun and Penner (2012) compared the effect of different parameterizations on the top of the atmosphere cloud radiative forcing in a global atmosphere model. They implemented the parameterization by Meyers et al. (1992) and the aerosol specific parameterizations by Phillips et al. (2008) and Young (1974). Depending on the parameterization used, they found changes of up to $8.73\,\mathrm{W\,m^{-2}}$ in the net solar flux and up to $3.52\,\mathrm{W\,m^{-2}}$ in the net longwave flux at the top of the atmosphere, respectively.

Coatings. The atmospheric aerosol is composed of a mixture of insoluble and soluble substances. This leads to the conclusion, that long–range transported atmospheric dust aerosols can get coated with various substances. Field experiments (e.g. Levin et al., 1996; Falkovich, 2004) support this assumption. Laboratory studies investigated the effect of various coatings on the ice nucleation ability of mineral dust particles (Möhler et al., 2008; Eastwood et al., 2009; Cziczo et al., 2009; Niedermeier et al., 2010; Sullivan et al., 2010), all showing that chemical processing can in some cases lower the IN ability. Large amounts of particulate matter are organics, either directly emitted at the ground or, to a large extend, formed in the atmosphere as so-called secondary organic aerosol (SOA) by the chemical conversion of volatile organic precursor gases (Jimenez et al., 2009; Hallquist et al., 2009). Möhler et al. (2008) investigated the effect of SOA coating on the deposition mode ice nucleation efficiency of ATD and the clay mineral illite at cirrus cloud conditions in the AIDA cloud chamber. They found that the ice nucleation efficiency was notably suppressed by the SOA coating.

1.2. Objectives and outline of the thesis

There is a need for better understanding the thermodynamic conditions required for ice crystal formation by atmospheric aerosols in order to predict their effects on cloud and climate properties. The AIDA aerosol and cloud simulation chamber is a unique facility to investigate ice crystal formation under atmospherically relevant and repeatable conditions. Most laboratory ice nucleation studies were conducted on mineral dust surrogates and pure clay minerals. Only a few studies investigated the ice nucleation efficiency of natural desert dust samples. These studies were conducted at temperatures lower than –20 °C. Parameterizations derived from these measurements

are limited to these lower temperatures and an extrapolation to higher temperatures is uncertain. Moreover, very few studies address the effect of organic coatings on the ice nucleation efficiency of natural desert dust samples. The objective of this thesis, is summarized in the following points

(1) Investigation of the immersion freezing behavior of natural desert dust aerosols over a wide range of temperatures in the AIDA aerosol and cloud chamber.

(2) Deriving a new parameterization of immersion freezing on desert dust particles on the basis of AIDA laboratory experiments.

(3) Application of the new parameterization.

(4) Investigation of secondary organic aerosol coating on the ice nucleation efficiency of desert dust particles at mixed–phase and cirrus cloud temperatures.

Chapter 2 presents two different approaches of describing the heterogeneous ice nucleation, namely the classical nucleation theory and the so-called ice-active surface site density approach. **Chapter 3** gives an introduction to the AIDA cloud simulation chamber, its instrumentation and operation principle. The dust samples used in this thesis are introduced, and the coating procedure with secondary organic aerosol is described. **Chapter 4** presents experiments of immersion freezing on desert dust aerosols. This is the most complete data set obtained during this thesis. Based on these results, a parameterization of immersion freezing is derived and applied to calculate distribution maps of ice nuclei number concentration based on model results from the regional scale model COSMO-ART during a Saharan dust event. The results are compared to measurements of ice nuclei and aerosol number concentrations at the Taunus Observatory on Mount Kleiner Feldberg and to other ice nucleation parameterizations applied to the same dust event. Moreover, a comparison of the new parameterization to literature data is presented. **Chapter 5** and **chapter 6** present experiments conducted on SOA coated desert dust particles in the mixed–phase cloud and cirrus cloud temperature regime, respectively. Finally, **chapter 7** gives an outlook, including some recommendations for future scientific work in this field.

2. Formulations of Heterogeneous Ice Nucleation

In this chapter the ice nucleation process that leads to the formation of ice crystals is presented (section 2.1). Concepts for the description of heterogeneous ice nucleation include the classical nucleation theory and the so-called ice-active surface site density approach. They will be described in sections 2.2 and 2.3, respectively.

2.1. The ice nucleation process

Ice nucleation in the atmosphere begins with the formation of an ice cluster, reaching the critical size for stability. Small clusters, below the critical size, have a tendency to evaporate, whereas large clusters, above the critical size, prefer to grow. The reason for this is the surface to volume ratio, that decreases with increasing cluster size. Only molecules at the cluster surface can escape from it. Therefore, the larger the number of water molecules inside the cluster, the less it is affected by random molecular fluctuations at the cluster surface. As the cluster becomes stable and continues to grow by diffusion, eventually forming a macroscopic ice crystal (Vali, 1999, homogeneous nucleation case). The presence of solid particles facilitates ice nucleation, by providing surfaces onto which water molecules can attach, thereby increasing the probability for the formation of a stable ice cluster (Vali, 1999, heterogeneous nucleation case).

There are different approaches available for the description of heterogeneous ice nucleation. The nucleation process is either based on thermodynamic considerations where the process of ice cluster formation is treated stochastically in the first place (classical theory, section 2.2), or it is assumed that ice nucleation is dominated by the availability and characteristics of ice-active nucleation sites (ice-active surface site density approach, section 2.3). In the latter case, it is still assumed that the process of cluster formation is stochastic.

2.2. Classical theory for heterogeneous ice nucleation

The classical theory for heterogeneous ice nucleation (Pruppacher and Klett, 1997; Seinfeld and Pandis, 2006; Lamb and Verlinde, 2011) accounts for the stochastic nature of the nucleation process which is time-dependent described by a nucleation rate. The governing factor is the temperature-dependent nucleation rate coefficient, j_{het} in m^{-2} s^{-1}. It is expressed as

$$j_{het}(T) = A_{het} \exp \left(\frac{-\Delta G^* f_{het}}{k_B T} \right).$$
(2.1)

k_B is the Boltzmann constant, and has a value of $1.381 \cdot 10^{-23}$ J K^{-1}. A_{het} is a pre-exponential factor and has units of m^{-2} s^{-1}. ΔG^* is the free energy, which is needed to form a critical ice nucleus. f_{het} is the factor that accounts for the presence of a solid particle. Assuming a spherical ice cap and neglecting the curvature of the solid particle, f_{het} depends on the contact angle θ between the particle's surface and the ice nucleus. $f_{het}(\theta)$ can be expressed as

$$f_{het}(\theta) = \frac{1}{4}(2 + \cos \theta)(1 - \cos \theta)^2$$
(2.2)

f_{het} takes values between 0 and 1. For a contact angle of $0\,°$, thus $f_{het} = 0$, there is no free-energy barrier of cluster formation, that has to be overcome. The nucleation process starts as soon as ice supersaturated conditions are reached. For a contact angle of $180\,°$, thus $f_{het} = 1$, the homogeneous and heterogeneous nucleation can occur with equal probabilities. A_{het} and ΔG^* take different expressions depending on the nucleation mechanism—nucleation from the vapor or liquid phase, respectively. Different expressions for A_{het} and ΔG^* are for instance given by Fletcher (1958), Zobrist et al. (2007), Chen et al. (2008), Fornea et al. (2009) and Barahona (2011).

The basic form of the classical theory describes the nucleation process by a single contact angle θ. The assumption of a probability distribution function (PDF; Marcolli et al., 2007; Lüönd et al., 2010) of contact angles takes the particle to particle variability into account. Nevertheless, θ is difficult to measure and validate, e.g. θ can only be measured on a microscopic scale and is therefore not transferable to the molecular scale. In addition, it is not realistic to assume that the shape of ice nucleus is a spherical cap.

Furthermore, the particle surface area is treated as energetically homogeneous, i.e. the probability of forming an ice nucleus is equally distributed across the surface of

the particle. In truth, the ice nucleation preferentially occurs at certain active sites (Pruppacher and Klett, 1997).

The classical theory describes heterogeneous ice nucleation incomplete. The required parameters are difficult to specify and the underlying assumptions are uncertain or unrealistic.

2.3. Ice-active surface site density approach

According to the ice-active surface site density approach, the ice nucleation process is dominated by the availability and characteristics of ice-active nucleation sites. These sites are equally distributed over the dust particle surface area. Ice nucleation is initiated instantaneously as soon as a characteristic supercooling or relative humidity with respect to ice is reached. There is no time-dependence and therefore no dependence on the cooling-rate. This means, that no further ice nucleation will occur if the temperature is held constant. Ice nucleation from the liquid phase is dominated by the change in temperature, e.g. the ice-active surface site with the lowest temperature threshold determines the freezing temperature of the droplet. Thus, freezing nucleation depends on temperature only. In the case of deposition mode nucleation, the determining factor is the relative humidity with respect to ice, and to a minor extend the change in temperature.

The number of frozen particles or droplets N_i can be described in general terms by (e.g. Connolly et al., 2009)

$$N_i = N_{tot}\{1 - \exp[-S_{ae}n_s]\}. \tag{2.3}$$

N_{tot} is the total number of particles, or droplets in the case of freezing nucleation. S_{ae} is the surface area of an individual particle. n_s is number of ice-active surface sites per unit area.

n_s can be expressed for freezing nucleation (n_s^{freeze}) and deposition nucleation (n_s^{dep}) as (Connolly et al., 2009)

$$n_s^{freeze}(T) = \int_T k_{freeze}(\tau)d\tau \quad \text{or} \quad n_s^{dep}(RH_i, T) = \int_{RH_i}\int_T k_{dep}(\rho, \tau)d\rho d\tau \tag{2.4}$$

with

$$k_{freeze}(T) = \frac{dn_s(T)}{dT} \quad \text{and} \quad k_{dep}(T, RH_i) = \frac{dn_s(T, RH_i)}{dT dRH_i}.$$

In the case of immersion freezing, n_s, describes the density of ice-active surface sites that become active as the temperature T is lowered. In the case of deposition mode ice nucleation n_s is a function of relative humidity, RH_i, and T.

Surface densities of active sites in relation to contact freezing and deposition nucleation were first discussed by Young (1974). DeMott (1995) applied the surface site density concept to quantify the heterogeneous ice nucleation activity in the deposition mode. Connolly et al. (2009) suggested parameterization for immersion freezing by desert dust particles using this approach. It was also discussed and used by Niedermeier et al. (2010), Lüönd et al. (2010), Murray et al. (2011) and Broadley et al. (2012).

This straightforward approach can be easily applied in cloud and climate models, however, in some cases the time-dependence of the ice nucleation process cannot be ignored. But from a large number of AIDA expansion experiments there is evidence that the formation of ice is mainly related to the total temperature change and the particle surface area. This concept will be used in the following as a measure for the ice nucleation ability of certain aerosol particles and to derive a parameterization for the immersion freezing by desert dust particles in chapter 4. At first the experimental setup is described (chapter 3).

3. Experimental Methods

In this chapter, the aerosol and cloud chamber AIDA (section 3.1) and the instrumentation (section 3.2), used for the ice nucleation studies in this thesis, are described. Furthermore, a typical AIDA expansion experiment is presented (section 3.3). The different dust samples used in this thesis are introduced in section 3.4. Ice nucleation experiments were also conducted on coated desert dust particles. The coating procedure is described in section 3.5.

3.1. The AIDA cloud simulation chamber

Figure 3.1 shows a schematic of the AIDA aerosol and cloud chamber and the instrumentation used in this thesis. It was used and described before by, e.g. Möhler et al. (2003), Möhler et al. (2006) and Wagner et al. (2006). The central part of the AIDA cloud chamber facility is a large, evacuable vessel with a volume of $84\,\mathrm{m}^3$, which can be used as an expansion chamber for ice nucleation studies. It can be evacuated from atmospheric pressure to less than $0.01\,\mathrm{hPa}$ by two mechanical pumps. The pumps can be operated at different pumping speeds, thus allowing a well controlled and repeatable simulation of cooling rates in the range of $0.1\,\mathrm{K\ min}^{-1}$ to $6.0\,\mathrm{K\ min}^{-1}$. This corresponds to updraft velocities of about $0.15\,\mathrm{ms}^{-1}$ to $8\,\mathrm{ms}^{-1}$ in natural wave clouds or convective clouds. The cylindrical shaped aluminum chamber is encased in a large thermally insulated box which can be cooled down to about $-35\,^\circ\mathrm{C}$ with a conventional chiller. Further cooling to a minimum temperature of $-90\,^\circ\mathrm{C}$ is achieved by the evaporation of liquid nitrogen inside the heat exchangers. A mixing fan is installed near the chamber bottom to ensure homogeneous conditions during the experiments. The temperature is measured at different heights inside the AIDA cloud simulation chamber by vertically aligned, calibrated thermocouples. The maximum deviation between the thermocouples is $0.3\,\mathrm{K}$ at the highest pumping speed. The wall temperature is measured with another set of thermocouples attached to the chamber walls. The AIDA mean gas temperature T_g corresponds to the average temperature measured by

the thermocouples. At constant pressure and temperature prior to a cloud expansion experiment, almost ice saturated conditions in the cloud chamber (typically about 90 % to 95 % relative humidity with respect to ice) are maintained by a thin ice layer on the chamber walls. According to Möhler et al. (2003), the thin ice layer ($\sim$2 µm) is accomplished by cooling the chamber walls to 0 °C, evacuating the chamber volume to 0.01 hPa with the two mechanical pumps, refilling the chamber with clean and dry synthetic air to about 5 hPa and evacuating it again. After another flushing and filling cycle, a certain amount of deionized water is added to the cloud simulation chamber. It is refilled to atmospheric pressure, then it is cooled to the temperature of interest. Water vapor condenses onto the chamber walls, if the wall temperature drops below the frost point temperature. The thin ice layer is a source of water vapor during the cloud expansion experiment. The chamber volume is not saturated with respect to ice prior to the expansion start, due to T_g, which is slightly higher than the wall temperature. The reason for this are internal heat sources inside the AIDA cloud simulation chamber, such as heated sampling tubes and the mixing fan.
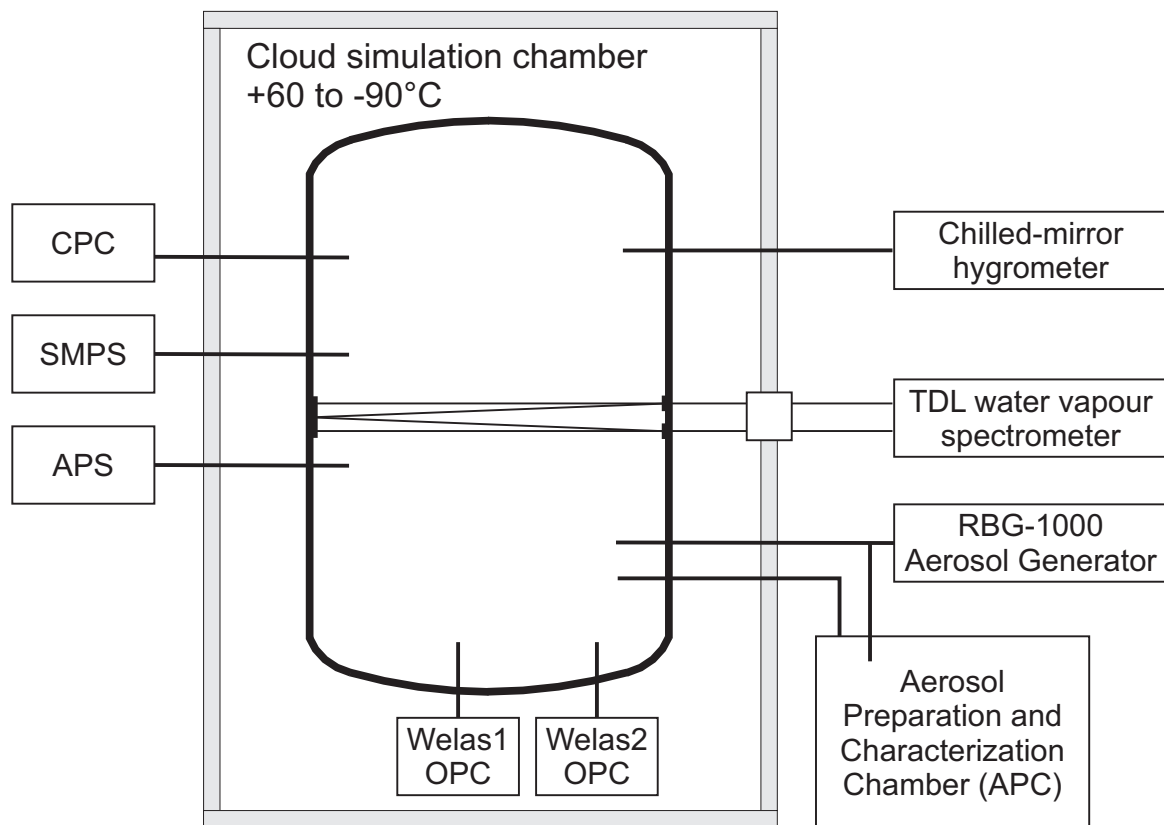

Figure 3.1.: Schematic of the AIDA cloud simulation chamber and instrumentation.

The APC (aerosol preparation and characterization) chamber has a volume of $3.7\,\mathrm{m}^3$ and is directly connected to the AIDA cloud simulation chamber through a connection tube. The APC is typically used to prepare the aerosol. A mixing fan in the APC chamber homogeneously mixes the volume. After aerosol generation and characterization, part of the aerosol can be transferred from the APC chamber into the AIDA cloud simulation chamber for the expansion cloud experiment.

3.2. Instrumentation

Dust samples are introduced into the chamber using a **rotating brush generator RBG–1000** (Palas GmbH, Karlsruhe, Germany) which is operated with dry and clean synthetic air. The rotating brush disperses a certain amount of particles from a particle reservoir. The fine particles are de-agglomerated in an aerosol dispersion nozzle. After this step, large particles are removed from the aerosol with a cyclone impactor operated with a $50\,\%$ cut–off between about $1\,\mu\mathrm{m}$ and $5\,\mu\mathrm{m}$. The particles are then transported with the air flow into the chamber. For a few experiments presented in this thesis (chapter 4.1, indicated in Table 4.2), no cyclone was used in order to generate aerosols with larger particles for the cloud experiments. In this case, particles larger than about $10\,\mu\mathrm{m}$ were still removed by settling and inertial losses of particles in the tube connection between the dust generator and the cloud chamber.

The total particle number concentration in the AIDA cloud simulation chamber is measured with a **condensation particle counter** (CPC3010, TSI Inc., USA). The CPC3010 has been modified and calibrated to continuously detect and count particles at reduced pressures in the range from 100 to $1000\,\mathrm{hPa}$ (see Seifert et al., 2004). The particles in the sample flow are enlarged by the condensation of butanol during its operation, allowing to count particles as small as $10\,\mathrm{nm}$. In some experiments the ultrafine condensation particle counter (UCPC3776, TSI Inc., USA) is additionally applied to count particles prior to the expansion cloud experiment. The UCPC3776 has a lower particle detection size limit of $2.5\,\mathrm{nm}$.

A **scanning mobility particle sizer** (SMPS, TSI Inc., USA) and an **aerodynamic particle sizer** (APS, TSI Inc., USA) measure the number size distribution of the aerosol sample before each cloud expansion experiment. The SMPS measures a mobility diameter[1] d_m in the particle size range $14\,\mathrm{nm}$ to $820\,\mathrm{nm}$. The APS sizes

---

[1]The mobility diameter is defined as that of a spherical particle having the same electrical mobility as the particle in question (John, 2011).

particles based on their aerodynamic diameter[2] d_a in the size range 0.5 µm to 20 µm. To compare the results of the two instruments, d_m measured by the APS and d_a measured by the SMPS are converted into a volume–equivalent sphere diameter[3] d_p through the following relationships (Hinds, 1999):

$$d_p = \frac{d_m}{\chi} \quad \text{and} \quad d_p = \sqrt{\frac{\chi \rho_0}{\rho}} d_a. \tag{3.1}$$

χ is the is the dynamic shape factor and takes the non-sphericity of the particle shape into account. ρ is the particle density and ρ_0 is the unit density of $1\,\text{g cm}^{-3}$.

The combined size distribution measurements from the SMPS and APS are best described by monomodal or bimodal log-normal fits. A log-normal distribution is defined as:

$$\frac{dN}{d \log d_p} = \frac{N_{tot}}{\sqrt{2\pi} \log \sigma} \exp\left[-\frac{1}{2}\left(\frac{\log d_p - \log d_N}{\log \sigma}\right)^2\right] \tag{3.2}$$

where N_{tot} is the total aerosol number concentration and σ the geometric standard deviation.

A **tunable diode laser** (TDL) absorption spectrometer is applied for the in situ measurement of the water vapor pressure with an accuracy of $\sim 5\,\%$ (Ebert et al., 2005; Fahey et al., 2009). The saturation vapor pressure formulations of Murphy and Koop (2005) are used to calculate the relative humidity with respect to ice (RH_i) and water (RH_w) using the AIDA mean gas temperature T_g and the measured water vapor pressure e_{TDL}:

$$RH_i = \frac{e_{TDL}}{e_{i,sat}} \cdot 100 \quad \text{and} \quad RH_w = \frac{e_{TDL}}{e_{w,sat}} \cdot 100,$$

with

$$e_{i,sat} = \exp[9.550426 - 5723.265/T_g + 3.53068 \ln(T_g) - 0.00728332 \ T_g];$$
$$T_g > 110 \ K,$$

and

$$e_{w,sat} \approx \exp\{54.842763 - 6763.22/T_g - 4.210 \ \ln(T_g) + 0.000367 \ T_g$$
$$+ \tanh[0.0415 \ (T_g - 218.8)][53.878 - 1331.22/T_g$$
$$- 9.44523 \ \ln(T_g) + 0.014025 \ T_g]\}; \quad 123 \ K < T_g < 332 \ K.$$

---

[2]The aerodynamic diameter is defined as that of a spherical particle of unit density having the same gravitational settling velocity as the particle in question (John, 2011).

[3]The volume–equivalent sphere diameter is defined as that of a sphere with the same volume as the particle in question Kulkarni et al. (2011).

Additionally, the total water concentration is measured with a **chilled–mirror hygrometer** (373LX, MBW Calibration, Switzerland). This accurate absolute measurement for total water is compared to the TDL absorption spectrometer in cloud–free situations, showing good agreement between the two instruments within $1\,\%$ to $2\,\%$.

Two **welas[4] optical particle counters** (Palas GmbH, Karlsruhe, Germany) are used to detect and count cloud droplets and ice crystals (Benz et al., 2005; Benz, 2006). The detection volume of the welas is illuminated with white light. The particles scatter light while they fly through the sensor. The number concentration of particles can be determined from the number of light pulses per time interval, the puls intensity gives information about the size of the particle (Palas, 2008). The number concentration of particles per unit volume detected by the welas, N^{welas}, is calculated using the velocity v of particles moving through the detection volume within a time interval Δt:

$$N^{welas} = \frac{n_a}{\Delta t \overline{v} A_{dv}} \tag{3.3}$$

A_{dv} is the cross-sectional area of the detection volume ($280\,\mu\mathrm{m} \times 280\,\mu\mathrm{m}$ for welas1 and $493\,\mu\mathrm{m} \times 493\,\mu\mathrm{m}$ for welas2) and n_a the number of particles detected (number of counts). Δt is chosen to be $5\,\mathrm{s}$ to reduce noise. This means that the number concentration of particles is calculated for every $5\,\mathrm{s}$ from the number of counts in this time interval. The welas calibration is based on the refractive index of water. The detection size ranges of the two instruments are $0.3\,\mu\mathrm{m}$–$46\,\mu\mathrm{m}$ (welas1) and $4\,\mu\mathrm{m}$–$237\,\mu\mathrm{m}$ (welas2), respectively. Ice crystals are distinguished from droplets and interstitial aerosol by their optical diameter[5]. In the analysis, a size threshold, which varies among the experiments, is set so that the number of all particles with sizes above the threshold can be used to calculate the number concentration of ice crystals, using Eq. 3.3. Since the saturation vapor pressure over liquid water is greater than over ice at the same temperature, liquid water droplets evaporate in the presence of ice crystals. The ice crystals grow quickly at the expense of the liquid water droplets (Wegener-Bergeron-Findeisen process). For example, at liquid water saturation, the diffusional growth rate of an ice crystal with a radius of $5\,\mu\mathrm{m}$ is about $0.9\,\mu\mathrm{m}\,\mathrm{s}^{-1}$ in radius at $-15\,^\circ\mathrm{C}$ (see Appendix A.1 for more details).

---

[4]white–light aerosol spectrometer system

[5]The optical diameter is defined as that of a calibration particle having the same response in an instrument that detects particles by their interaction with light, as the particle in question (John, 2011).

3.3. AIDA expansion experiments

Each AIDA cloud expansion experiment starts with a reference expansion, where the background aerosol is activated to droplets or ice crystals and precipitated from the cloud chamber. After aerosol generation and characterization, the expansion cycle is started by slow pumping. Figure 3.2 depicts a typical AIDA expansion experiment with a Saharan dust sample (section 3.4) starting at a temperature of –19.3 °C (experiment ACI04_10). Time 0 s corresponds to the start of the expansion cooling. The pressure p starts to decrease after time 0 s (panel 1). The chamber volume cools adiabatically at first (panel 2). The wall temperature T_w stays nearly constant throughout the experiment, because of its high heat capacity. Due to the heat flux from the warmer chamber walls, T_g deviates from the adiabatic profile ($T_{adiabatic}$, blue dashed line in panel 2) after some time as $T_w - T_g$ increases. The initial adiabatic change in temperature due to the pressure drop is described by

$$\frac{dT_g}{dp} = \frac{R_a}{c_{pa}} \frac{T_g}{p} \tag{3.4}$$

where $c_{pa} = 1005 \, \text{J kg}^{-1} \, \text{K}^{-1}$ is the specific heat capacity of air and $R_a = 287 \, \text{J kg}^{-1}$ K^{-1} is the specific gas constant for dry air.

Shortly after the start of the expansion, the relative humidity with respect to ice, RH_i, exceeds the ice saturation line (panel 3). After about 90 s, the air becomes saturated with respect to water and droplets start to form. N_{tot}^{welas1} in panel 4 equals the total number concentration of cloud droplets after cloud formation. Ice forms shortly after droplet activation by immersion freezing (N_i^{welas1} and N_i^{welas1} in panel 4). A vertical black line in each panel represents the onset of ice formation. As long as the droplets persist, RH_w should be close to 100 %. In the experiments where droplets are formed, RH_w is observed to be about 5 % below water saturation. This systematic deviation can be caused by a slight offset in the temperature measurement due to the condensation of water vapor on the temperature sensors or by inhomogeneities especially close to the chamber walls which lead to lower calculated average humidity compared to the regions where cloud droplets are present. In the following time series of immersion freezing experiments, the relative humidity is corrected by 5 % in order to match water saturated conditions during the presence of water droplets in the cloud chamber. Additionally, the relative humidity calculated from the frost point temperature, measured with the chilled–mirror hygrometer (section 3.2), is shown. MBW_i and MBW_w compare well to the relative humidity from the TDL measurement (section 3.2) before droplet and ice formation.

The pumping stops at about 480 s and 750 hPa in this experiment. The temperature starts to increase again, due to the heat flux from the warmer chamber walls. The relative humidity decreases and the droplets and ice crystals evaporate.
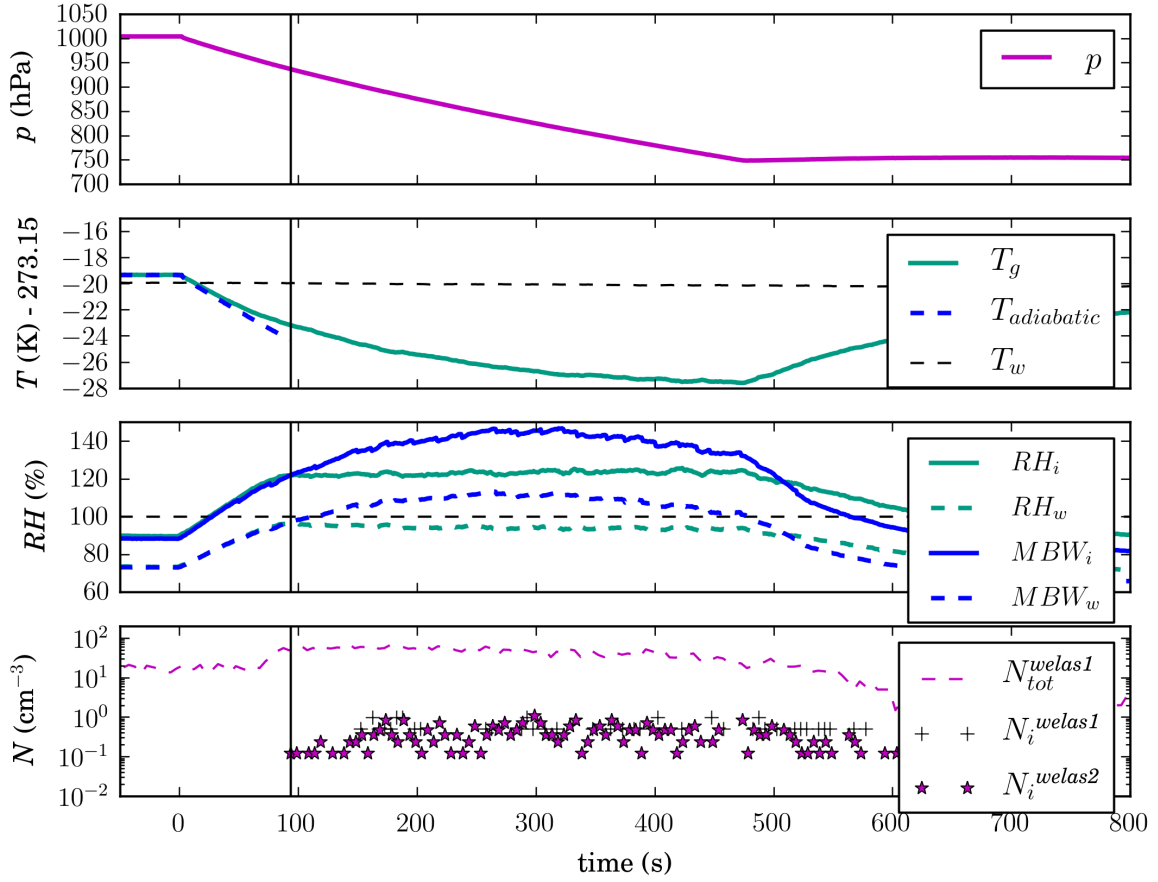

Figure 3.2.: Typical AIDA expansion experiment (experiment ACI04_10). The initial temperature is –19.3 °C. **Panel 1**: pressure p; **panel 2**: gas temperature T_g, adiabatic temperature $T_{adiabatic}$, wall temperature T_w; **panel 3**: relative humidity with respect to water (RH_w) and ice (RH_i), relative humidity calculated from the frost point temperature measured with the chilled–mirror hygrometer, MBW_w and MBW_i; **panel 4**: number concentration of ice crystals N_i^{welas1} and N_i^{welas2}. N_{tot}^{welas1} is the total number concentration measured by the welas1 and equals the total number concentration of cloud droplets after cloud formation. The vertical black line in each panel indicates the starting point of ice formation.
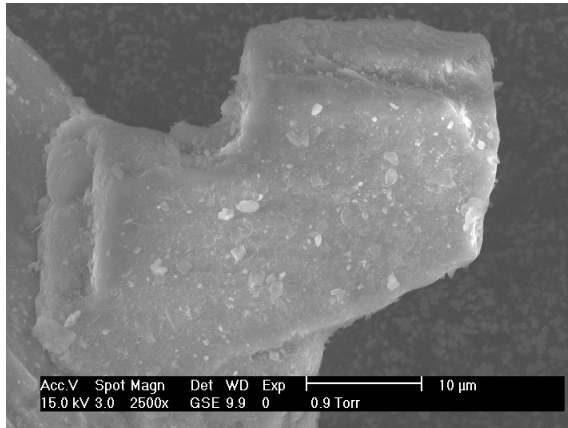
3.4. Dust samples

The ice nucleation of five different dust samples is examined in this thesis - Asian dust (AD), Saharan dust (SD), Canary island dust (CID), Israel dust (ID), and Arizona test dust (ATD). The origins of the dust samples are listed in Table 3.1. AD, SD, CID, and ID were collected from the surface. They are samples of natural origin and are considered to be representative for atmospheric dust. ATD (Powder technology Inc., Minnesota, USA) is a commercially available, milled reference dust material with a nominal 0–3 µm particle diameter size range (Möhler et al., 2006).

Table 3.1.: Dust types and origin of samples.

| Dust	Origin
AD	soil sample collected in the easterly parts of the Takla Makan Desert in China, provided by Lothar Schütz, University of Mainz, Germany
SD	soil sample collected about 50 km north of Cairo city, Egypt
CID	soil sample collected near the town of Mala on the Canary Island of Lanzarote
ID	collected as sedimented particles after a dust storm in Israel, provided by Prof. Eli Ganor, Tel Aviv University
ATD	milled reference dust material, Powder Technology Inc., Minnesota, USA

The AD, SD, CID and ID samples are sieved, but not chemically or otherwise processed, to obtain a sub-fraction with particle diameters smaller than 75 µm which is used for aerosol generation. Figure 3.3 shows environmental scanning electron microscope (ESEM) images of AD, SD, ID and ATD. Whereas the images of AD, SD and ATD are from the bulk sample, ID was sampled on a Nuclepore® filter directly from the AIDA cloud simulation chamber and than viewed with the ESEM. The image of the AD sample shows small particles in the order of less than 2 µm attached to a larger chunk. The AD and SD sample have rather smooth surfaces, the ID particles are agglomerates of small grains as large as 1 µm. The ATD particles are characterized by sharp edges.
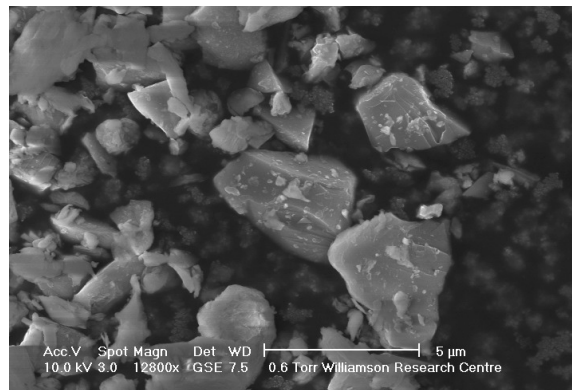
(a) Asian dust
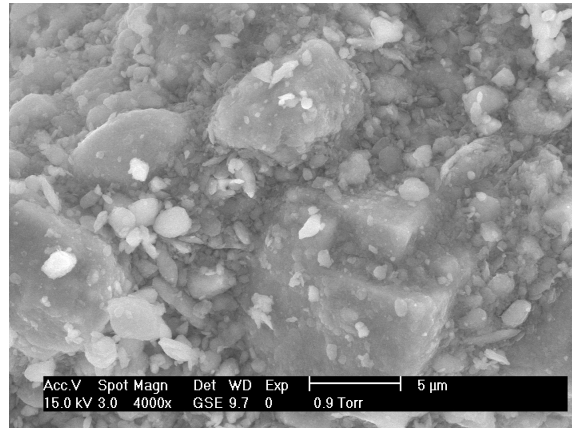
(b) Saharan dust
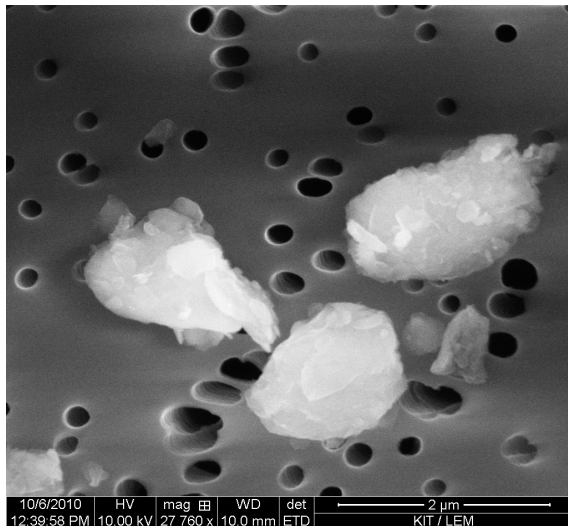
(c) Israel dust

(d) Arizona test dust

Figure 3.3.: Representative ESEM images of dust samples used in this thesis (courtesy to Dr. Frank Friedrich (KIT-IFG) for images (a) and (b), to Dr. Alexei Kiselev (KIT-IMK-AAF) for image (c) and to Dr. Rachel Burgess (The University of Manchester) for image (d)).

3.5. Coating procedure

Ice nucleation experiments were conducted on desert dust particles coated with secondary organic aerosol (SOA) compounds. In the following, the coating procedure is described. The results from the experiments with coated dusts will be discussed in chapters 5 and 6.

The dust particles are coated with secondary organic aerosol compounds at room temperature in the APC or at lower temperatures directly in the AIDA cloud simulation chamber at atmospheric pressure. The SOA coating procedure was induced by the ozonolysis reaction of α–pinene. First, ozone is added to the dark chamber and second, a certain amount of α–pinene. Ozone is always added in excess to the α–pinene. This ensures a complete conversion of α–pinene to the SOA products (Möhler et al., 2008). The SOA yield, i.e. the ratio of the SOA mass (µg m^{-3}) produced to the mass of α–pinene reacted, is calculated using the parameterization presented in Saathoff et al. (2009) who investigated the formation of SOA from the ozonolysis of α–pinene in the temperature range –30 °C to 40 °C. The SOA yield is mainly a function of the amount of α–pinene added to the chamber and temperature. In principle, the lower the temperature at which the aerosol is coated, the larger is the SOA yield for the same amount of α–pinene added.

The condensation of the SOA onto the desert dust particles occurs in the transition from the kinetic regime to the diffusion regime. In the kinetic regime, this means for particles smaller than the gas mean free path, the diameter growth rate of the SOA layer is influenced by the rate of random molecular collisions of vapor molecules and is independent of the size of the particles (Hinds, 1999). On the other hand, for particles larger than 0.5 µm to 1 µm the growth rate becomes inversely proportional to the radius (diffusion regime). It can therefore be assumed that the coating thickness decreases with particle size.

4. Immersion Freezing on Desert Dust Particles

The AIDA cloud simulation chamber (chapter 3.1) was applied to investigate the immersion freezing on desert dust particles in the temperature range –10 °C to –28 °C. Section 4.1 presents two typical immersion freezing experiments starting at an initial temperature of about –20 °C and –10 °C, respectively. The results of the immersion freezing experiments are presented in section 4.2. A new parameterization of immersion freezing on desert dust particles is derived (section 4.2.2). This new parameterization is applied to a Saharan dust outbreak (section 4.3) which was simulated with the COSMO-ART regional scale model (section 4.3.1). In section 4.3.2, the new parameterization is applied to calculate distribution maps of ice nuclei. Measurements of ice nuclei number concentrations and size distributions were obtained during the time of the dust event (section 4.3.3). In section 4.3.4, the calculated IN number concentration is compared to the measurements and to other concepts (section 4.3.5). The results are summarized in section 4.5. The results of this chapter have been published in Niemand et al. (2012).

4.1. AIDA immersion freezing experiments

The immersion freezing on desert dust particles was investigated in the AIDA cloud simulation chamber (chapter 3.1) during the International Workshop on Comparing Ice Nucleation Measuring Systems (ICIS07) in September 2007 (Nicolet et al., 2010; Koehler et al., 2010; Kanji et al., 2011; Jones et al., 2011) and during the Aerosol-Cloud Interaction campaign ACI04 in September/October 2010. The dust samples, namely Asian dust (AD), Saharan dust (SD), Canary island dust (CD), Israel dust (ID), and Arizona test dust (ATD), are introduced in chapter 3.4. Table 4.1 lists the different dust types and the investigated temperature ranges (cf. Table 3.1, chapter 3.4).

Table 4.1.: Dust types and respective temperature ranges.

Dust	Origin	Temperature range
Asian dust (AD)	soil sample	–10 °C to –28 °C
Saharan dust (SD)	soil sample	–10 °C to –28 °C
Canary island dust (CD)	soil sample	–18 °C to –23 °C
Israel dust (ID)	sedimented particles after a dust storm	–10 °C to –28 °C
Arizona test dust (ATD)	dust surrogate	–17 °C to –22 °C

An overview of all immersion freezing experiments presented and discussed in this chapter is given in Table 4.2. It tabulates experiment number, date, and dust type, the pressure p_0 and temperature T_0 prior to the start of each experiment, the temperature range that is covered in the experiment, the initial total particle number concentration N_{tot}, and total particle surface area concentration S_{tot}. N_{tot} is obtained from the CPC3010 measurement (chapter 3.2), S_{tot} is calculated from the log-normal fit to the surface size distribution (chapter 3.2 and section 4.2.1) before the start of the experiment.

The desert dust particles were dispersed with the rotating brush generator RBG–1000 and a dispersion nozzle into a flow of dry synthetic air (see chapter 3.2). The resulting dust aerosol was then passed to the AIDA cloud simulation chamber either directly or through cyclone impactors for removing larger particles. Direct transfer without cyclone impaction enhanced the abundance of larger dust particles and therefore also enhanced the aerosol surface area concentration during the AIDA ice nucleation experiments (see Table 4.2).

Figure 4.1 shows an AIDA immersion freezing experiment (experiment ACI04_22) with ID starting at an initial temperature of –19.6 °C and atmospheric pressure (Figure 4.1, panel 1). The pumping expansion starts at $t = 0$ s. The gas temperature T_g decreases, while the wall temperature T_w stays nearly constant (Figure 4.1, panel 1). The experiment starts at nearly ice saturated conditions (RH_i in Figure 4.1, panel 2). The initial relative humidity with respect to water (RH_w) is about 80 %. Due to the cooling expansion RH_i exceeds 100 % after a few seconds. Water saturated conditions ($RH_w = 100$ %) are reached after about 75 s. The relative humidity is corrected by 5 % in order to match water saturated conditions during the presence of water droplets in

the cloud chamber (cf. chapter 3.3).

The total particle number concentration N_{tot} is shown in panel 3 of Figure 4.1. It is calculated from the initial CPC3010 value (chapter 3.2) measured before the expansion start multiplied by the pressure dilution p/p_0, assuming a constant particle mixing ratio in the course of the experiment. The direct CPC3010 measurement is not shown here, because it is affected by particle losses in the unheated sampling tube after droplet activation. Droplets and ice crystals are measured by the two optical particle counters welas1 and welas2 (chapter 3.2). The total particle number concentration measured by welas1 (N_{tot}^{welas1} in Figure 4.1, panel 3) increases by the formation of liquid droplets as soon as RH_w reaches the cloud condensation nucleation threshold for the dust particles. After the liquid cloud formation, N_{tot}^{welas1} equals the total number concentration of cloud droplets. In the experiments discussed in this chapter all dust particles acted as cloud condensation nuclei (CCN) within the measurement uncertainty of $\pm 30\,\%$. This is because the cooling rates were sufficiently high for the peak supersaturation to exceed the value required for all particles larger than a few tenths of a micron to activate as droplets. Shortly after droplet formation, ice crystals form via immersion freezing (N_i^{welas1} and N_i^{welas2} in Figure 4.1, panel 3). Particles are detected as ice crystals when they grow to an optical diameter larger than a certain size threshold which is set individually for each experiment so that interference with cloud droplet sizes is avoided (chapter 3.2). Panel 4 of figure 4.1 shows the size distribution over time of growing droplets and ice crystals from welas1 and welas2. The size threshold is set to $d_p = 30\,\mu$m in this experiment.

Figure 4.2 shows the AIDA time series for the immersion freezing experiment ACI04_37 with SD starting at an initial temperature of –9.8 °C and atmospheric pressure. The air gets saturated with respect to ice and water shortly after the start of the pumping expansion (RH_i and RH_w reaching or exceeding $100\,\%$ in panel 2). At about $t = 50$ s N_{tot}^{welas1} increases due to the formation of droplets (panel 3). Only a few ice crystals form via immersion freezing (panel 3 and panel 4). The calculation of the ice number concentration (chapter 3.2) is partly based on only one count in panel 3. Therefore, the ice number concentration is averaged in each experiment over a time period of minimum 60 s for further analysis, as described in the next section 4.2.

Table 4.2.: Overview of immersion freezing experiments and respective experimental conditions. p_0 and T_0 are the pressure and temperature inside the chamber at the start of the experiment. N_{tot} is the total number concentration and S_{tot} the total surface area concentration of dust particles prior to the experiment. T_{range} is the temperature range covered by the expansion run. It is indicated whether a cyclone impactor was used to cut-off larger particles.

| Exp. No.	Date	Dust	p_0 (hPa)	T_0 (K) − 273.15	T_{range} (K)	N_{tot} (cm⁻³)	S_{tot} (μm² cm⁻³)	Cyclone	Comments
ACI04_13	1 Oct 2010	AD	1003.3	−10.0	−8.0	173.3	109.2	yes	no ice
ACI04_16	1 Oct 2010	AD	1002.8	−14.3	−8.1	238.3	130.0	yes	freezing
ACI04_19	4 Oct 2010	AD	990.1	−20.1	−8.0	218.2	156.4	yes	freezing
ACI04_04	29 Sep 2010	SD	1007.5	−9.1	−7.9	127.8	145.9	yes	no ice
ACI04_37	7 Oct 2010	SD	1008.2	−9.8	−5.6	114.8	248.6	no	freezing
ACI04_07	30 Sep 2010	SD	1005.5	−14.1	−8.0	173.9	189.2	yes	freezing
ACI04_34	6 Oct 2010	SD	999.4	−14.8	−7.7	138.2	309.2	no	freezing
ICIS07_20	25 Sep 2007	SD	1005.7	−16.4	−4.4	396.8	98.5	yes	freezing
ACI04_10	30 Sep 2010	SD	1003.9	−19.3	−8.2	121.8	110.2	yes	freezing
ICIS07_23	26 Sep 2007	CID	1002.0	−18.4	−5.1	381.8	59.1	yes	freezing
ACI04_25	5 Oct 2010	ID	995.7	−9.8	−7.5	695.6	576.7	yes	freezing
ACI04_40	7 Oct 2010	ID	1007.9	−9.4	−7.9	739.5	1229.7	no	freezing
ACI04_28	5 Oct 2010	ID	996.4	−14.4	−6.6	655.4	514.6	yes	freezing
ACI04_31	6 Oct 2010	ID	1000.9	−15.0	−7.8	766.5	1333.9	no	freezing
ACI04_43	8 Oct 2010	ID	1007.1	−15.0	−8.3	526.6	922.5	no	freezing
ICIS07_17	24 Sep 2007	ID	1005.1	−16.8	−6.6	253.8	110.3	yes	freezing
ACI04_22	4 Oct 2010	ID	989.2	−19.6	−7.9	252.1	165.5	yes	freezing
ICIS07_03	17 Sep 2007	ATD	1000.9	−16.8	−4.9	950.0	328.0	yes	freezing
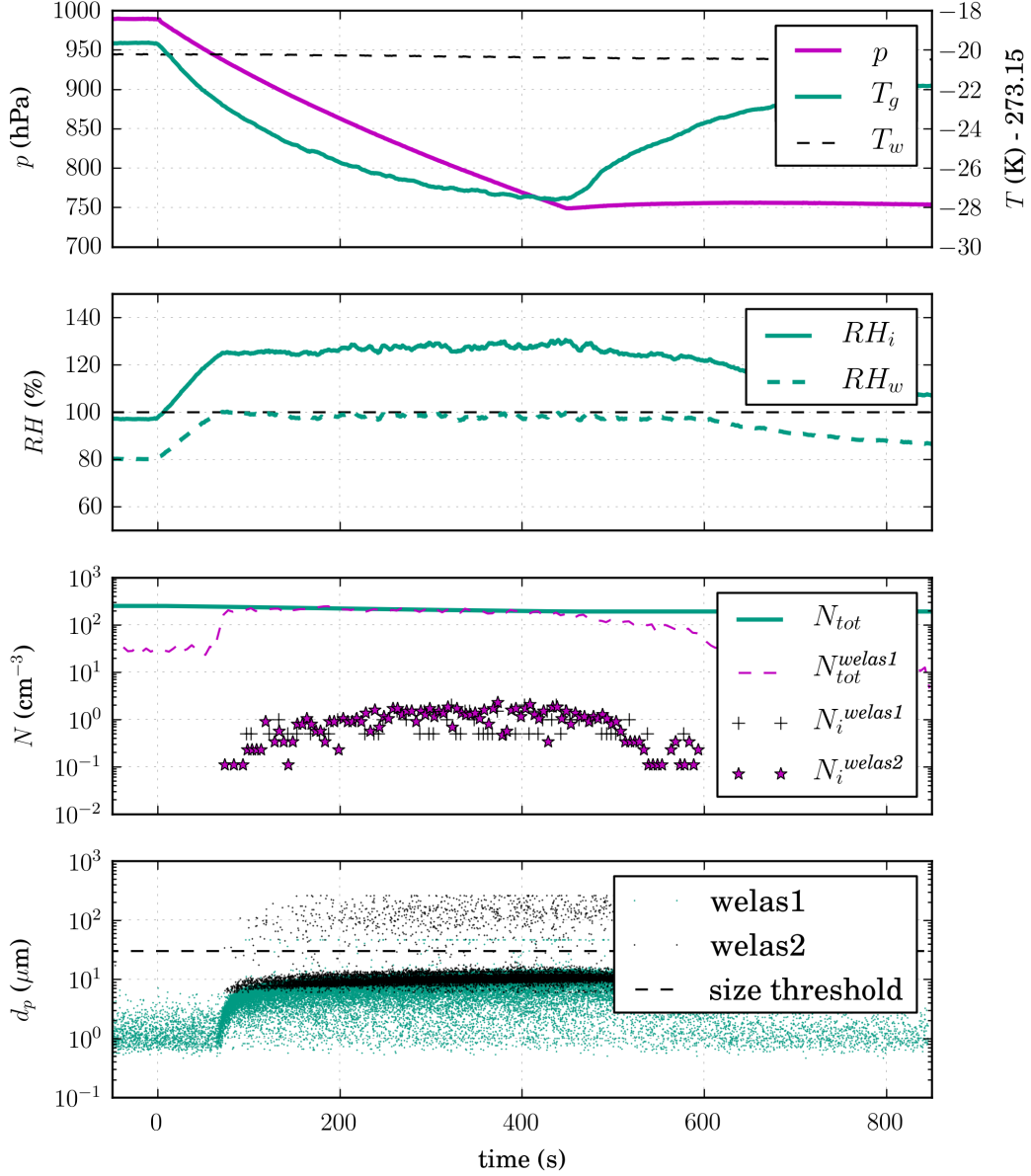
Figure 4.1.: AIDA expansion experiment (experiment ACI04_22) with Israel dust (ID). Initial temperature is –19.6 °C. **Panel 1**: pressure p, wall temperature T_w, gas temperature T_g; **panel 2**: relative humidity with respect to water (RH_w) and ice (RH_i); **panel 3**: number concentration of total aerosol N_{tot} and ice crystals N_i^{welas1} and N_i^{welas2}. N_{tot}^{welas1} equals the total number concentration of cloud droplets after cloud formation at about 75 s; **panel 4**: particle size distribution with size threshold between droplets and ice crystals at $d_p = 30\,\mu$m. See section 4.1 for more details.
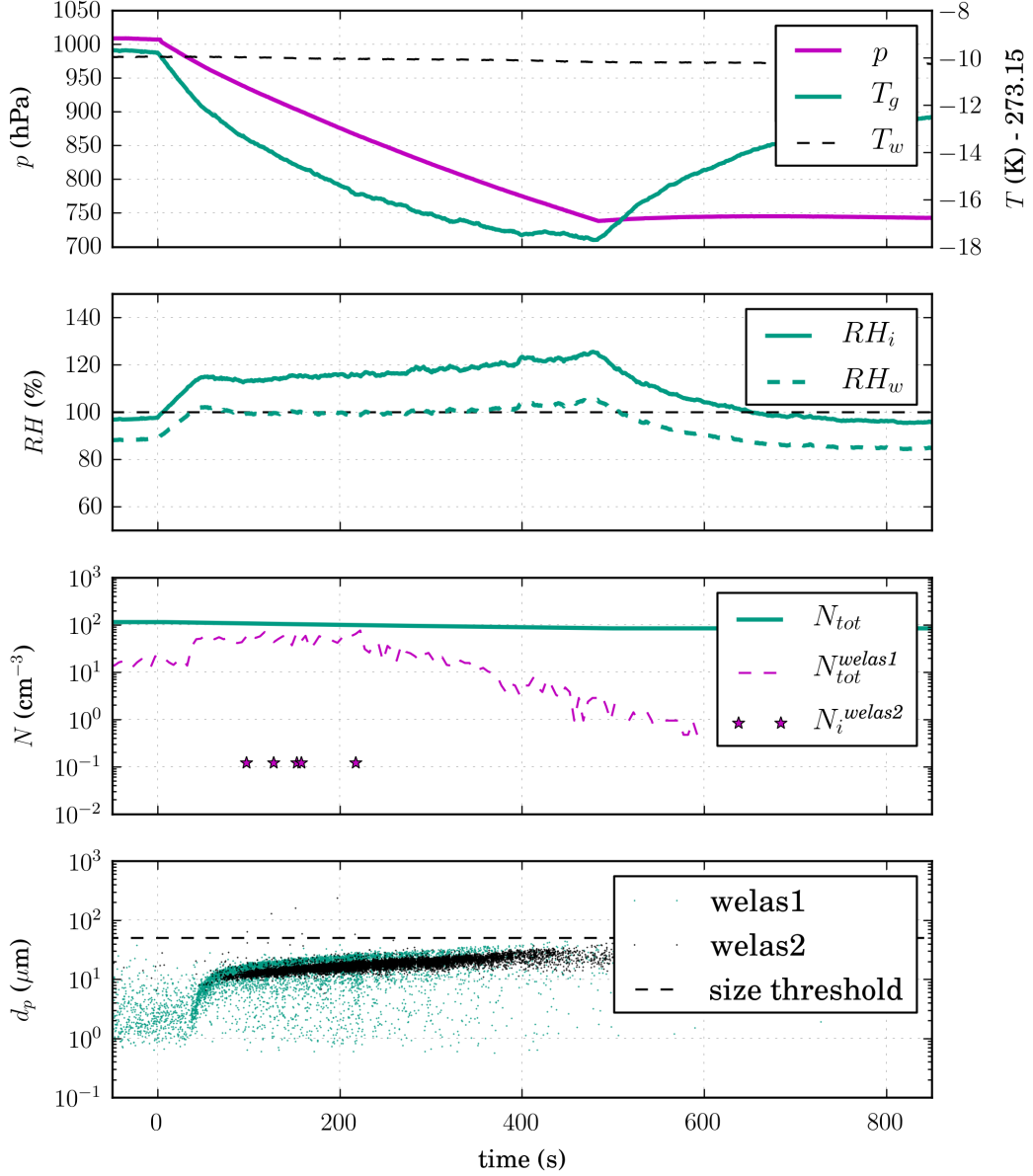
Figure 4.2.: AIDA expansion experiment (experiment ACI04_37) with Saharan dust (SD). Initial temperature is –9.8 °C. **Panel 1**: pressure p, wall temperature T_w, gas temperature T_g; **panel 2**: relative humidity with respect to water (RH_w) and ice (RH_i); **panel 3**: number concentration of total aerosol N_{tot} and ice crystals N_i^{welas1} and N_i^{welas2}. N_{tot}^{welas1} equals the total number concentration of cloud droplets after cloud formation at about 50 s; **panel 4**: particle size distribution with size threshold between droplets and ice crystals at $d_p = 50\,\mu$m. See section 4.1 for more details.

4.2. Immersion freezing results

In the following, the ice-active particle fractions f_i, calculated for all immersion freezing experiments listed in Table 4.2 are presented. Surface size distributions will be shown in section 4.2.1. The measured ice number concentrations and total particle surface areas will be used to derive a parameterization of immersion freezing on desert dust particles in section 4.2.2.

Figure 4.4 depicts f_i versus decreasing temperature. f_i is calculated from the ice number concentration from the welas2 instrument, N_i^{welas2}, divided by N_{tot}. The reason for using the welas2 data only, is the higher sensitivity of this instrument compared to welas1. For the calculation of f_i, N_i^{welas2} is averaged over a 60 s time period, making sure that at least 4 ice crystals are counted in this time interval. Otherwise, the time interval is increased until this condition is satisfied, leading to a larger range of corresponding temperature for this data point. The averaging procedure starts at droplet formation and continues as long as N_i^{welas2} is significantly increasing, resulting in up to 5 values of N_i per experiment (Figure 4.3).
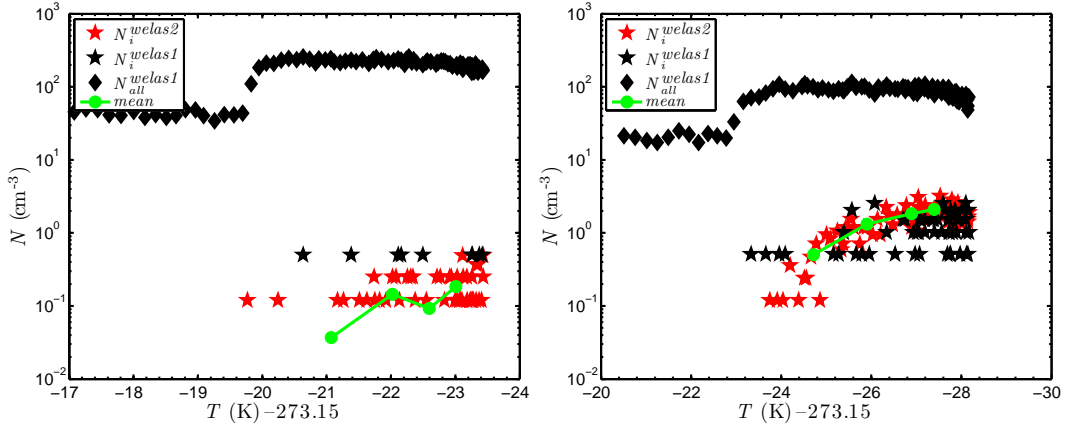
(a) Experiment starting at $T = -16.8\,°C$. (b) Experiment starting at $T = -20.1\,°C$.

Figure 4.3.: Number concentration of droplets and ice versus decreasing temperature. Droplets are represented by black diamonds after droplet activation at about $-20\,°C$ in (a) and $-24\,°C$ in (b), respectively. The green curve in (a) and (b) represents the minimum 60 s averages of N_i^{welas2} (red stars) for experiments ICIS07_17 (with ID) and ACI04_19 (with AD). See chapter 4.2.

The vertical error bars in Figure 4.4 represent a factor of two estimated uncertainty in f_i. This includes mainly the uncertainty of the number concentration of large ice
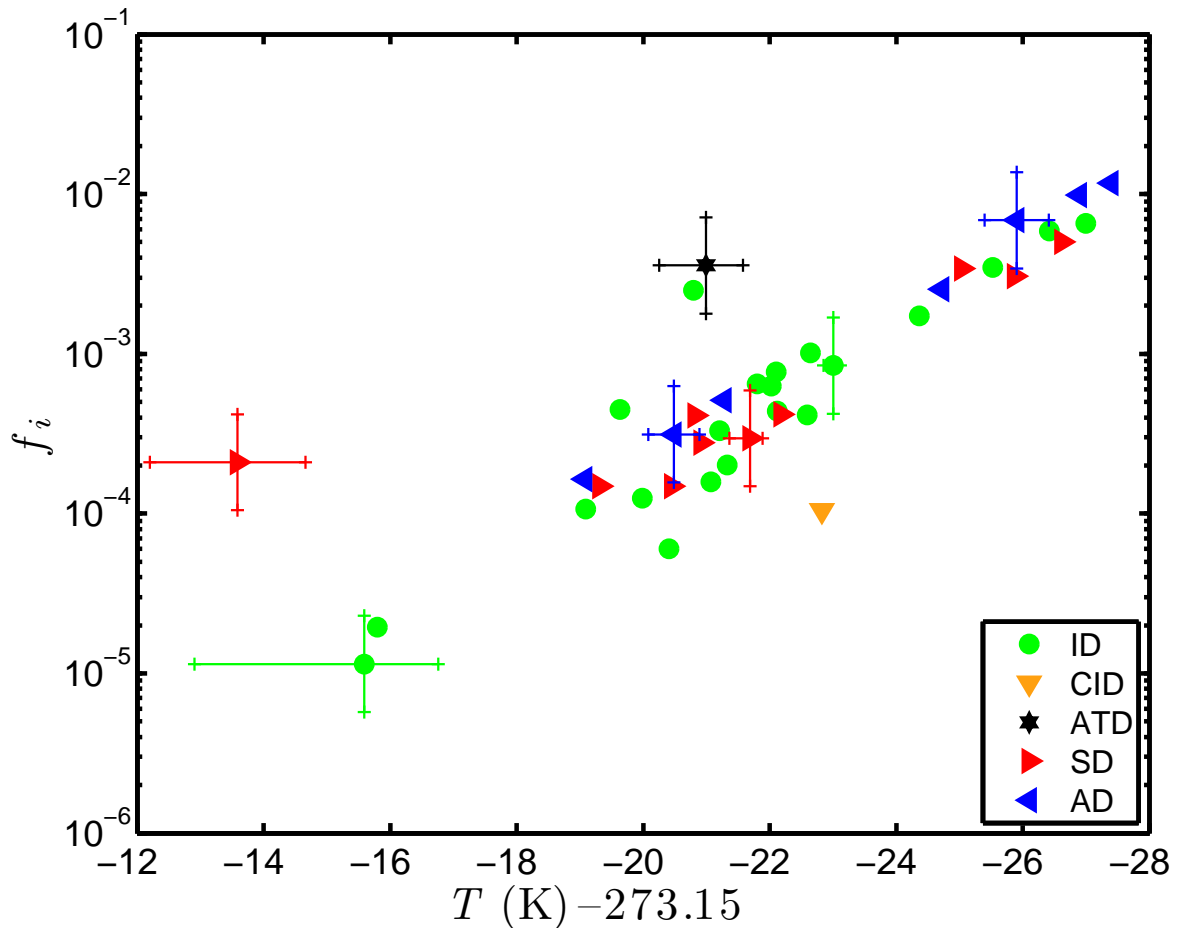
Figure 4.4.: Ice-active particle fraction f_i versus temperature for all experiments listed in Table 4.2. The horizontal error bars represent the temperature uncertainty in N_i due to the averaging over a time period of minimum 60 s. The vertical error bars represent a factor of two uncertainty in f_i. For clarity, only a few error bars are show (see text for more information).

crystals and the uncertainty of the aerosol number concentration.

In general, f_i increases exponentially with decreasing temperature. Ice nucleation is first observed at a temperature of about –13 °C in the case of SD, and at around –16 °C in the case of ID. No ice is detected in the AIDA expansion experiments with AD in the temperature range between –10 °C and –19 °C. Some AD particles can still be ice-active in this temperature range, but only in amounts below the ice crystal detection limit, which is about $0.01\,\mathrm{cm^{-3}}$ for the welas2 sensor, corresponding to $f_i = 10^{-5}$ at a particle number concentration of $1000\,\mathrm{cm^{-3}}$. Other than ID, AD and SD, the ATD and CID samples were not examined in the whole temperature range from –10 °C to –28 °C (cf. Table 4.1). The ATD and CID data points each are derived from a single

experiment. f_i is $4 \cdot 10^{-3}$ for ATD at about –21 °C and $1 \cdot 10^{-4}$ for CID at about –23 °C. The largest activated fraction of all immersion freezing experiments shown here is about 1 %. This is reached in the case of AD, ID and SD at a temperature of about –28 °C.

4.2.1. Surface size distributions

The desert dust samples were sized with a SMPS and APS prior to each experiment run with a freshly dispersed dust sample (chapter 3.2). To compare the results of the two instruments, the aerodynamic diameter measured by the APS and the equivalent mobility diameter measured by the SMPS were converted into a volume–equivalent sphere diameter. For this conversion, the bulk density and the shape factor must be known (Hinds, 1999). Typical densities used in dust aerosol studies range from 2.5 g cm^{-3} for sand (Davies, 1979; Linke et al., 2006) to 2.65 g cm^{-3} for quartz (Tegen and Fung, 1994; Hinds, 1999; Kandler et al., 2007). Hinds (1999) tabulates a dynamic shape factor of 1.36 for quartz and 1.57 for sand. A bulk density of 2.6 g cm^{-3} for all dust samples and dynamic shape factors between 1.1 and 1.4 gave the best match between SMPS and APS in the experiments presented in this chapter.

The surface size distributions were calculated from the number size distributions, assuming that the dust particles are spheres with the respective volume–equivalent sphere diameter. Figure 4.5 shows surface size distributions for all freezing experiments listed in Table 4.2. A log-normal distribution (1 or 2 modes) was fitted to the data with median diameters $d_{S,median}$ and geometric standard deviations σ as listed in Table 4.3. The counting efficiency at the lower and upper end of the detection limits of SMPS and APS is reduced. Therefore, in the log-normal fits the SMPS data is considered only up to 600 nm and the APS data from 800 nm. The sum of the area under the curve corresponds to the total dust particle surface area concentration S_{tot} available in the experiment. S_{tot} is used in section 4.2.2 to calculate the ice-active surface site density n_s, which is the number of ice-active surface sites per unit area.

4.2.2. Parameterization of immersion freezing

In order to parameterize the experimental results on immersion freezing, the so-called ice-active surface site density approach (chapter 2.3) was applied (e.g. Connolly et al., 2009, paper called C09 hereafter). It is assumed that localized sites with specific activation energies for ice nucleation are equally distributed over the dust particle

surface area. It is further assumed that different sites exist with a wide range of freezing probabilities as a function of temperature and time. From a large number of AIDA expansion experiments there is evidence that the formation of ice is mainly related to the total temperature change and the particle surface area (equation (5) in C09).

The ice crystal number concentration formed by active IN in size bin j, $N_{i,j}$, is expressed as (cf. chapter 2)

$$N_{i,j} = N_{tot,j}\{1 - \exp[-S_{ae,j}n_s(T)]\} \tag{4.1}$$

where $N_{tot,j}$ is the total number concentration of particles in size bin j and $S_{ae,j}$ is the individual particle surface area in that size bin. The density of ice-active surface sites $n_s(T)$ is considered constant throughout the size distribution, assuming that the aerosol composition and surface properties do not vary with size.

For a polydisperse aerosol sample, i.e. sample containing particles of different sizes, equation (4.1) is summed over all n size bins:

$$\sum_{j=1}^{n} N_{i,j} = \sum_{j=1}^{n} N_{tot,j}\{1 - \exp[-S_{ae,j}n_s(T)]\}. \tag{4.2}$$

For $S_{ae,j}n_s(T) \ll 1$, equation (4.2) can be approximated by

$$\sum_{j=1}^{n} N_{i,j} \approx \sum_{j=1}^{n} N_{tot,j}S_{ae,j}n_s(T) = n_s(T)\sum_{j=1}^{n} N_{tot,j}S_{ae,j} \tag{4.3}$$

Rearranging equation (4.3) yields

$$n_s(T) = \frac{\sum_{j=1}^{n} N_{i,j}}{\sum_{j=1}^{n} N_{tot,j}S_{ae,j}} = \frac{\sum_{j=1}^{n} N_{i,j}}{\sum_{j=1}^{n} S_{tot,j}} = \frac{N_i}{S_{tot}} \tag{4.4}$$

where $S_{tot,j}$ is the total surface area per unit volume of particles in a size bin, N_i is the total ice number concentration and S_{tot} is the total surface area concentration of particles in all n size bins.

N_i is measured in the AIDA expansion experiment. S_{tot} (section 4.2.1) is measured prior to each cloud expansion experiment and multiplied by the pressure dilution p/p_0 to to reduce it through the experiment. Figure 4.6 shows S_{tot}, N_i, the droplet number concentration N_d, and the calculated value of n_s versus decreasing temperature as

an example for experiment ACI04_19 with AD. N_i is small compared to N_d (e.g. $N_i \approx 1\,\mathrm{cm}^{-3}$ and $N_d \approx 70\,\mathrm{cm}^{-3}$ at –28 °C, corresponding to a frozen fraction f_i of about 1 %). S_{tot} decreases from initially $1.5 \cdot 10^2\,\mathrm{\mu m^2\,cm^{-3}}$ at –23.5 °C (start of ice formation) to $1.2 \cdot 10^2\,\mathrm{\mu m^2\,cm^{-3}}$ at –28 °C. n_s is calculated using equation (4.4). In the course of experiment ACI04_19, n_s increases to a value of about $2 \cdot 10^{10}\,\mathrm{m^{-2}}$ at –28 °C.

This calculation was repeated for all freezing experiments. Figure 4.7 shows the resulting n_s values versus decreasing temperature for all experiments with ID. The values that correspond to a single experiment are connected with a line. The fluctuations in n_s are due to the averaging of N_i over a time period of minimum 60 s as described above. In general, a exponential increase in n_s is observed.

Figure 4.8 shows n_s versus decreasing temperature for all experiments listed in Table 4.2. The plot also includes the corrected surface site densities obtained by C09. A reanalysis of some of the older AIDA expansion experiments showed that C09 overestimated the surface site density by about a factor of ten, mainly due to a systematic error, resulting in underestimating the aerosol surface area by this factor.

The data points suggest that an exponential function fits the data best. The fit does not include the C09 data. Also the ATD data point was left out, since ATD is a processed and milled sample (see Möhler et al., 2006). Crushed particles from this manufacturing process probably involve a higher density of surface defects and therefore a higher ice activity.

The exponential fit is given by the equation:

$$n_s(T) = \exp[-0.517(T - 273.15) + 8.934] \quad (m^{-2}) \tag{4.5}$$

with T in °C. This equation can be used in models as a parameterization of immersion freezing on desert dust particles in the temperature range –12 °C and –36 °C. It will be used and compared to other concepts in sections 4.3.2, 4.3.4 and 4.3.5.

The ice-active fraction in a size bin $f_{i,j}$ can be calculated via (see equation (4.1)):

$$f_{i,j} = \frac{N_{i,j}}{N_{tot,j}} = 1 - \exp[-S_{ae,j}n_s(T)] \approx S_{ae,j}n_s(T) \tag{4.6}$$

The approximation is valid for small aerosol particles and experiments at higher temperatures as demonstrated in Figure 4.9. However, e.g. for particles larger than about 3 µm and temperatures lower than –30 °C, f_i approaches 1 and has to be calculated with the exact formulation for each size bin.
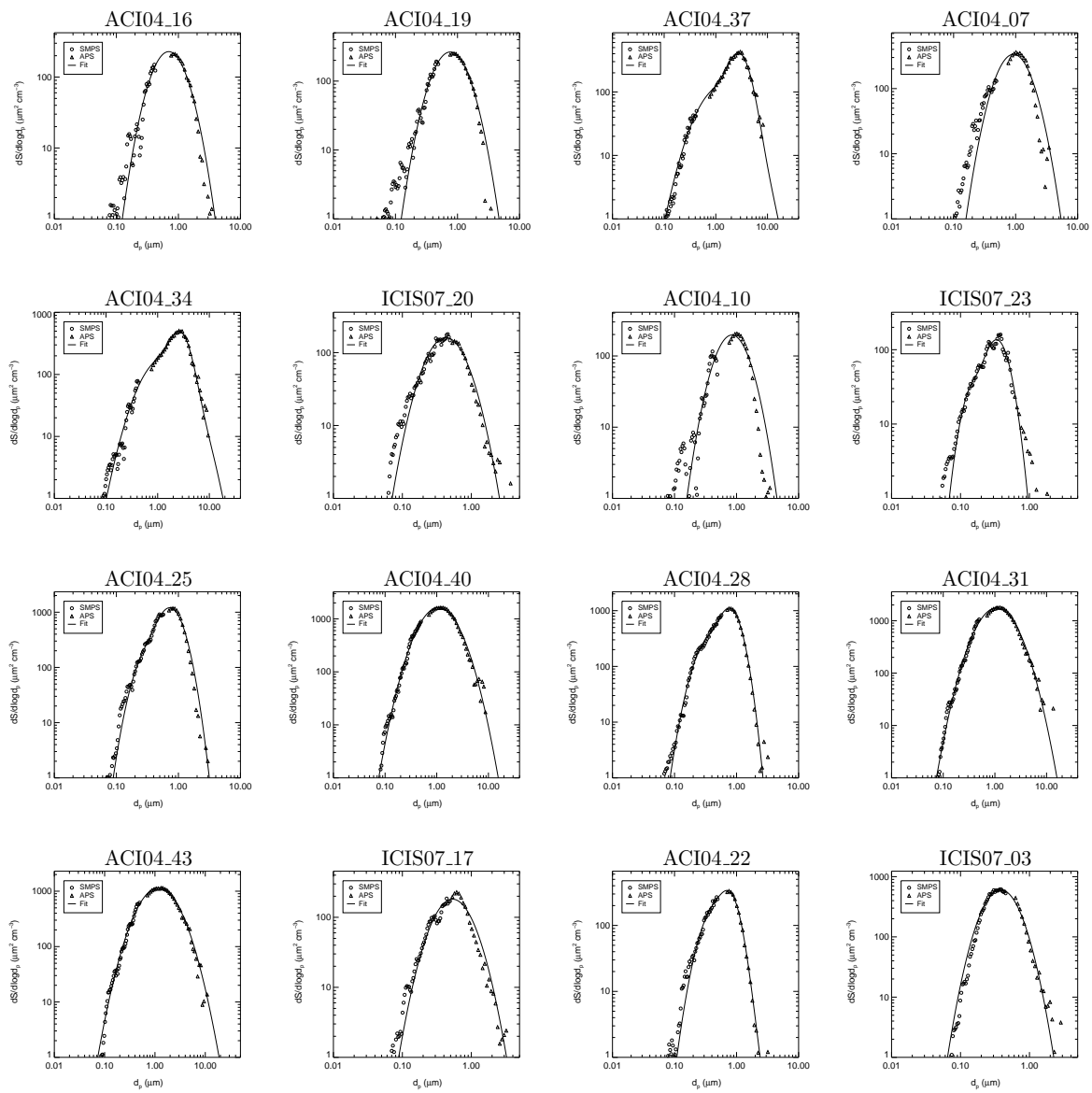
Figure 4.5.: Surface size distributions and log-normal fits for all experiments marked with "freezing" in Table 4.2 (same order). The log-normal fit parameters are listed in Table 4.3.

Table 4.3.: List of log-normal fit parameters to the surface size distributions (one or two modes).

| Exp. No.	Dust	$S_{tot,1}$ (µm² cm⁻³)	$d_{S,median,1}$ (µm)	σ_1	$S_{tot,2}$ (µm² cm⁻³)	$d_{S,median,2}$ (µm)	σ_2
ACI04_13	AD	7.55	0.23	1.39	101.63	0.79	1.56
ACI04_16	AD	130.01	0.70	1.69	-	-	-
ACI04_19	AD	156.38	0.76	1.72	-	-	-
ACI04_04	SD	38.97	0.52	1.50	106.89	1.13	1.42
ACI04_37	SD	106.26	1.29	2.26	142.29	2.82	1.48
ACI04_07	SD	189.17	0.92	1.68	-	-	-
ACI04_34	SD	162.96	1.37	2.23	146.21	2.69	1.44
ICIS07_20	SD	98.53	0.43	1.75	-	-	-
ACI04_10	SD	110.16	0.84	1.67	-	-	-
ICIS07_23	CID	10.51	0.16	1.37	48.59	0.34	1.39
ACI04_25	ID	486.36	0.74	1.47	90.33	0.35	1.53
ACI04_40	ID	1229.70	1.08	2.00	-	-	-
ACI04_28	ID	352.73	0.79	1.39	161.86	0.40	1.58
ACI04_31	ID	1333.85	1.08	2.00	-	-	-
ACI04_43	ID	922.50	1.17	2.10	-	-	-
ICIS07_17	ID	110.28	0.54	1.75	-	-	-
ACI04_22	ID	59.98	0.78	1.34	105.49	0.51	1.60
ICIS07_03	ATD	328.04	0.38	1.64	-	-	-
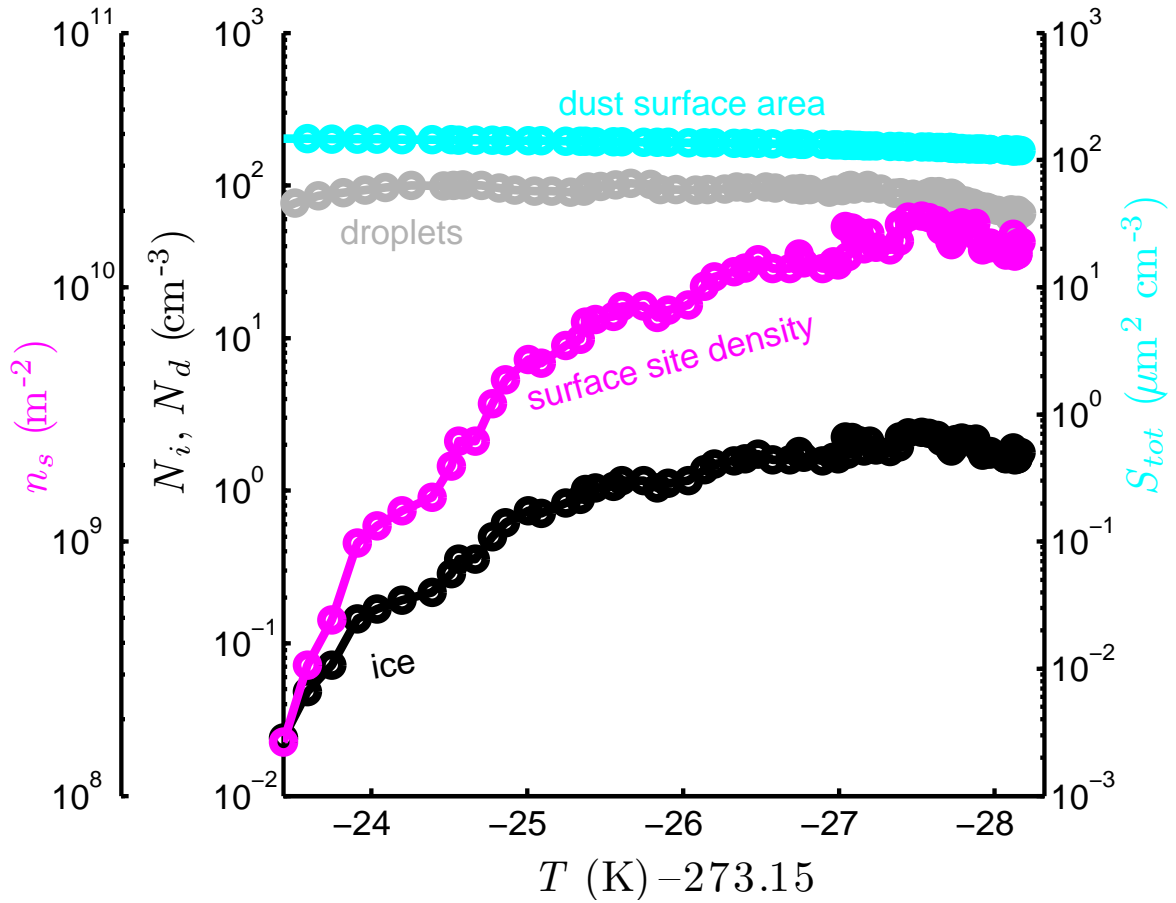
Figure 4.6.: Measured droplet and ice number concentration, N_i and N_d, particle surface area concentration, S_{tot}, and calculated ice-active surface site density, n_s, for experiment ACI04_19 with Asian dust (AD) versus decreasing temperature.
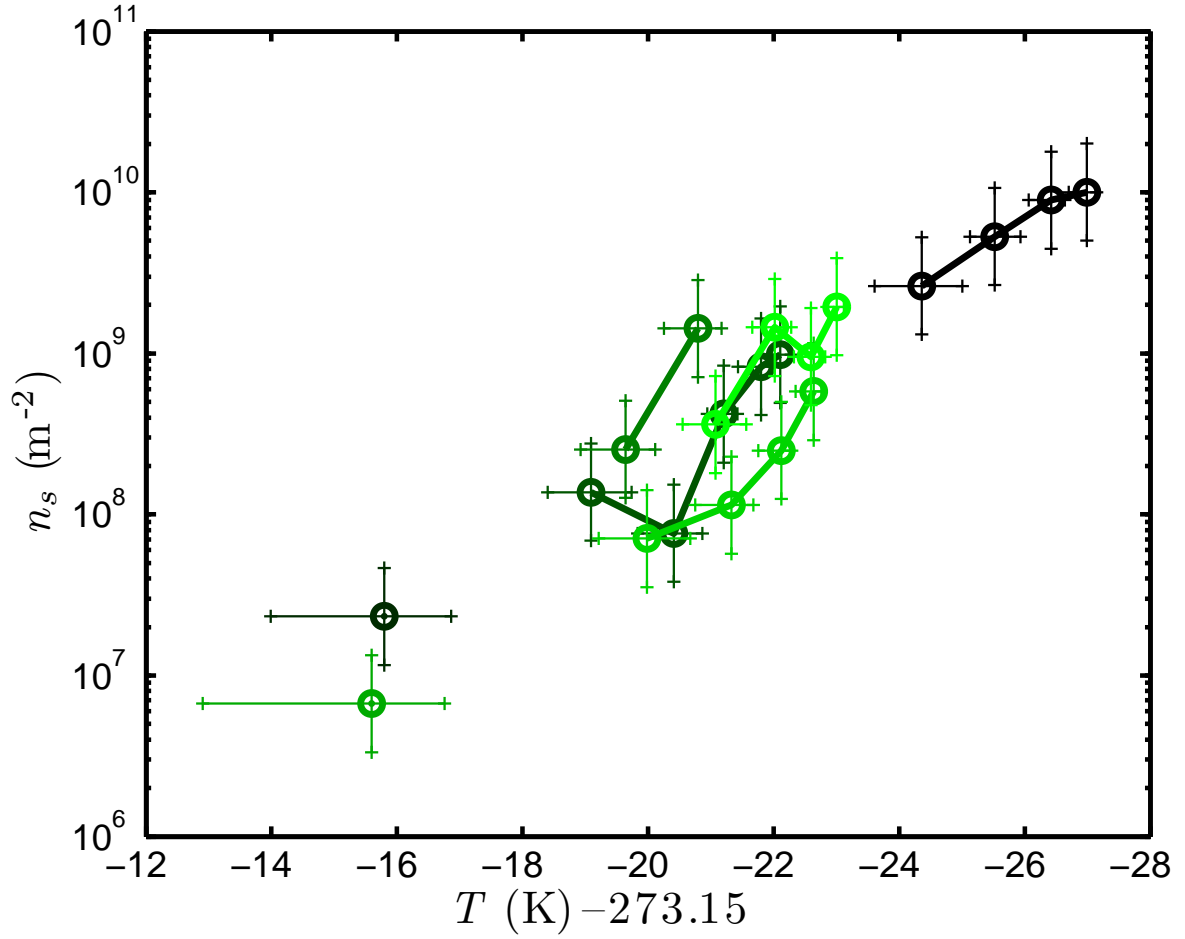
Figure 4.7.: The calculated values of n_s versus decreasing temperature for all immersion freezing experiments with ID listed in Table 4.2. The data point that belong to one experiment are connected. For the calculation of n_s, N_i was averaged over a time period of minimum 60 s as described in section 4.2.
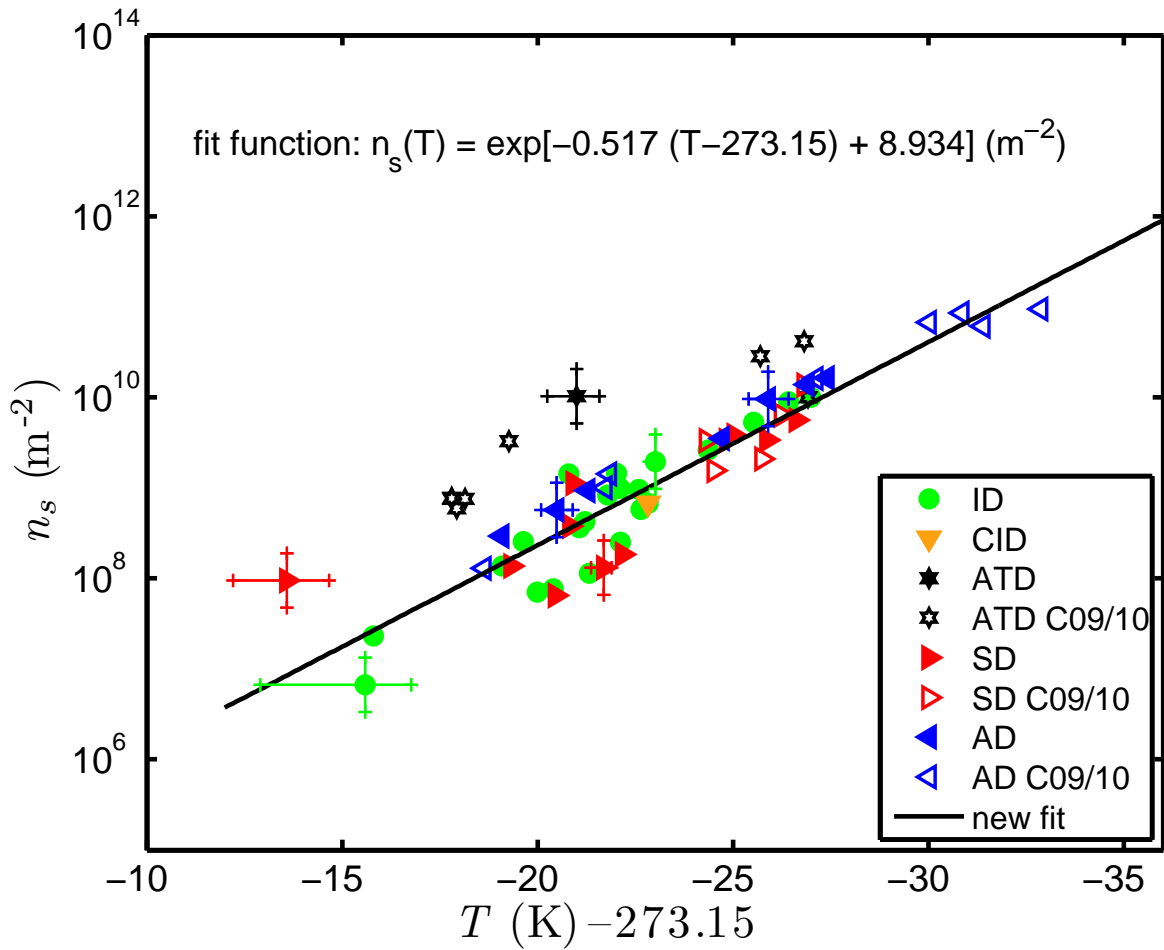
Figure 4.8.: The black solid line is a T-dependent fit to all natural dusts investigated in this chapter ($R^2 = 0.91$). The plot also includes the data from Connolly et al. (2009) (C09) reduced by a factor of 10 (see section 4.2.2).
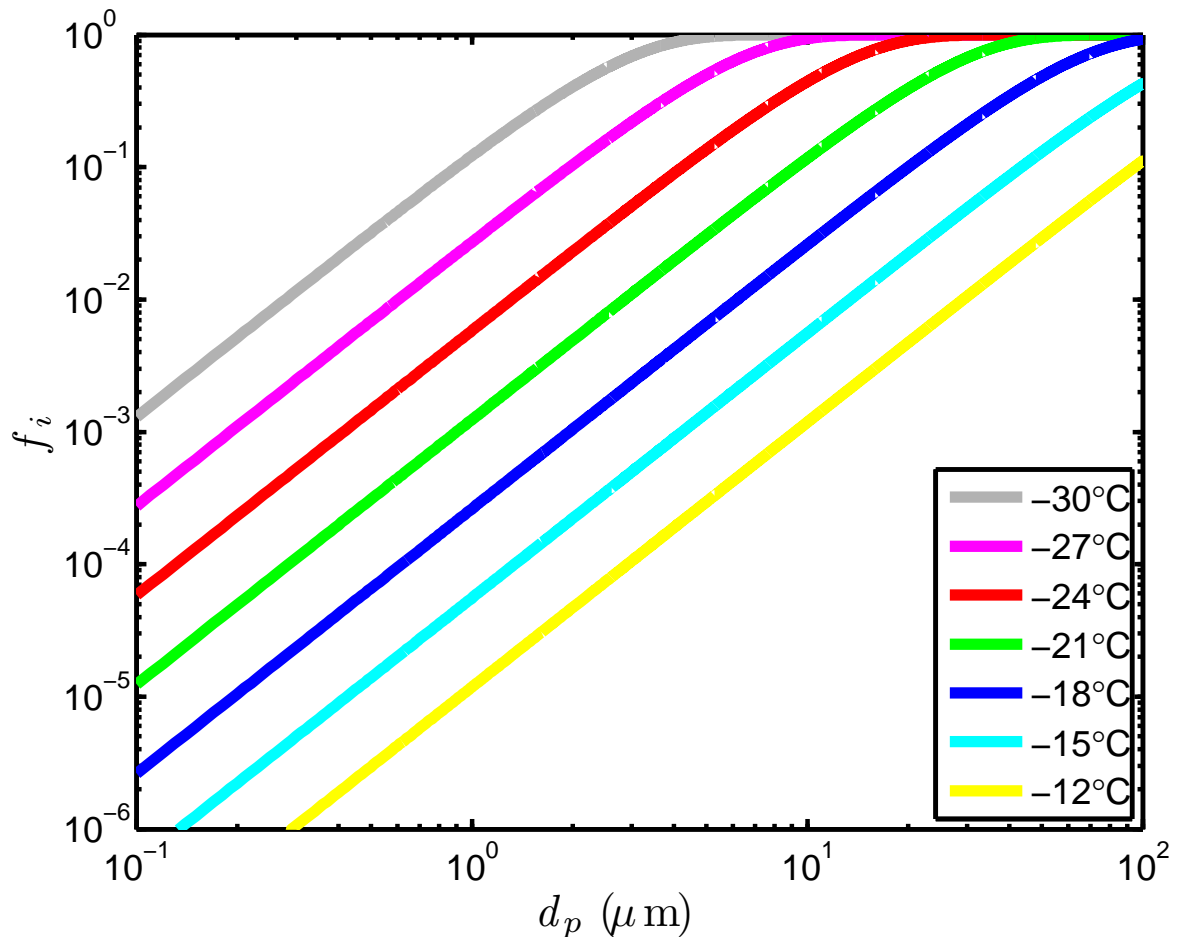
Figure 4.9.: The fraction of ice versus the diameter of monodisperse aerosol calculated using equation (4.6) for different temperatures.

4.3. Saharan dust event of May 2008

In the following, the new immersion freezing parameterization derived in section 4.2.2 will be applied to a Saharan dust outbreak to calculate distribution maps of IN, which will then be compared to measurements at the Taunus Observatory on Mount Kleiner Feldberg and to other parameterizations.

4.3.1. Description and simulation with COSMO-ART

In May 2008, a major dust outbreak over the Sahara occurred. This event transported large amounts of Saharan dust across the Mediterranean area and Western Europe. The regional scale online coupled model system COSMO-ART[1] (Vogel et al., 2009; Bangert et al., 2011a) was used to simulate the development and the spatial distribution of the dust plume. The performance of the model system has been recently evaluated by Knote et al. (2011) under a broad range of conditions, and by Stanelle et al. (2010) and Bangert et al. (2011b) for case studies of Saharan dust outbreaks. COSMO-ART includes a detailed dust emission scheme (Stanelle et al., 2010; Vogel et al., 2006) that gives size-dependent emission fluxes of particles depending on the friction velocity and a data set of surface properties (Marticorena et al., 1997; Callot et al., 2000). COSMO-ART uses a modal approach to simulate the particle size distributions of number, surface area, and mass. Three log-normal modes that differ in their number median diameter (mode 1: $0.64\,\mu m$; mode 2: $3.45\,\mu m$; mode 3: $8.67\,\mu m$) and geometric standard deviation (mode 1: 1.7; mode 2: 1.6; mode 3: 1.5) are applied.

In this application of the model system, dust was simulated only. All other aerosol types were neglected. The horizontal spatial resolution was $0.25\,°$ in both directions, which corresponds to about $28\,km$. The model domain is shown in Figure 4.14. 40 vertical layers up to a height of $28\,km$ altitude were used. The simulation started at 00 UTC on 22 May 2008 and ended at 17 UTC on 31 May 2008. The model run was driven by IFS (ECMWF Integrated Forecast System) boundary conditions. Those boundary conditions are updated every six hours. At the beginning of the simulation, it was assumed that the atmosphere is dust-free. During the simulation period the dust emissions lead to the development of a significant dust plume. A comparison with observations demonstrated that the model system simulates the meteorological situation and the dust plume reasonably well (Bangert et al., 2011b).

---

[1] **CO**nsortium for **S**mall-scale **MO**deling—**A**erosols and **R**eactive **T**race gases; www.cosmo-model.org

Figure 4.10 shows a longitudinal vertical cross section of the simulated number concentration of dust particles at $50°\,13'\,N$ (along the Taunus Mountains, Germany) on 28 May 2008, 12 UTC. The dust plume is about 800 km wide and extends from the surface to 8–11 km in height. The number concentration reaches its maximum of $1.11 \cdot 10^5\,L^{-1}$ at around 3 km. The corresponding vertical cross section of the total surface area concentration of dust particles (Figure 4.11) gives a maximum value of $4.18 \cdot 10^5\,\mu m^2\,L^{-1}$ at around 3 km height. The total dust particle surface area concentration and the temperature from the COSMO-ART model simulation served as an input for the calculation of the IN number concentration using the new parameterization.

Figure 4.12 compares the simulated mass concentrations of particles less than 10 μm in diameter (PM10) from COSMO-ART (PM10 COSMO) and DREAM (PM10 DREAM; Nickovic et al., 2001; Klein et al., 2010) to the measured PM10 mass concentration derived from APS size distributions (PM10 KF) during the Saharan dust event at the Taunus Observatory on Mount Kleiner Feldberg (cf. Fig. 7 in Klein et al., 2010). PM10 KF is affected by the background concentration of small e.g. sulfate, nitrate, soot and organic particles which lead to higher particle number concentrations compared to PM10 COSMO and PM10 DREAM which include dust only. The background mass concentration at the Taunus Observatory is in the order of 15–25 μg m^{-3} (cf. Klein et al., 2010). PM10 COSMO and PM10 DREAM show an increase during the time of the dust event, however they predict a factor of two to four higher PM10 mass concentrations than the measurements.

The surface area concentration calculated from the COSMO-ART modeled dust particle size distribution (S COSMO) is compared to the surface area concentration derived from APS size spectra (S KF) during the time of the Saharan dust event in Figure 4.13. The peak values of S COSMO and S KF are $270\,\mu m^2\,cm^{-3}$ and $400\,\mu m^2\,cm^{-3}$, respectively. The numbers are in good agreement, however they are reached at different times. The peak in S COSMO is reached on 29 May 2008, in S KF on 30 May 2008.

4.3.2. Application of new parameterization

Based on the model results from COSMO-ART (total dust particle surface area concentration and temperature) the new parameterization was applied (see equation (4.4) and equation (4.5)) to calculate the spatial distribution of immersion freezing nuclei at 6000 m above surface (Figure 4.14), independent of the simulated relative humidity.

At 6000 m height, temperatures around –18 °C were reached. The pattern shows high IN number concentrations of more than $500\,L^{-1}$ above Northern Africa and North–East of Spain and spreads across Western Europe. The black line in Figure 4.14 indicates the location of the vertical cross section at 50° 13' N presented in Figure 4.10 and Figure 4.15.

Figure 4.15 shows the vertical distribution of potential immersion freezing nuclei at this latitude. For this calculation a constant temperature of –18 °C was used for the comparison with FRIDGE[2] measurements of IN which were performed at this temperature (section 4.3.3). The maximum ice number concentration of $27\,L^{-1}$ is reached in 3 km height.

4.3.3. Measurements of IN at the Kleiner Feldberg field site

The number concentration of deposition/condensation freezing IN is measured at Taunus Observatory on Mount Kleiner Feldberg since April 2008 on a regular daily basis. For these measurements, the atmospheric aerosol is collected for time periods of 5 minutes by electrostatic precipitation on silicon wafers in the 10 nm to 20 µm size range. The samples are then analyzed in FRIDGE at –18 °C and $RH_i = 119\,\%$ ($RH_w \approx 100\,\%$) for their IN number. The grown ice crystals are viewed by a CCD camera and counted automatically. High aerosol number concentrations and a strong increase in the IN number concentrations at –18 °C were measured at the Taunus Observatory during the Saharan dust event in May 2008 (Klein et al., 2010). In addition, an aerodynamic particle sizer (APS, TSI Inc., USA) was used to measure aerosol particle number distributions in the size range 0.5 µm to 20 µm during the time of the dust event. The aerosol surface area concentration calculated from the APS size distributions were used to calculate the IN number concentration with the new parameterization. The results are compared to the IN number calculated from the simulation and to FRIDGE measurements in section 4.3.4.

4.3.4. Comparison of modeled and measured results

The total dust particle surface area concentration, calculated from the simulated number size distribution, served as an input to the new parameterization. The resulting IN number concentrations are compared to those measured with FRIDGE (section 4.3.3) for a temperature of –18 °C (Figure 4.16). For this comparison, the simulated

---

[2]Frankfurt Ice Deposition Freezing Experiment (Bundke et al., 2008)

number size distribution at the closest point to Mount Kleiner Feldberg (model layer at 800 m a.s.l.) was used. A background concentration of $26.27\,\mathrm{L^{-1}}$ (average IN number concentration in FRIDGE before and after the dust event) was subtracted from the FRIDGE measurements during the dust event.

Because RH_w is approximately 100 % in FRIDGE, it can be assumed that water uptake is involved in the freezing process. Most of the ice formation in the AIDA expansion experiments of this work occurred through the immersion freezing mode, with some minor contribution of condensation freezing close to the onset of cloud condensation. In a comparison study by DeMott et al. (2011), FRIDGE and AIDA showed similar freezing onsets in the case of ATD, but a systematic difference between both methods cannot yet be completely ruled out, in particular if condensation and immersion freezing rates and active fractions markedly differ from each other at $-18\,^{\circ}\mathrm{C}$.

Figure 4.16 shows the comparison between calculated IN number concentrations and FRIDGE measurements. The grey shaded area in Figure 4.16 indicates the uncertainty in the calculated IN number concentration due to the uncertainty in the surface area concentration from the model simulation. The uncertainty of about a factor of ten is estimated from the comparison of the COSMO-ART to the DREAM modeled surface area concentration (not shown here; cf. Fig. 8. (b) in Klein et al., 2010).

The new parameterization was additionally applied to the APS measured size distributions of particles obtained at the same time. Therefore the APS data was averaged over the sampling time of the filter probe for the analysis in FRIDGE. For comparison reasons, the black dashed line in Figure 4.16 represents the IN number concentration excluding the contribution from particles smaller $0.5\,\mathrm{\mu m}$ to the total particle surface area concentration from the model simulation. The calculated IN number concentrations based on the simulation and on the measurement are in good agreement. Also the simulation captures the peak IN number concentration during the dust event between 26 May 2008 and 30 May 2008. However, whereas the FRIDGE measurement shows IN peak concentrations of about $286\,\mathrm{L^{-1}}$, the new parameterization leads to about $22\,\mathrm{L^{-1}}$.

The total surface area concentration from the model simulation is continued to be used as an input for further comparisons between different parameterizations (see section 4.3.5).

4.3.5. Comparison to other concepts

Figures 4.17 shows the new parameterization in comparison to three other concepts, including the parameterizations by DeMott et al. (2010), Hoose et al. (2010) and Phillips et al. (2008) for the temperatures –15 °C, –18 °C and –25 °C. The total particle surface area concentration or number concentration calculated from the COSMO-ART model simulation are used as input parameters for the different parameterizations.

Whereas the new parameterization is based on lab studies in the AIDA cloud simulation chamber (IN number concentration as a function of dust particle surface area concentration and temperature), the parameterizations by DeMott et al. (2010) and Phillips et al. (2008) are based on field measurements of IN number concentrations with a continuous flow diffusion chamber. In the parameterization by DeMott et al. (2010), the IN number concentration is a function of number concentration ($d_p > 0.5\,\mu m$) and temperature. The parameterization by Phillips et al. (2008) uses the particle surface area and the ice supersaturation as input parameters. Phillips et al. (2008) extrapolated their fit to temperatures warmer than –25 °C. The time-dependent parameterization by Hoose et al. (2010) is based on classical nucleation theory and laboratory experiments with montmorillonite/illite. The parameterizations by Hoose et al. (2010) and Phillips et al. (2008) are both evaluated at water saturation. All parameterizations, except the one by DeMott et al. (2010), are proportional to the surface area and differ only by a constant factor at a constant temperature.

The new parameterization is most sensitive to the temperature variation. The peak IN number concentrations for –15 °C, –18 °C and –25 °C are about $5\,L^{-1}$, $22\,L^{-1}$ and $742\,L^{-1}$, respectively. The IN number concentrations calculated with the parameterization by DeMott et al. (2010) are roughly $3\,L^{-1}$ (–15 °C), $7\,L^{-1}$ (–18 °C) and $36\,L^{-1}$ (–25 °C). The parameterization by Phillips et al. (2008) gives IN number concentrations of about $227\,L^{-1}$ (–15 °C), $357\,L^{-1}$ (–18 °C) and $1068\,L^{-1}$ (–25 °C). The parameterization by Hoose et al. (2010) gives values of about $310\,L^{-1}$ for –15 °C, $1119\,L^{-1}$ for –18 °C and $2665\,L^{-1}$ for –25 °C.

The parameterization by Hoose et al. (2010) leads to higher values of IN, due to the time dependency of the parameterization and the integration over 90 s, which corresponds to the measurement time of FRIDGE. Furthermore, this parameterization is based on experiments with montmorillonite/illite, pure clay minerals which are known to be very efficient IN. The extrapolation of Phillips et al. (2008) to temperatures warmer than –25 °C is uncertain due to the lack of constraining data. They used the form of the parameterization by Meyers et al. (1992) as a basis for their

extrapolation. The parameterization shows a relatively weak dependence on temperature between –15 °C and –25 °C. The lower IN number concentrations predicted by the DeMott et al. (2010) parameterization are likely due to its derivation from CFDC measurements sampling background concentrations in primarily non-dust dominated environments.
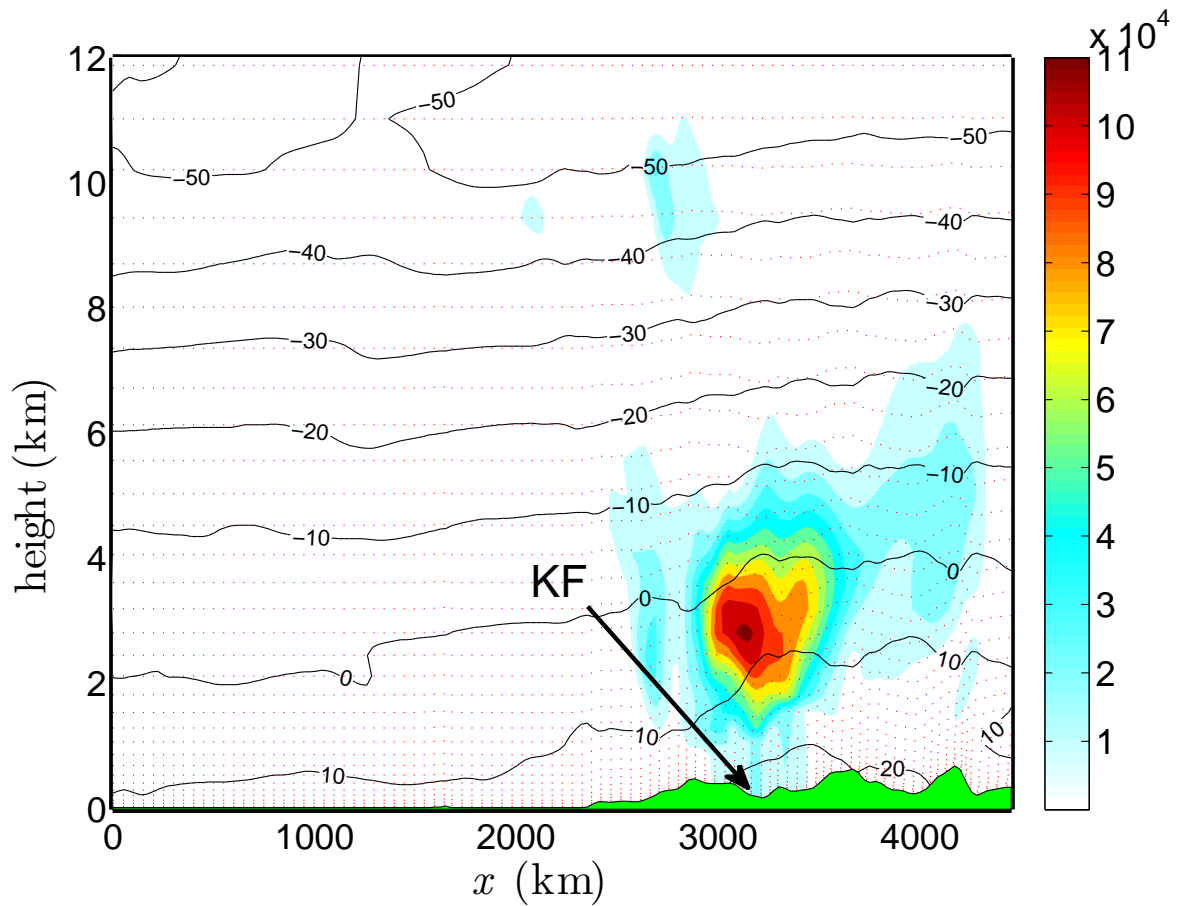
Figure 4.10.: Vertical cross section of the simulated number concentration (color code; L^{-1}) at 50° 13' N on 28 May 2008, 12 UTC. The x-axis shows the distance in km with respect to the simulated model domain (cf. Figure 4.14). 0 km corresponds to 20° W longitude. The topography is indicated in green. The red dotted lines illustrate the vertical levels in the model. The horizontal grid-size is 28 km. The lines of equal temperature (isothermal lines) are plotted in black.
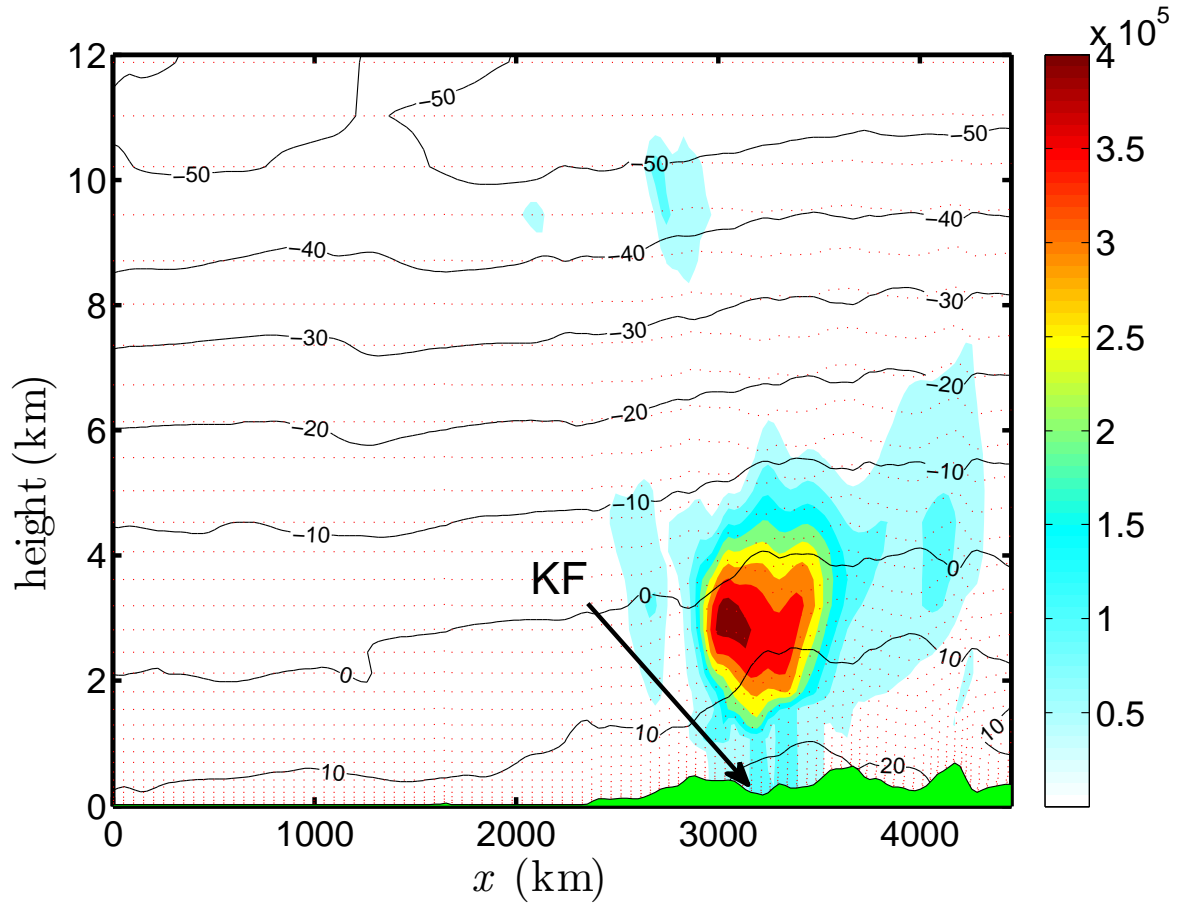
Figure 4.11.: Vertical cross section of the simulated dust particle surface area concentration (color code; $\mu m^2 \ L^{-1}$) at 50° 13' N on 28 May 2008, 12 UTC. The x-axis shows the distance in km with respect to the simulated model domain (cf. Figure 4.14). 0 km corresponds to 20° W longitude. The topography is indicated in green. The red dotted lines illustrate the vertical levels in the model. The horizontal grid-size is 28 km. The lines of equal temperature (isothermal lines) are plotted in black.
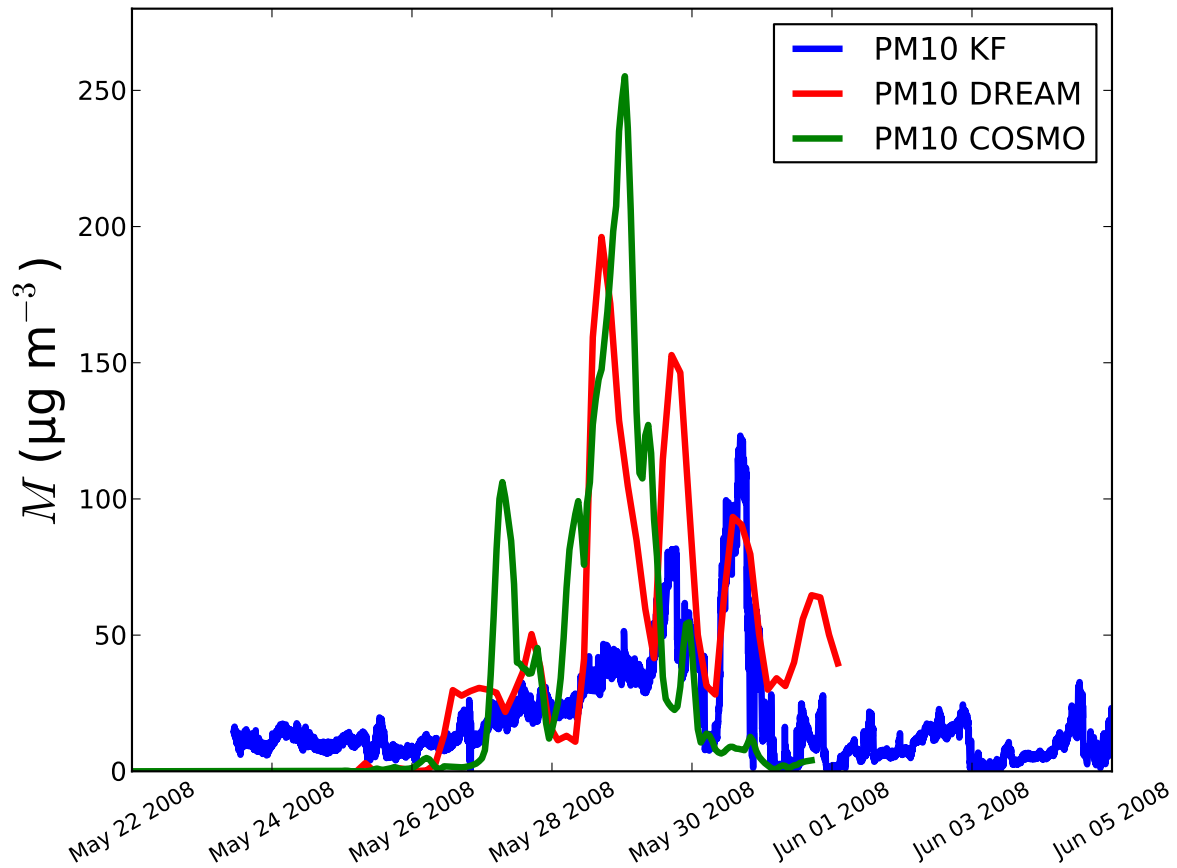
Figure 4.12.: Measured and modeled mass concentrations of particles less than 10 µm in diameter (PM10) during the Saharan dust event at the Taunus Observatory on Mount Kleiner Feldberg. **Blue line**: PM10 derived from APS size spectra (PM10 KF); **red line**: PM10 calculated by the DREAM model (PM10 DREAM; see Klein et al. (2010) for further details); **green line**: PM10 calculated by the COSMO-ART model (PM10 COSMO).
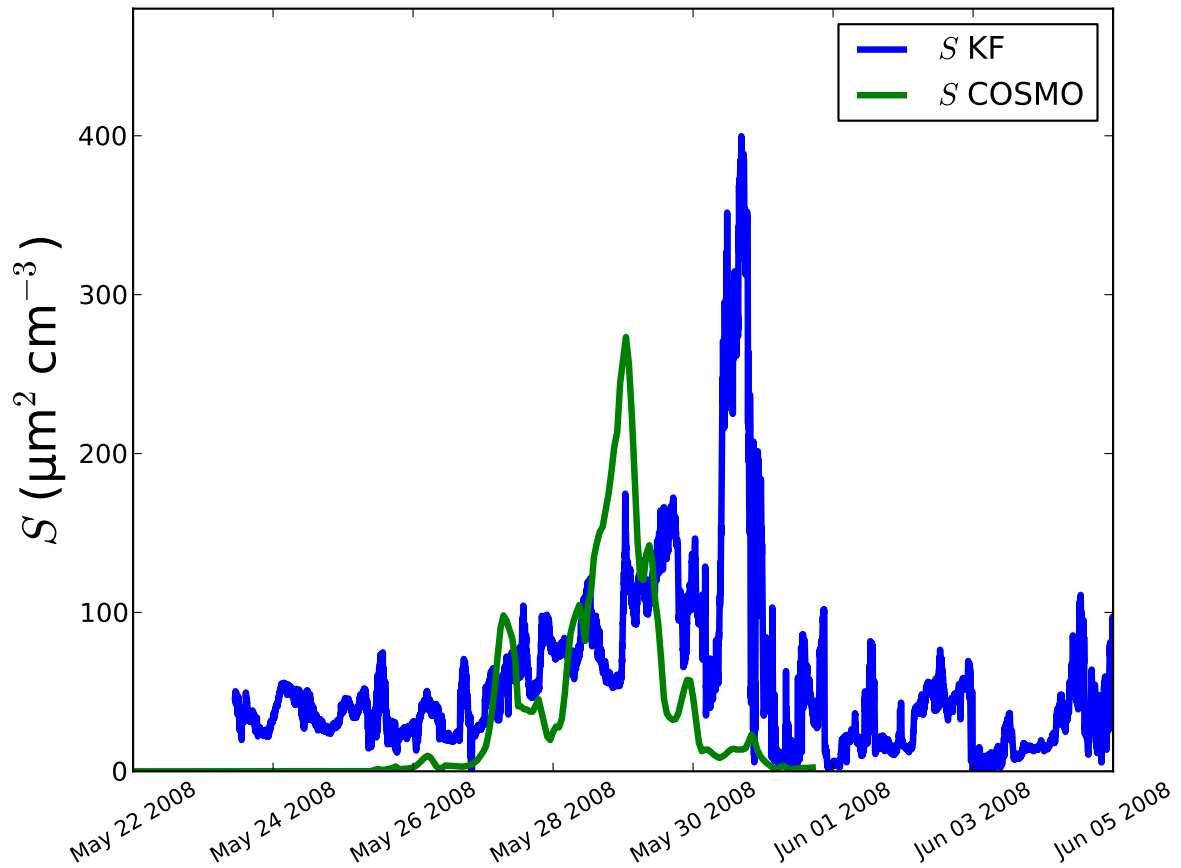
Figure 4.13.: Measured and modeled surface area concentration during the Saharan dust event at the Taunus Observatory on Mount Kleiner Feldberg. **Blue line**: total particle surface area concentration calculated from APS size distributions (S KF); **green line**: total dust particle surface area concentration calculated from the COSMO-ART modeled dust particle size distribution (S COSMO).
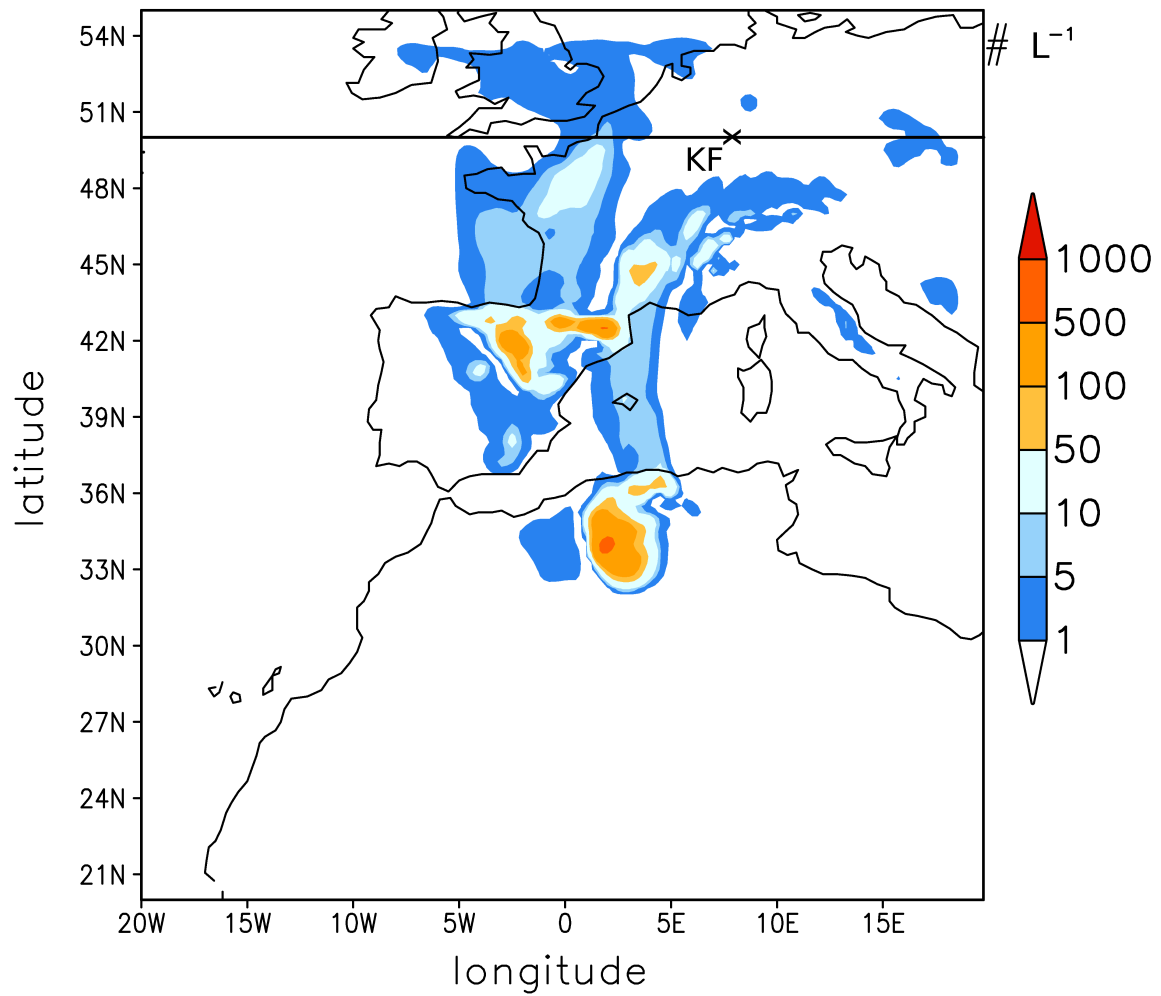
Figure 4.14.: Calculated potential immersion freezing nuclei at 6000 m height on 28 May 2008, 12 UTC. Simulated temperatures are around –8 °C at this height.
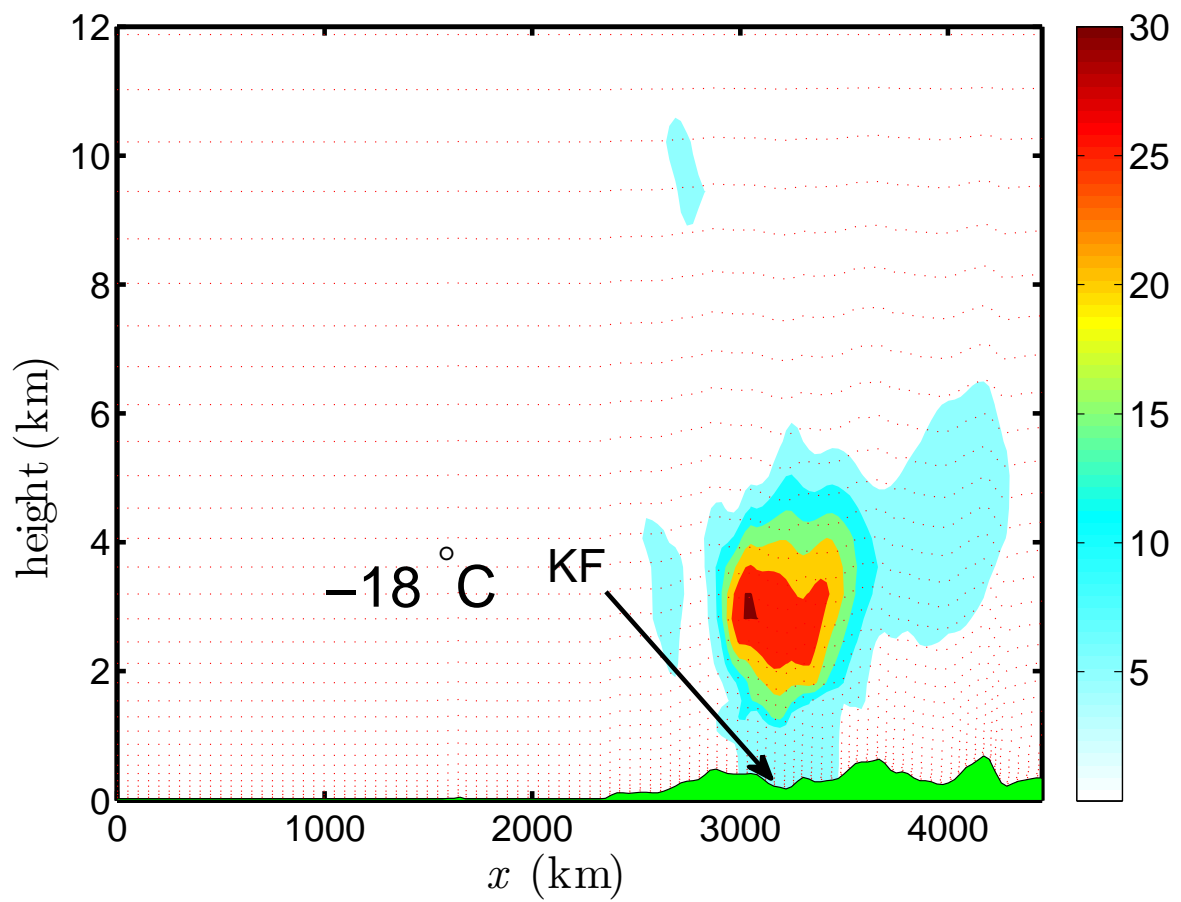
Figure 4.15.: Vertical crosssection of the potential immersion freezing nuclei (L^{-1}) at $50° 13'$ N as calculated with the new parameterization based on the COSMO-ART modeled surface area and a constant temperature of $-8°C$.
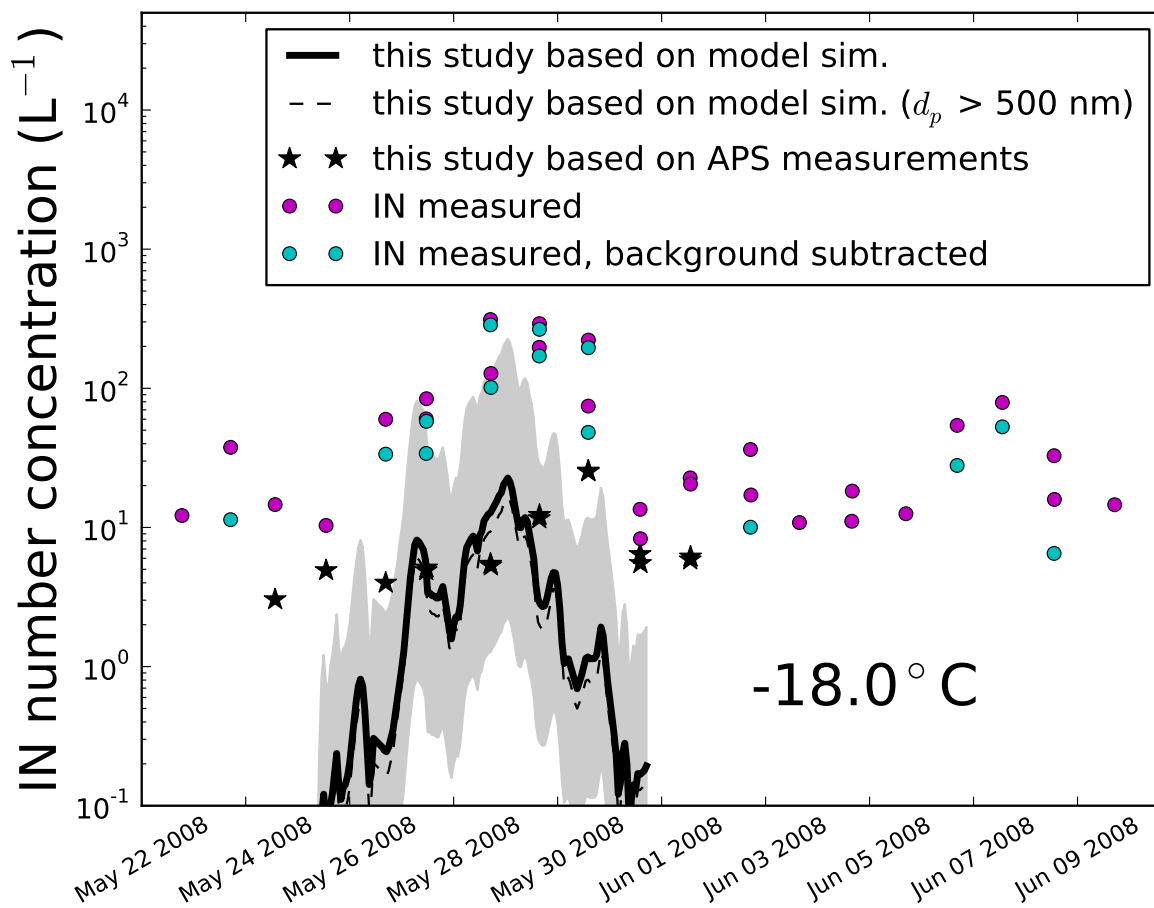
Figure 4.16.: IN number concentration versus time. Comparison of calculated IN number concentrations to FRIDGE measurements of IN at –18 °C. The grey shading indicates the uncertainty in the calculated IN number concentration due to the uncertainty in the simulated particle surface area concentration (section4.3.4).
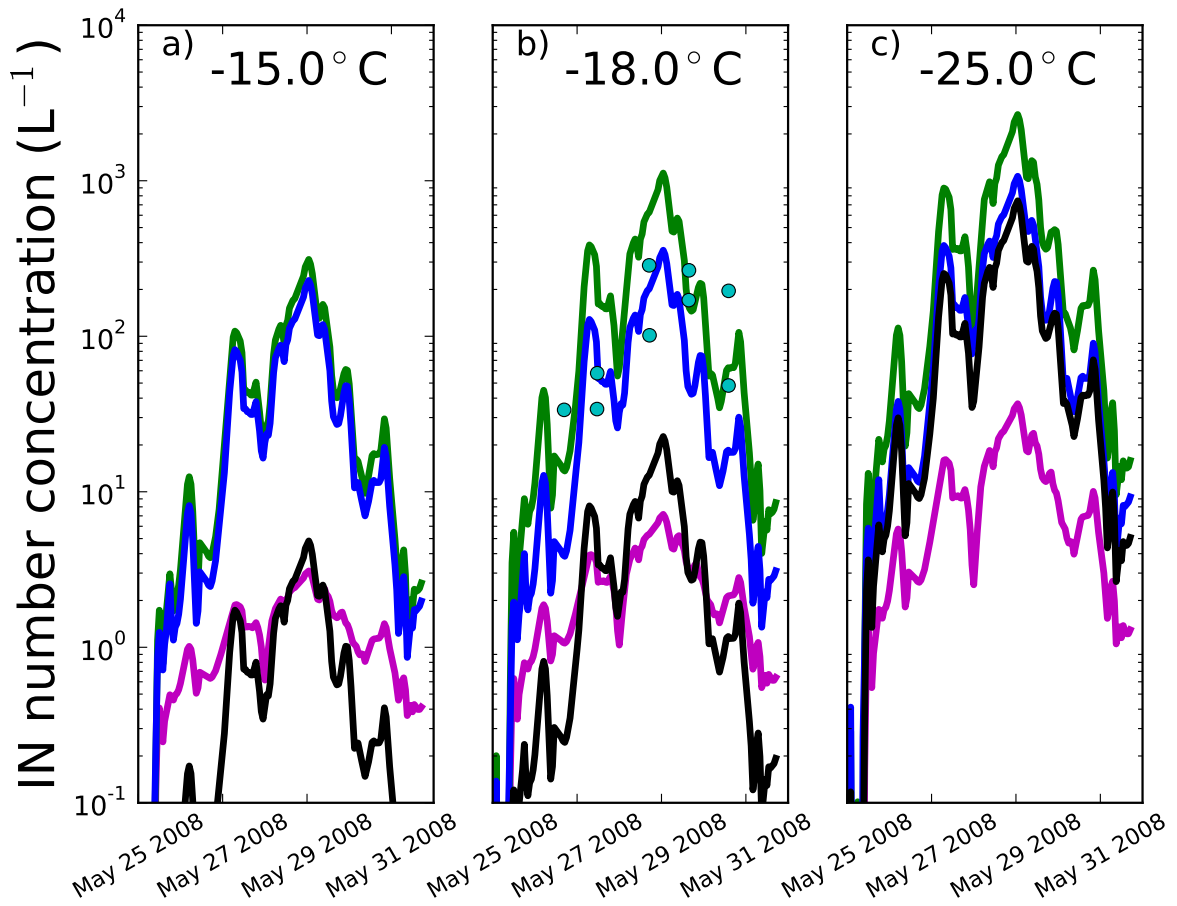
Figure 4.17.: IN number concentrations for different temperatures versus time. Comparison of different parameterizations for the temperatures a) –15 °C b) –18 °C and c) –25 °C. **Purple line**: DeMott et al. (2010); **green line**: Hoose et al. (2010); **blue line**: Phillips et al. (2008); **black line**: new parameterization; **turquoise dots plot b**: IN measured, background subtracted.

4.4. Comparison to literature data

In the following, the new parameterization, derived in section 4.2.2, is compared to available laboratory measurements from recent publications, conducted on the mineral dust surrogate ATD and the pure clay minerals, kaolinite and illite. Figure 4.18 depicts the ice-active surface site density n_s versus temperature. The new parameterization derived in this thesis is shown in black. The plot includes the data from Niedermeier et al. (2010) (ATD), Murray et al. (2011) (kaolinite), Broadley et al. (2012) (illite) and Lüönd et al. (2010) (kaolinite). All authors directly provide values of n_s, except for Lüönd et al. (2010) who provide measured ice-active fractions. In this case, n_s is calculated using equation (4.6) from section 4.2.2 (exact formulation).

Overall, the discrepancies between the new parameterization and literature data are large (up to a factor of one hundred). Niedermeier et al. (2010), who investigated the ice nucleation efficiency of size-selected ($\sim$300 nm) ATD particles, give values of n_s which are slightly lower than predicted by the new parameterization. This is in contrast to the result obtained from this work, were the milled and processed ATD sample appears to be more ice-active, resulting in a higher value of n_s compared the natural dust samples (cf. Figure 4.8). The discrepancy might be due to the use of size-selected ATD compared to the polydisperse sample used in this thesis. There could be a size dependence that scales with surface area, which has not been investigated yet. Furthermore, the different treatment of the dust samples, such as the dispersion method, or simply differences among the used samples might lead to this discrepancy.

Murray et al. (2011) and Broadley et al. (2012) used kaolinite and illite particles in their studies, respectively. Those two clay minerals are often found in natural dust samples, with kaolinite being less abundant than illite (Broadley et al., 2012). Both authors used the BET method (Brunauer, Emmett and Teller gas adsorption technique Brunauer et al., 1938) to determine the surface area of their dust samples. They mention that micro-pores on the particle surface are found to contribute significantly to the surface area measurement, leading to an overestimation of the total surface area and therefore an lower value of n_s (Broadley et al., 2012, and reference therein).

Lüönd et al. (2010) investigated the immersion freezing of size-selected ($\sim$800 nm) kaolinite particles, obtained from a different company that than the one used by Murray et al. (2011). The kaolinite sample used by Lüönd et al. (2010) shows a steeper increase of ice-active surface sites compared to all other measurements and to the new immersion freezing parameterization. Murray et al. (2011) state that their
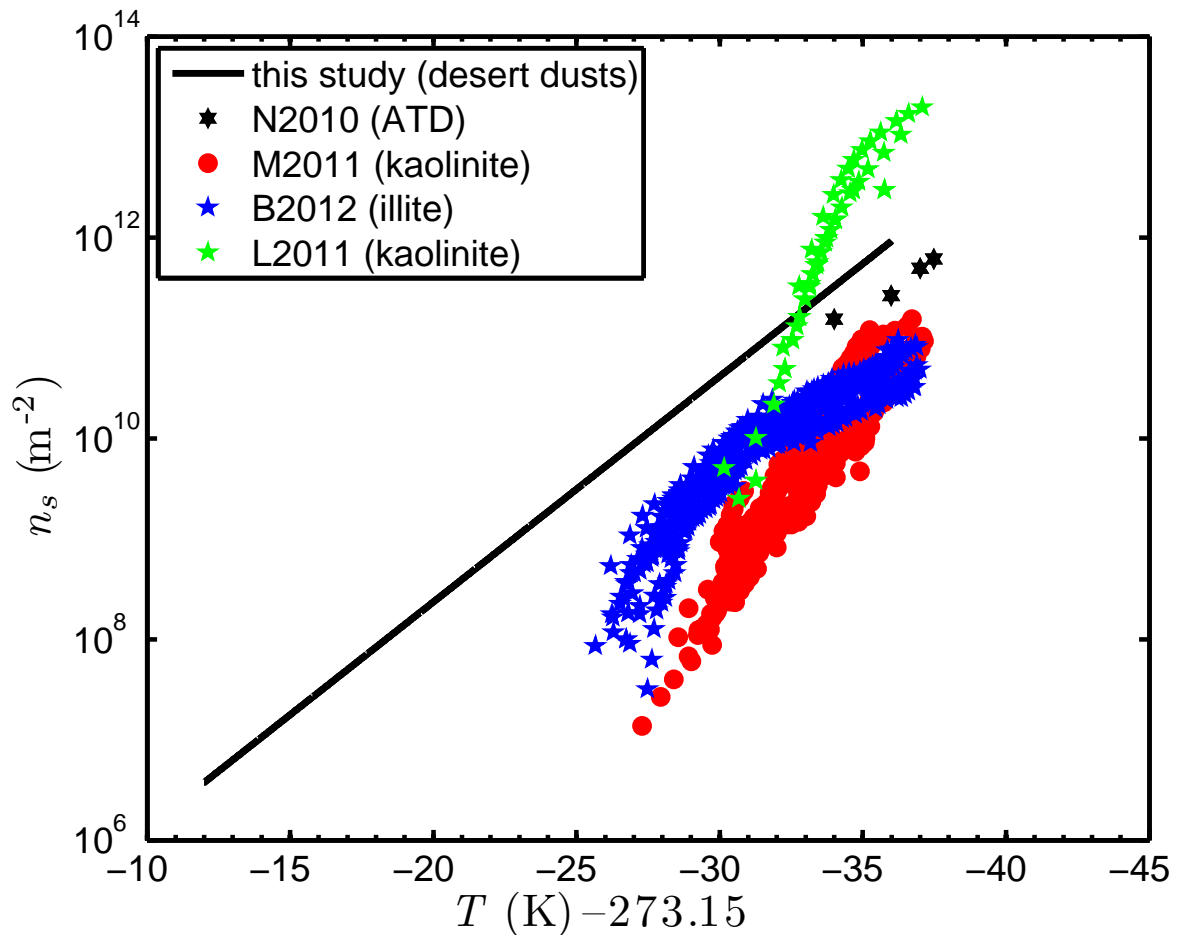
Figure 4.18.: Comparison of new immersion freezing parameterization to literature data. N2010: Niedermeier et al. (2010); M2011: Murray et al. (2011); B2012: Broadley et al. (2012); L2011: Lüönd et al. (2010).

sample has not been acid washed or chemically treated like in others, e.g. Lüönd et al. (2010).

4.5. Summary and conclusion

Immersion freezing on different desert dust particles was investigated in the AIDA cloud simulation chamber at temperatures between –12 °C and –28 °C. A parameterization of immersion freezing as a function of the dust particle surface area concentration and temperature was derived which fits the measured abundance of immersion freezing nuclei in desert dust aerosols. The parameterization can be applied in atmospheric models which include information about the dust surface area.

Based on the surface area concentration calculated from the COSMO-ART, modeled

dust particle size distribution, and the COSMO-ART modeled temperature distribution, the new parameterization was applied to calculate spatial distributions of IN number concentration during a large Saharan dust outbreak in May 2008. The results were compared to size distributions and to IN number concentrations measured at the Taunus Observatory on Mount Kleiner Feldberg in Germany for a temperature of –18 °C and a relative humidity with respect to ice of 119 % ($RH_w \approx 100$ %). The dust surface area concentration from the model simulation agreed well with the aerosol surface area concentration calculated from the measured aerosol size distributions, but the calculated IN number concentrations were about 13 times lower than the measured ones.

The parameterization derived in this thesis was also compared to three other approaches, namely the parameterizations by DeMott et al. (2010), Hoose et al. (2010) and Phillips et al. (2008) at three different temperatures based on the aerosol number concentration and surface area concentration from the COSMO-ART model simulation. The new parameterization is most sensitive to temperature variations. It gives similar results as the parameterization by DeMott et al. (2010) for a temperature of –15 °C. For –18 °C the parameterizations by Phillips et al. (2008) and Hoose et al. (2010) give IN number concentrations which are 16 to 51 times higher compared to the new parameterization, but are closer to the FRIDGE measurements. For –25 °C, the new parameterization gives about a factor 4 less IN than the parameterizations by Hoose et al. (2010), but 21 times higher IN number concentrations than the parameterization by DeMott et al. (2010).

There are several reasons that could cause the discrepancies between the calculated and measured IN number concentrations and systematic differences among the different parameterizations. Uncertainties in the modeled and measured parameters both contribute to the discrepancy between calculated and measured IN number concentrations. For example, biological particles attached to the transported dust could lead to a higher IN number concentration (Conen et al., 2011), and local dust emissions could lead to an enhanced aerosol surface area concentration compared to the calculations using the modeled Saharan dust number concentration only. Concerning the accuracy of IN number concentration measurements, DeMott et al. (2011) published a comparison between different methods and instruments for IN measurements. This comparison shows that FRIDGE measures similar ice nucleation onsets as other instruments, but comprehensive comparisons of measured IN number concentrations have not been obtained. Future comparisons of IN measuring devices are therefore

merited.

Also care has to be taken when comparing parameterizations derived from experiments with different dust samples. There is indication that milled and processed samples such as Arizona test dust (ATD) and illite have a higher ice nucleation efficiency than natural dust samples (Möhler et al., 2006), which could explain at least part of the discrepancy between different parameterizations based on different lab measurements. To further resolve the discrepancies between parameterizations and field measurements, more quantitative intercomparison studies between in situ IN measurements and model studies are needed.

Furthermore, the new parameterization was compared to laboratory measurements from the literature, conducted on different clay minerals and ATD. The discrepancies are up to a factor of one hundred. The different results could be explained by the different materials used in the laboratory studies, i.e. the composition of the natural dust samples used in this thesis might not be well represented by the clay minerals illite or kaolinite, or the dust surrogate ATD. Moreover, different dust particle sizes were used in the laboratory measurements of the previously published work. The characteristics of the individual dust samples (e.g. particle morphology and chemical composition) might be size-dependent. There were also differences in the determination of the particle surface area concentration, e.g. Murray et al. (2011) and Broadley et al. (2012) used a gas adsorption technique (BET method), whereas here the particle surface area concentration was calculated from the number size distribution. The application of different measurement techniques could also influence the results.

5. Immersion Freezing on SOA Coated Desert Dust Particles

The immersion freezing on desert dust particles coated with secondary organic aerosol (SOA) was investigated at the AIDA cloud chamber facility in the temperature range between –22 °C and –29 °C. The experiments took place within the international Aerosol–Cloud Interaction campaign ACI03 between September 28th and October 23rd 2009. Section 5.1 presents and discusses the number, surface area and mass size distributions before and after the coating procedure. The experimental results on immersion freezing are presented in section 5.2. The results are summarized and discussed in section 5.3.

5.1. Aerosol generation and characterization

The dry desert dust samples, namely Asian dust (AD) and Saharan dust (SD) (chapter 3.4), were introduced into the chamber, AIDA or APC, using a rotating brush generator as described in chapter 3.2. A cyclone impactor was applied with a 50 % cut-off between about 1 μm and 5 μm in each experiment. The SOA was generated by the ozonolysis of α–pinene at room temperature in the APC chamber or at about –22 °C in the AIDA cloud simulation chamber as described in chapter 3.5. Table 5.1 summarizes the coating conditions for each experiment. It gives the initial number concentration N_0 and the available dust particle surface area S_0 prior to the coating procedure as obtained from the log-normal fits to the combined SMPS and APS number and surface area size distribution measurements (chapter 3.2). It is indicated in which chamber and at what temperature the aerosol was coated and what amount of α–pinene was added to induce the SOA formation for the coating. The SOA yield, i.e. the mass of SOA produced per mass of reacted precursor, is estimated with the parameterization given by Saathoff et al. (2009) using the total amount of α–pinene added to the chamber and the temperature at which the dusts were coated. The

amount of α–pinene ranged from 1.6 ppb in the AIDA cloud simulation chamber to 86 ppb in the APC chamber as indicated in Table 5.1. The ozone was always added in excess to the α–pinene to ensure the complete conversion of the α–pinene to the semi-volatile oxidation products.

Figure 5.1 shows the number (row (a)), surface area (row (b)) and mass size distribution (row (c)) of AD before (first column) and after the coating step (second column) with SOA in the APC chamber for experiment ACI03_11. The solid lines each represent bimodal log-normal fits to the combined SMPS and APS data. In all experiments presented in this chapter a particle density of 2.6 g cm^{-3} and shape factors between 1.2 and 1.4 were applied to match SMPS and APS data before the coating step. A density of 2.3 g cm^{-3} and shape factors between 1.0 and 1.2 gave best results for the SOA coated dusts in the experiments. After the coating procedure (Figure 5.1, second column), a "pure" SOA nucleation mode is observed in the measurement. It is clearly separated in size from the second mode which is assumed to contain the internally mixed desert dust aerosols that can later act as CCN or IN in the expansion experiment. This nucleation mode was observed in all three AD experiments. Furthermore, the maximum of the number size distribution in row (a) of Figure 5.1, moves to larger diameters after the coating procedure. The magnitude of this shift is in the order of the estimated coating thickness. Some of the larger particle apparently get lost due too sedimentation. The time period between the two measurements is about one hour.

A very rough estimate of the coating thickness can be made by uniformly distributing the amount of SOA (μg m^{-3}) onto the available particle surface area before the coating step. In experiment ACI03_11 the calculated SOA yield is 81 μg m^{-3}. The mass size distribution after the coating step (row (c), second column) shows that there is a contribution of nucleated "pure" SOA particles to the total SOA mass. To estimate an average coating thickness this contribution of about 5 μg m^{-3} has to be subtracted from the calculated total SOA yield. For the same experiment, the dust particle surface area S_0 is 1012 μm^2 cm^{-3} before α–pinene is added. This leads to a coating thickness of about 60 nm, assuming a SOA material density of 1.25 $\pm$ 0.1 g cm^{-3}. This estimation has an uncertainty of at least a factor of two. This uncertainty is mainly based on the extrapolation of the SOA yield parameterization, the uncertainty in the actually present organic aerosol mass, the uncertainty of the available desert dust surface area, and to a minor extend the amount of SOA in the nucleation mode.

The coating thickness also depends on the particle size. The condensation of the SOA onto the dust particles occurs in the transition from the kinetic regime to the diffusion regime. Whereas the mass increase is equal for all particle sizes in the kinetic regime, in the diffusion regime (particles larger than about 0.5 μm to 1 μm) the growth rate becomes inversely proportional to the particle radius. Hence, small particles are coated thicker than larger ones which narrows the size distribution (cf. chapter 3.5). Nevertheless, the method mentioned above is used 61 to estimate the average thickness of the coating.

Figure 5.2 shows the number (a), surface area (b) and mass size distribution (c) of SOA coated AD for experiment ACI03_11 after the transfer from the APC chamber into the AIDA cloud simulation chamber. Here, the SOA coated dust mode (second mode of the distribution) is fitted only. The log-normal fit parameters for this mode, S_{dust}, $d_{S,median}$ and σ are listed in Table 5.2. While part of the aerosol is transferred from the warmer APC chamber to the cold AIDA cloud simulation chamber, the aerosol is diluted and the chemical composition can change. Furthermore, the semi-volatile SOA products can partly condense to the colder AIDA chamber walls. The aerosol number concentration of the coated dust mode is $2218\,\mathrm{cm}^{-3}$ in the APC chamber (Figure 5.1, row (a), after coating) and about $63\,\mathrm{cm}^{-3}$ after the transfer (Figure 5.2 (a)). The surface area of the SOA coated AD decreases from initially $607\,\mathrm{\mu m}^2$ cm^{-3} in the APC chamber to $44.6\,\mathrm{\mu m}^2\,\mathrm{cm}^{-3}$ in the AIDA cloud simulation chamber.

Figure 5.3 depicts the number (a), surface area (b) and mass size distribution (c) of SOA coated SD in the AIDA cloud simulation chamber for experiment ACI03_39. The SD sample was coated in the APC chamber and then transferred into the AIDA cloud simulation chamber. No nucleation of "pure" SOA occurred during the coating step. The SOA mass is calculated to be $16\,\mathrm{\mu g}\,\mathrm{m}^{-3}$ and the initial surface area S_0 is $2210\,\mathrm{\mu m}^2\,\mathrm{cm}^{-3}$. The approximated average coating thickness is therefore $6\,\mathrm{nm}$.

Figures 5.4 and 5.5 show size distribution measurements for the two remaining experiments ACI03_09 and ACI03_07. In both cases, the aerosol was coated in the AIDA cloud chamber and in both cases a "pure" SOA nucleation mode is observed after the coating procedure. Figure 5.4 shows the number (a), surface area (b) and mass size distribution (c) of AD before (left column) and after coating (right column). Figure 5.5 shows the number (a), surface area (b) and mass size distribution (c) after the coating step in the AIDA chamber only. The estimated coating thickness is $6\,\mathrm{nm}$ for experiment ACI03_09 and $11\,\mathrm{nm}$ for experiment ACI03_07.

Table 5.1.: Overview of the coating conditions for the experiments with SOA coated desert dust particles. N_0 is the initial number concentration and S_0 the initial surface area obtained from the log-normal fits to the combined number size distribution measurements with the SMPS and APS prior to the coating procedure. It is indicated in which chamber the aerosol was coated, the amount of α-pinene, the calculated SOA yield γ_{SOA}, the corresponding SOA mass, and the estimated coating thickness.

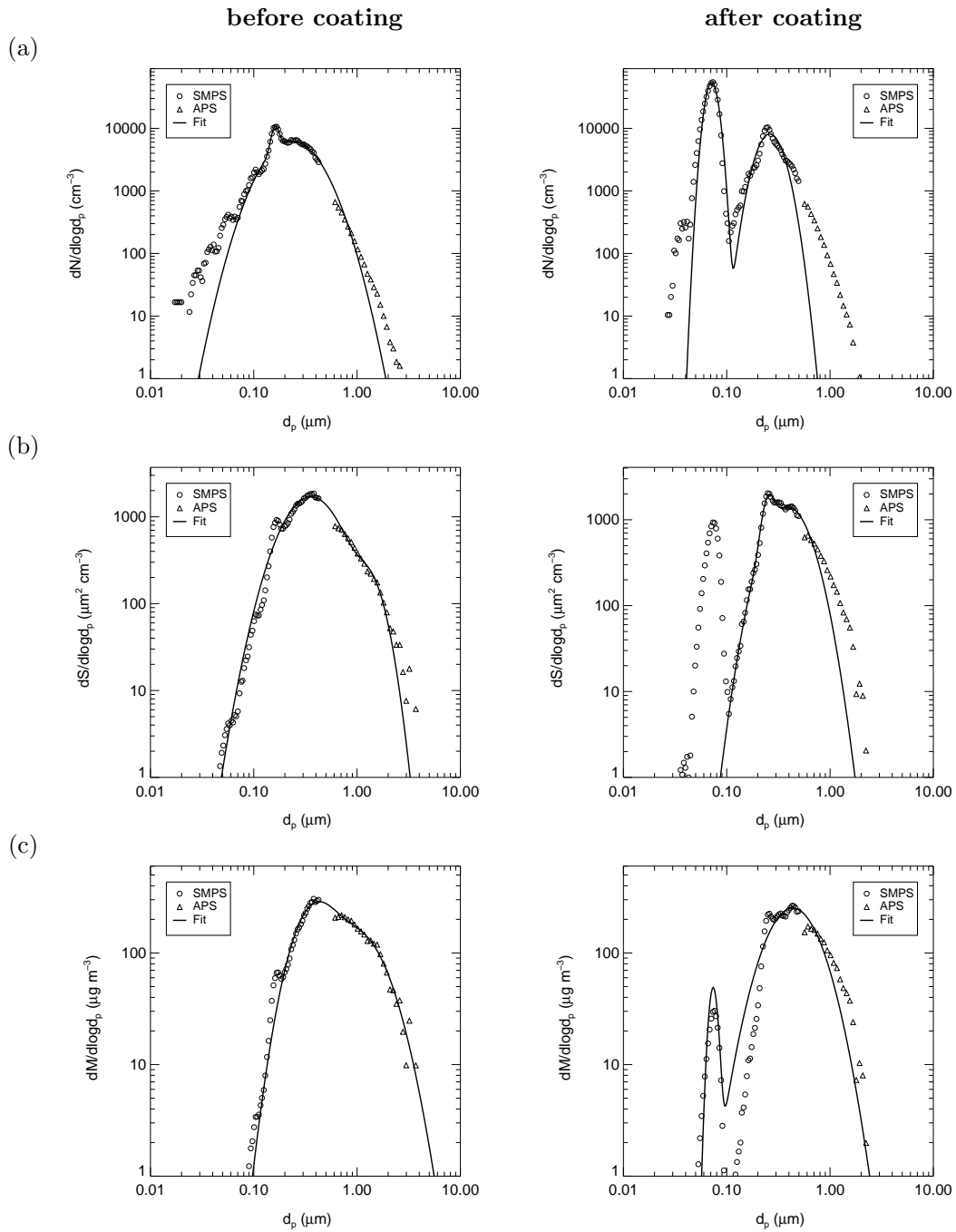| Exp. No.	Date	Dust	N_0 (cm^{-3})	S_0 $(\frac{\mu\mathrm{m}^2}{\mathrm{cm}^3})$	Where coated?	α-pinene (ppb)	γ_{SOA} (%)	SOA mass $(\frac{\mu\mathrm{g}}{\mathrm{m}^3})$	estimated coating thickness (nm)
ACI03_07	7 Oct 2009	AD	349	155	AIDA @ −22°C	1.7	20	2.2	11
ACI03_09	8 Oct 2009	AD	854	279	AIDA @ −22°C	1.6	20	2.1	6
ACI03_11	9 Oct 2009	AD	3933	1012	APC @ +22°C	86	17	81	60
ACI03_39	21 Oct 2009	SD	4655	2210	APC @ +22°C	22	13	16	6

62

Figure 5.1.: Size distribution measurements of AD in the APC chamber **before** (left column) and **after** (right column) the coating step with SOA. The aerosol was coated in the APC chamber and then transferred into the AIDA cloud simulation chamber for the expansion experiment (ACI03_11). Row (a): number size distributions; row (b): surface area size distributions; row (c): mass size distributions.
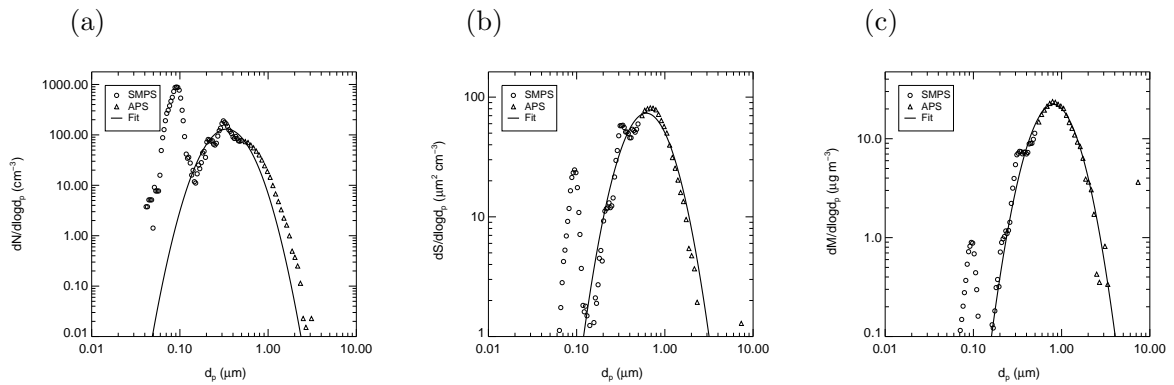
Figure 5.2.: Size distribution measurement of AD (experiment ACI03_11) in the AIDA cloud simulation chamber after the coating procedure and transfer from the APC chamber (cf. Figure 5.1). (a)–(c) show number, surface area and mass size distributions, respectively. Log-normal functions are fitted to each second mode of the size distributions (SOA coated dust mode).
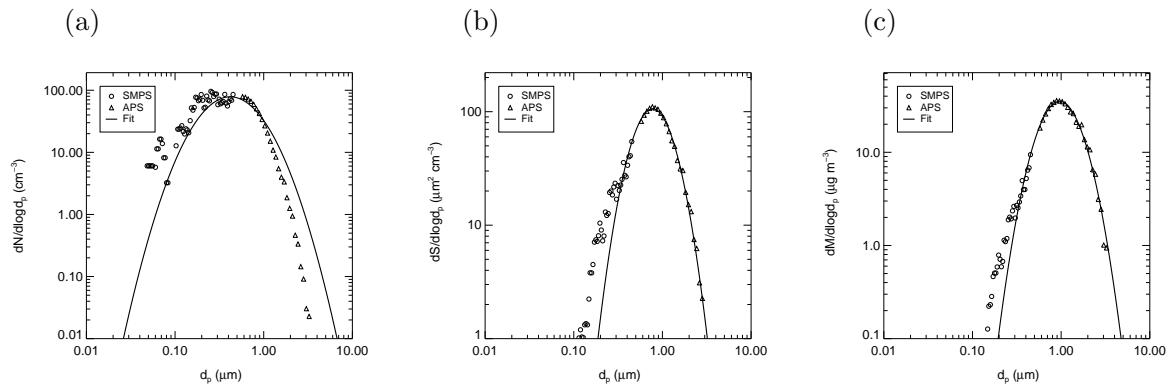

Figure 5.3.: Size distribution measurement of SOA coated SD in the AIDA cloud simulation chamber (experiment ACI03_39). The aerosol was coated in the APC chamber and then transferred into the AIDA cloud simulation chamber. (a): number size distribution; (b): surface area size distribution; (c): mass size distribution.
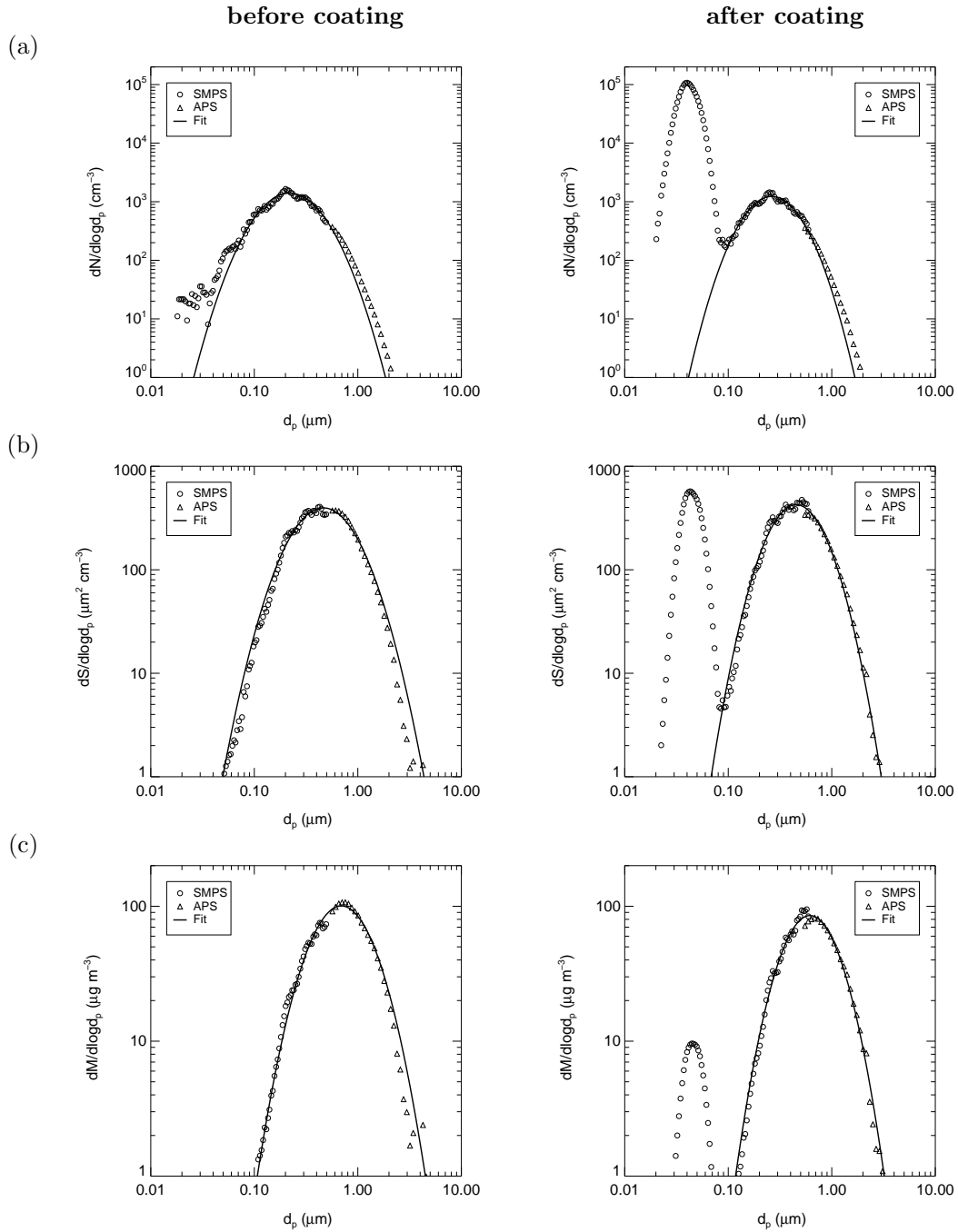
Figure 5.4.: Size distribution measurements of AD **before** (left column) and **after** (right column) the coating step with SOA. The aerosol was coated in the AIDA cloud simulation chamber (experiment ACI03_09). Row (a): number size distributions; row (b): surface area size distributions; row (c): mass size distributions.
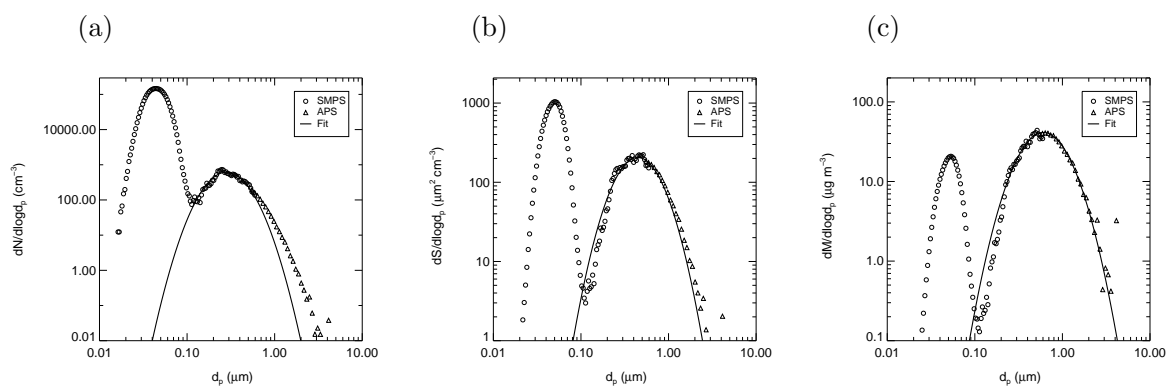
Figure 5.5.: Size distribution measurement of AD after coating in the AIDA cloud simulation chamber (experiment ACI03_07). (a)–(c) show number, surface area and mass size distributions, respectively. Log-normal functions are fitted to each second mode of the size distributions (SOA coated dust mode).

5.2. Immersion freezing results

After aerosol generation and characterization, the ice nucleation ability of the SOA coated desert dusts was examined in the AIDA cloud simulation chamber. The experimental conditions in the AIDA cloud simulation chamber at the start of each expansion experiment are summarized in Table 5.2. All four experiments started at an initial temperature of about –22 °C and atmospheric pressure. The aerosol number concentration, N_{dust}, and surface area, S_{dust}, refer to the SOA coated dust mode only. In the case of experiments with AD, where a "pure" SOA nucleation mode was always observed after the coating procedure, N_{dust} and S_{dust} refer to the second mode of the log-normal distribution (marked with * in Table 5.2). The log-normal fit parameters of the surface area size distribution are also given. S_{dust} will be used in this section to calculate the ice-active surface site density n_s, which is the number of ice-active surface sites per unit area (cf. chapter 4.2.2).

Figure 5.6 shows the AIDA time series of temperature, pressure, humidity and number concentrations for experiment ACI03_39 (SOA coated SD, no "pure" SOA nucleation mode). The experiment starts at –21.8 °C and atmospheric pressure at $t = 0$ s. The temperature decreases and the relative humidities with respect to ice, RH_i, and with respect to water, RH_w, increase during the pumping expansion (Figure 5.6, panel 1 and 2). As soon as RH_w reaches water saturated conditions, N_{tot}^{welas1} shows a steep increase in count rate due to the onset of droplet formation at about $t = 130$ s (Figure 5.6, panel 3). N_{tot}^{welas1} equals the total number concentration of droplets after droplet activation. The relative humidity is corrected by 5 % in order to match water saturated conditions during the presence of droplets (see chapter 3.3). After droplet activation, N_{tot}^{welas1} equals the total aerosol number concentration N_{tot}, showing that all SOA coated desert dust particles were activated to form droplets. N_{tot} is calculated from the initial UCPC3776 value (chapter 3.2) measured before the expansion start multiplied by the pressure dilution p/p_0, assuming a constant particle mixing ratio in the course of the experiment. Ice forms by immersion freezing shortly after the onset of droplet formation. The number concentrations of ice crystals, N_i^{welas1} and N_i^{welas2}, do not exceed $1 \, \text{cm}^{-3}$. This corresponds to an ice-active fraction of about 1 %. Panel 4 shows the particle size distribution with a size threshold between droplets and ice crystals at $d_p = 22 \, \mu\text{m}$. The expansion cooling stops after about 450 s and at 780 hPa. The droplets and ice crystals evaporate while the temperature increases again.

Figure 5.7 shows an experiment with SOA coated AD (experiment ACI03_07).

Experiment ACI03_11 behaved similarly and is therefore not shown. Experiment ACI03_07 starts at –22 °C and atmospheric pressure. The adiabatic expansion starts at time $t = 0$ s with the same pumping speed as in the previous experiment ACI03_39. The relative humidity increases due to the pumping expansion. After CCN activation, the relative humidity stays nearly constant as long as droplets are present (Figure 5.7, panel 2). N_{tot} is shown in panel 3. It has an initial value of about 60000 cm^{-3}, which includes the number of particles in the SOA nucleation mode, that formed during the coating step (see Figure 5.5 (a)). The initial number concentration of internally mixed desert dust particles N_{dust} (Table 5.2) is about 277 cm^{-3} (panel 3). This value is multiplied by the pressure dilution p/p_0 and compared to the total amount of droplets, N_{tot}^{welas1}, after cloud droplet formation. The amount of droplets activated is about a factor of seven larger compared to N_{dust}, suggesting that pure SOA particles formed droplets, too. Droplet activation is a function of supersaturation. As long as the supersaturation rises, more smaller particles are activated as cloud droplets (Pruppacher and Klett, 1997). Once the particles are activated, they continue to grow by water vapor diffusion, decreasing the supersaturation. In experiment ACI03_07 the number of SOA coated desert dust particles, N_{dust} is not high enough to decrease supersaturation, hence small "pure" SOA particles are activated to from droplets. First ice crystals already form shortly before CCN activation. In contrast to all other experiments presented in this thesis, no reference expansion was performed prior to aerosol generation in ACI03_07, ACI03_09 and ACI03_11 of this chapter. In the reference expansion experiment, the background aerosol is activated to droplets or ice crystals and precipitated from the cloud chamber. Therefore, the earlier ice nucleation was possibly induced by some background particles. The background aerosol, was in the order of 0.5 cm^{-3} in experiment ACI03_07. This number concentration is comparable to the number of ice crystals formed shortly before CCN activation. It can be excluded, that deposition mode ice nucleation on uncoated or incompletely coated AD occurred, since no deposition nucleation was observed before CCN activation in the experiments with pure AD dust particles in this temperature range (cf. experiments discussed in chapter 4). Pure liquid SOA particles are not observed to form ice heterogeneously (Möhler et al., 2008; Prenni et al., 2009). Most ice formation occurs shortly after the CCN threshold is reached due to immersion freezing of the SOA coated desert dust particles. The maximum activated fraction reached in this experiment (N_i^{welas2} divided by N_{tot}^{welas1}) is about 1 %. The particle size distribution is shown in panel 4. The size threshold to distinguish droplets from ice crystals is set

to $d_p = 12\,\mu$m. The gaps in the N_i^{welas1} data are due to measurement artifacts.

Figure 5.8 shows the time series for experiment ACI03_09. In contrast to all three other experiments discussed in this chapter, the rate of pressure decrease is not constant. This is due to the synthetic air supply, which wasn't accidentally stopped until about 200 s after the start of the expansion experiment (panel 1). The initial N_{tot} is about 33000 cm^{-3} due to the nucleation of pure SOA particles during the coating step in the AIDA cloud simulation chamber. The log-normal fit to the coated dust mode, N_{dust}, gives about 657 cm^{-3} (panel 3). A minor fraction of ice forms about 20 s before the CCN activation threshold is reached. As discussed before, this ice nucleation could be induced by the background aerosol. Droplet formation is initiated as soon as water saturation is reached at about $t = 270$ s, and ice forms shortly after this time. The number of activated droplets, N_{tot}^{welas1} after droplet activation, roughly equals the number of SOA coated dust particles, N_{dust}. The maximum ice-active fraction in ACI03_09 is about 1 % like in all experiments listed in Table 5.2.

The experimental results are interpreted in terms of ice-active surface site density (n_s). n_s is calculated from the number concentration of ice crystals from the welas2 instrument, N_i^{welas2}, divided by the particle surface area of SOA coated dust particles, S_{dust} (cf. chapter 4.2.2). The values for S_{dust} are listed in Table 5.2. Figure 5.9 shows the ice-active surface site density n_s versus decreasing temperature of SOA coated desert dust particles in comparison to the results for uncoated desert dusts from chapter 4 (cf. Figure 4.8). To be consistent, the data was treated the same way as in chapter 4 (averages over 60 s, starting after droplet formation and continuing as long as N_i^{welas2} is still increasing). The exponential function is a fit to all uncoated dusts examined in chapter 4. The function describes the average ice-active surface site density n_s versus temperature. Concerning the overall scatter in this plot, the results from this chapter are well represented by the same fit function. However, a closer look at the experiments with coated desert dusts (Figure 5.10) reveals that the coated dusts show lower values of n_s by more than a factor two compared to the uncoated.

Figures 5.11 and 5.12 again show the ice-active surface site densities n_s on the SOA coated desert dusts as a function of decreasing temperature for dusts coated in the APC chamber and in the AIDA cloud simulation chamber, respectively. The reason for this distinction is that the chemical composition of the coating might be different for aerosols coated in the APC chamber compared to those coated in the AIDA cloud simulation chamber. More semi-volatile organic material should partition into the SOA coating layer at the lower temperatures in the AIDA cloud simulation chamber.

In these figures, n_s is plotted on a linear scale. Other than in Figure 5.9 and Figure 5.10 the data was not averaged over 60 s. The data includes ice that is formed after droplet activation only. The time period is about the same as in Figure 5.9. The error bars in Figures 5.11 and 5.12 represent a relative error of 50 %, which corresponds to the square root of the sum of squared relative errors in N_i^{welas2} and S_{dust}. The relative error is estimated to be 30 % for N_i^{welas2} and 40 % for S_{dust}.

In Figure 5.11 experiments ACI04_19 (with AD) and ACI04_10 (with SD) from chapter 4 are shown for comparison to the experiments with SOA coated desert dusts, ACI03_11 (ADcSOA) and ACI03_39 (SDcSOA). AD and SD were coated in the APC chamber and the estimated coating thicknesses are 60 nm for ACI03_11 and 6 nm for ACI03_39 (cf. Table 5.1). The initial temperatures in the experiments with uncoated dusts, ACI04_19 and ACI04_10, are –20.1 °C and –19.3 °C, respectively (cf. Table 4.2 in chapter 4.1). Experiments ACI03_11 and ACI03_39 both start at about –22 °C. For this reason the data is shifted by about 2 °C towards warmer temperatures for the experiments with uncoated desert dusts in Figure 5.11. In the experiment with uncoated AD (experiment ACI03_19; blue triangles), n_s increases from $10^9 \, \mathrm{m}^{-2}$ at –24 °C to $12 \cdot 10^9 \, \mathrm{m}^{-2}$ at –26.8 °C. In the experiment with SOA coated AD (experiment ACI03_11; blue stars) n_s increases from initially $7 \cdot 10^9 \, \mathrm{m}^{-2}$ at –26.5 °C to $17 \cdot 10^9 \, \mathrm{m}^{-2}$ at –27.3 °C and is steeper compared to the uncoated case. The comparison of the uncoated SD (experiment ACI04_10; red triangles) to the coated SD experiment (experiment ACI03_39; red stars) shows an effect of the SOA coating on the ice nucleation ability of the SD sample in the order of about factor two at around –26 °C to –26.5 °C.

Figure 5.12 depicts two experiments with AD coated in the AIDA cloud simulation chamber (ACI03_09 and ACI03_07). As in Figure 5.12, experiment ACI04_19 from chapter 4 is shown for comparison. The "thinner" coating in experiment ACI03_09 corresponds to an estimated coating thickness of 6 nm, the "thicker" coating in experiment ACI03_07 to 11 nm (section 5.1 and Table 5.1). As mentioned before, this estimation has an uncertainty of at least a factor of two. Also the coating thickness varies with particle size. Therefore, "thick" and "thin" only refer to an estimated average coating thickness. In experiment ACI03_07 ("thicker" coating; grey stars) n_s increases from initially $7 \cdot 10^9 \, \mathrm{m}^{-2}$ to $17 \cdot 10^9 \, \mathrm{m}^{-2}$ within about 1.5 °C. The n_s values are similar to those in the uncoated case (experiment ACI03_19; blue triangles), although the increase is slightly steeper. In experiment ACI03_09 ("thinner" coating, blue stars), the number of ice-active sites increases from about $0.2 \cdot 10^9 \, \mathrm{m}^{-2}$

at –26.3 °C to about $0.7 \cdot 10^9 \, \mathrm{m}^{-2}$ at –27.2 °C. The n_s values are less by about a factor of two compared to the uncoated case. As discussed before in the time series of experiment ACI03_09 (section 5.1), the synthetic air supply wasn't turned off by accident until the first couple of minutes of the experiment, which might effect the result.

Table 5.2.: Overview of immersion freezing experiments with SOA coated desert dust particles. p_0 and T_0 are the pressure and temperature inside the AIDA cloud simulation chamber at the start of the expansion experiment. N_{dust} and S_{dust} refer to the aerosol number concentration and surface area concentration of coated desert dust particles prior to the expansion run. In case of all three experiments with AD, where a "pure" SOA nucleation mode was observed, N_{dust} and S_{dust} refer to the second mode of the log-normal distribution (marked with *). $d_{S,median}$ and σ are the median diameter and geometric standard deviation of the surface area size distribution, respectively.

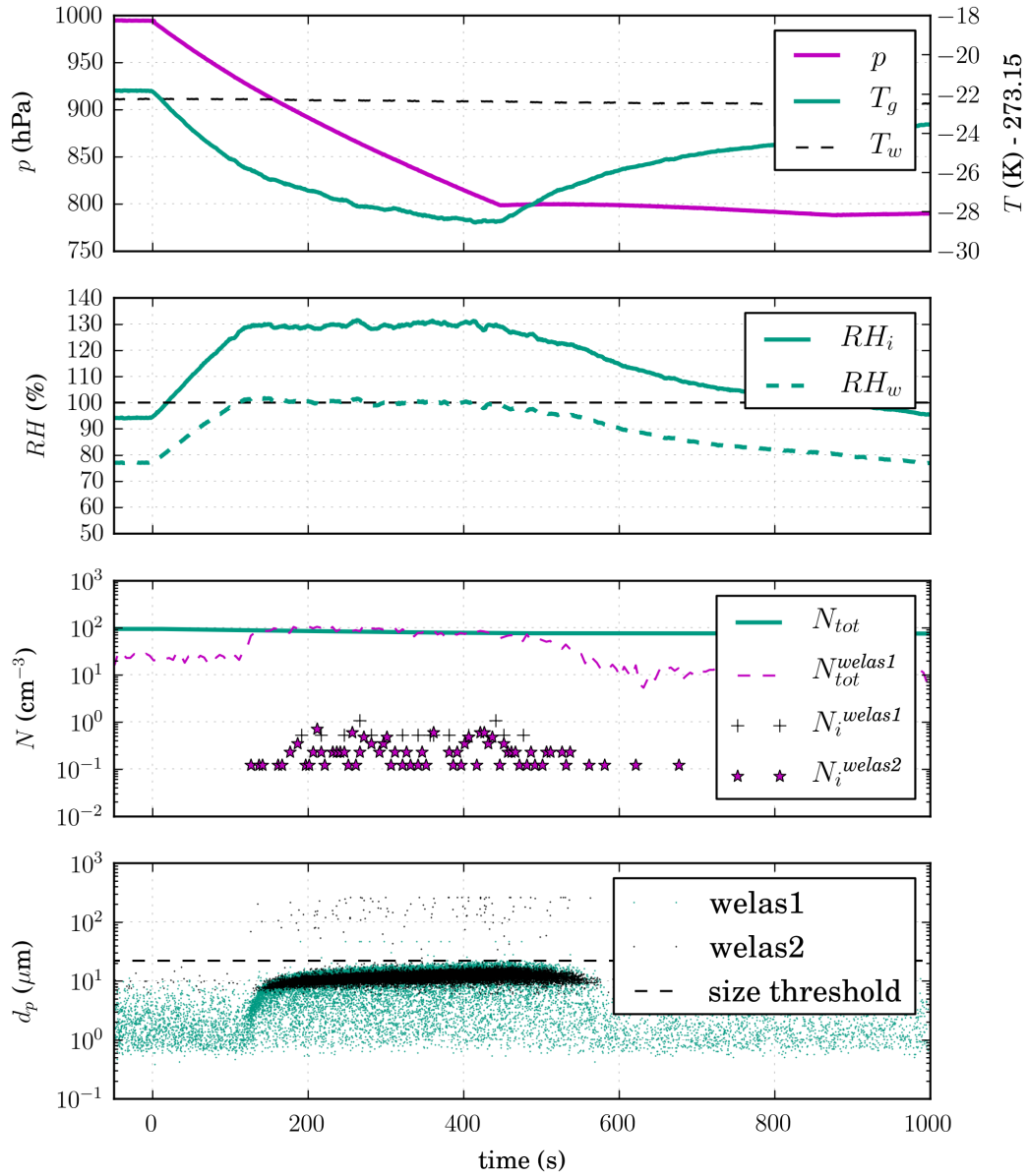| Exp. No.	Aerosol	p_0 (hPa)	T_0 (K) − 273.15	N_{dust} (cm^{-3})	S_{dust} µm^2 cm^{-3}	$d_{S,median}$ (µm)	σ
ACI03_07	ADcSOA	1002.1	−22.0	277*	117*	0.45	1.68
ACI03_09	ADcSOA	1002.0	−22.0	657*	252*	0.45	1.72
ACI03_11	ADcSOA	1007.0	−22.0	63*	45*	0.62	1.75
ACI03_39	SDcSOA	994.4	−21.8	94	54	0.78	1.59

Figure 5.6.: AIDA time series of experiment ACI03_39 with SOA coated SD. Initial temperature is –21.8 °C. **Panel 1**: pressure p, wall temperature T_w, gas temperature T_g; **panel 2**: relative humidity with respect to water (RH_w) and ice (RH_i); **panel 3**: number concentration of total aerosol N_{tot} and ice crystals N_i^{welas1} and N_i^{welas2}. N_{tot}^{welas1} equals the total number concentration of cloud droplets after cloud formation at about 130 s; **panel 4**: particle size distribution with size threshold between droplets and ice crystals at $d_p = 22\,\mu$m.
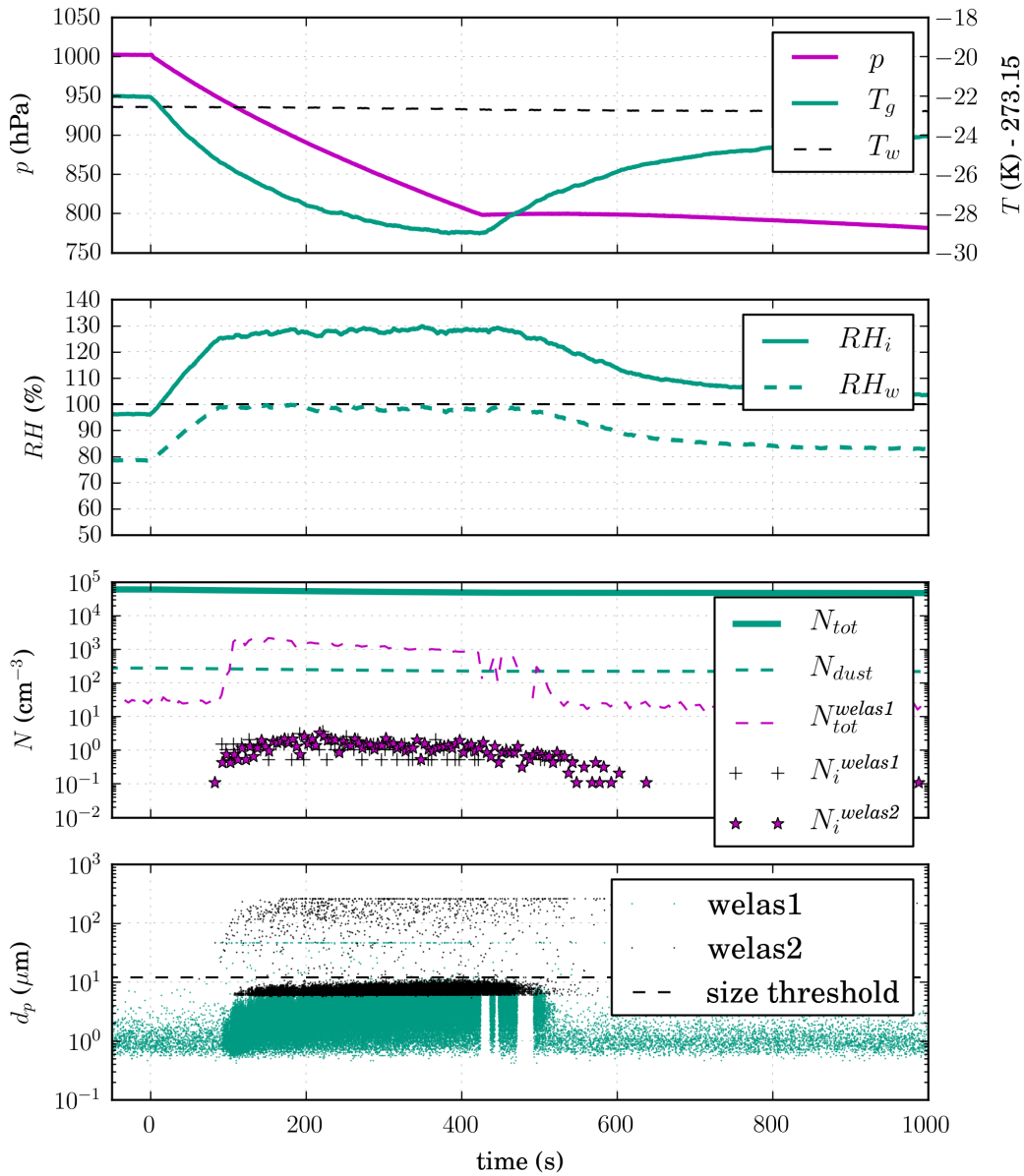
Figure 5.7.: AIDA time series of experiment ACI03_07 with SOA coated AD. Initial temperature is –22 °C. **Panel 1**: pressure p, wall temperature T_w, gas temperature T_g; **panel 2**: relative humidity with respect to water (RH_w) and ice (RH_i); **panel 3**: number concentration of total aerosol N_{tot} (nucleated "pure" SOA particles and SOA coated dust particles) and ice crystals N_i^{welas1} and N_i^{welas2}. N_{dust} equals the number concentration of SOA coated desert dust particles only. N_{tot}^{welas1} equals the total number concentration of cloud droplets after cloud formation at about 90 s; **panel 4**: particle size distribution with size threshold between droplets and ice crystals at $d_p = 12\,\mu m$.
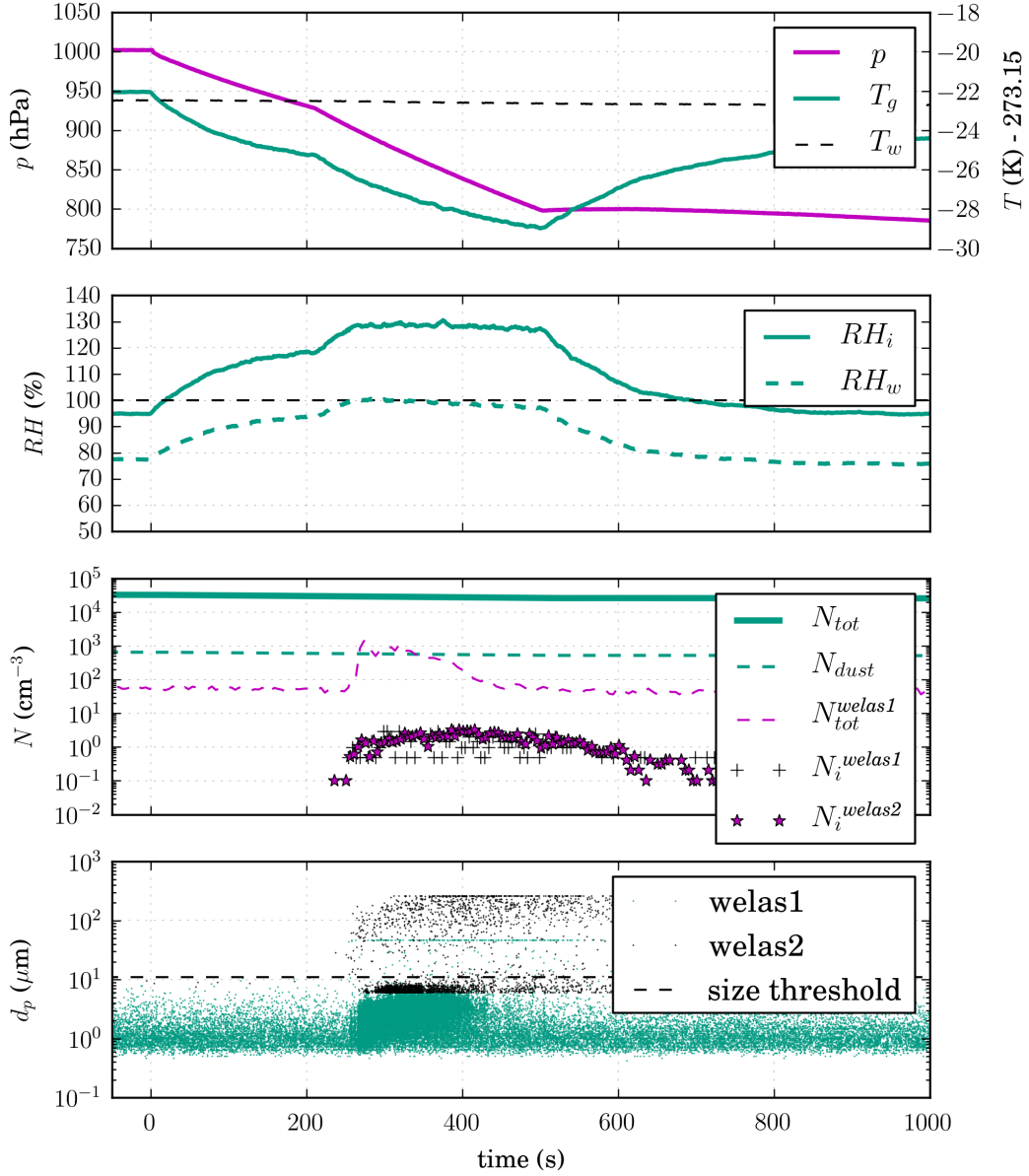
Figure 5.8.: AIDA time series of experiment ACI03_09 with SOA coated AD. Initial temperature is –22 °C. **Panel 1**: pressure p, wall temperature T_w, gas temperature T_g; **panel 2**: relative humidity with respect to water (RH_w) and ice (RH_i); **panel 3**: number concentration of total aerosol N_{tot} (nucleated "pure" SOA particles and SOA coated dust particles) and ice crystals N_i^{welas1} and N_i^{welas2}. N_{dust} equals the number concentration of SOA coated desert dust particles only. N_{tot}^{welas1} equals the total number concentration of cloud droplets after cloud formation at about 250 s; **panel 4**: particle size distribution with size threshold between droplets and ice crystals at $d_p = 11\,\mu m$.
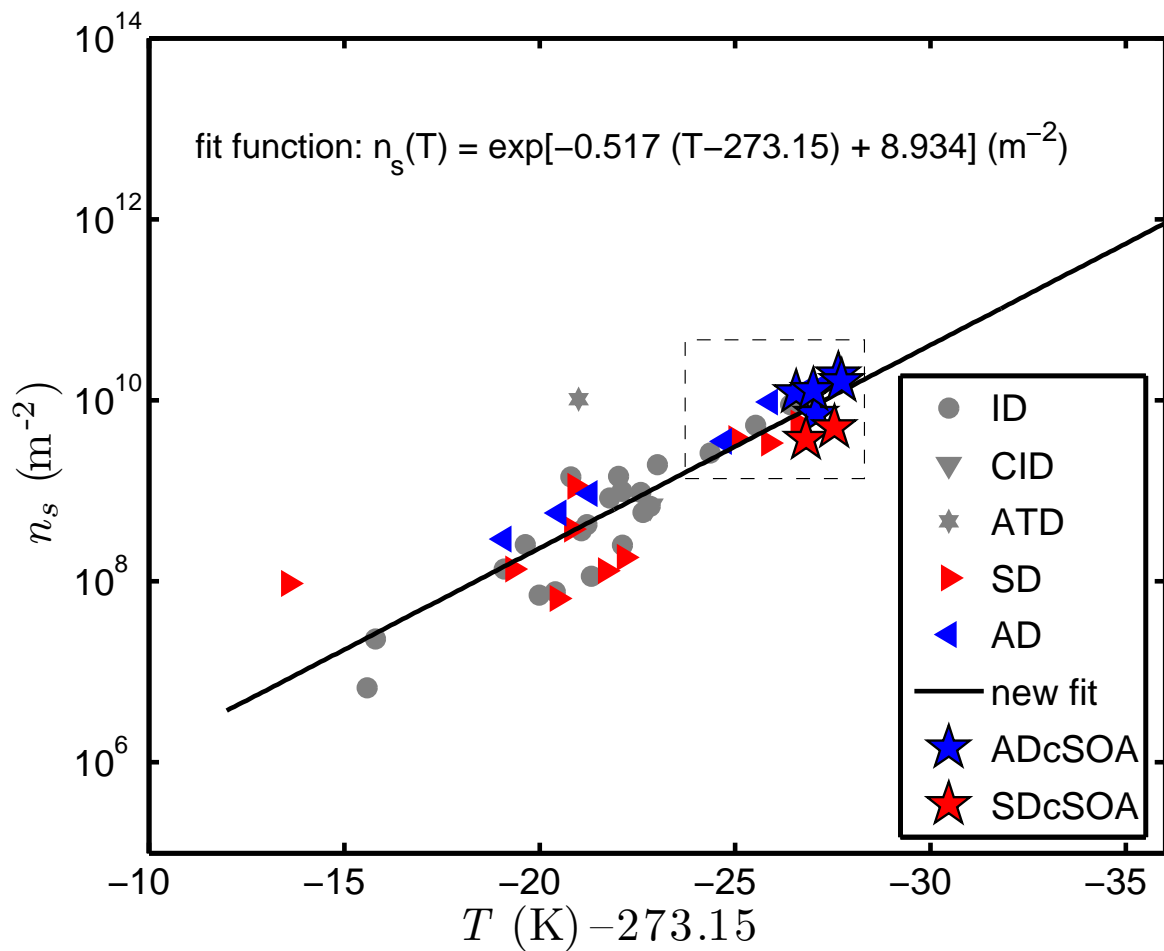
Figure 5.9.: Ice-active surface site densities n_s for uncoated dusts (results from chapter 4; cf. Figure 4.8, chapter 4.2.2) including the calculated n_s values from the experiments with SOA coated desert dust particles.
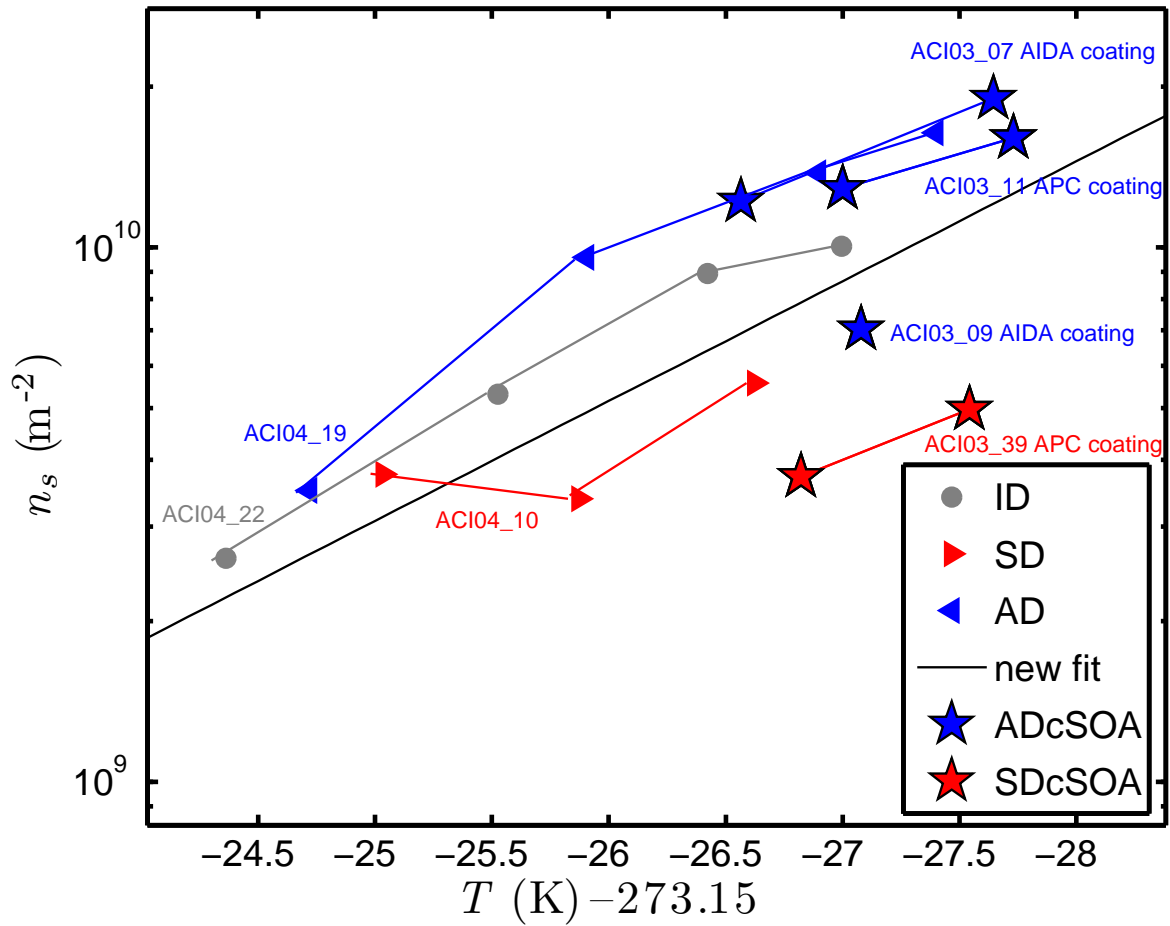
Figure 5.10.: Ice-active surface site densities n_s of SOA coated and plain desert dust particles (results from chapter 4). Close up of the area in the box in Figure 5.9.

Figure 5.11.: Ice-active surface site densities n_s of SOA coated (triangles) and un-coated desert (stars) dust particles (same as in Figure 5.9 and Figure 5.10, not averaged) on a linear scale. The plot compares desert dust particles that were coated in the APC chamber only. The relative error in n_s is 50 % (see text for more details). For clarity, only a few error bars are plotted.
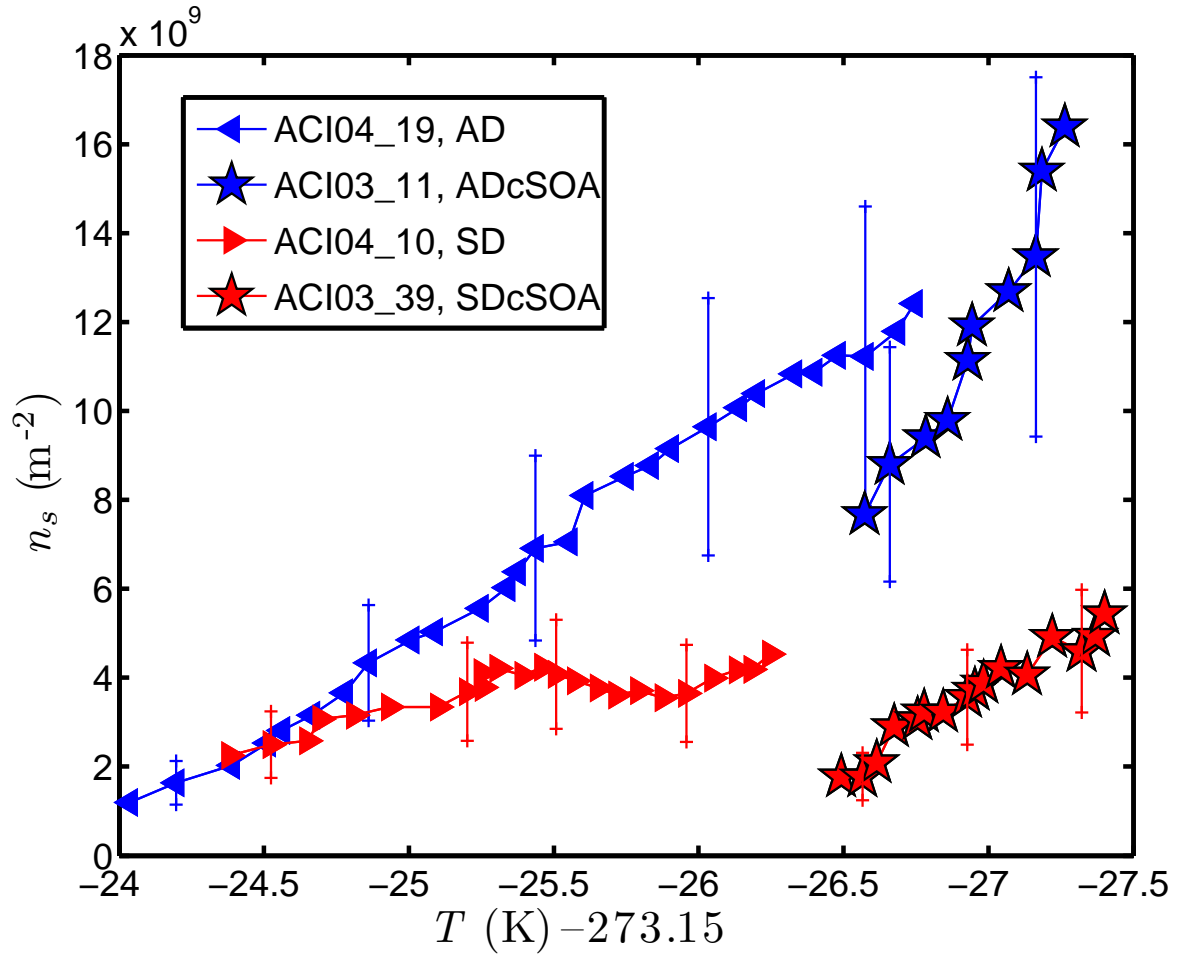
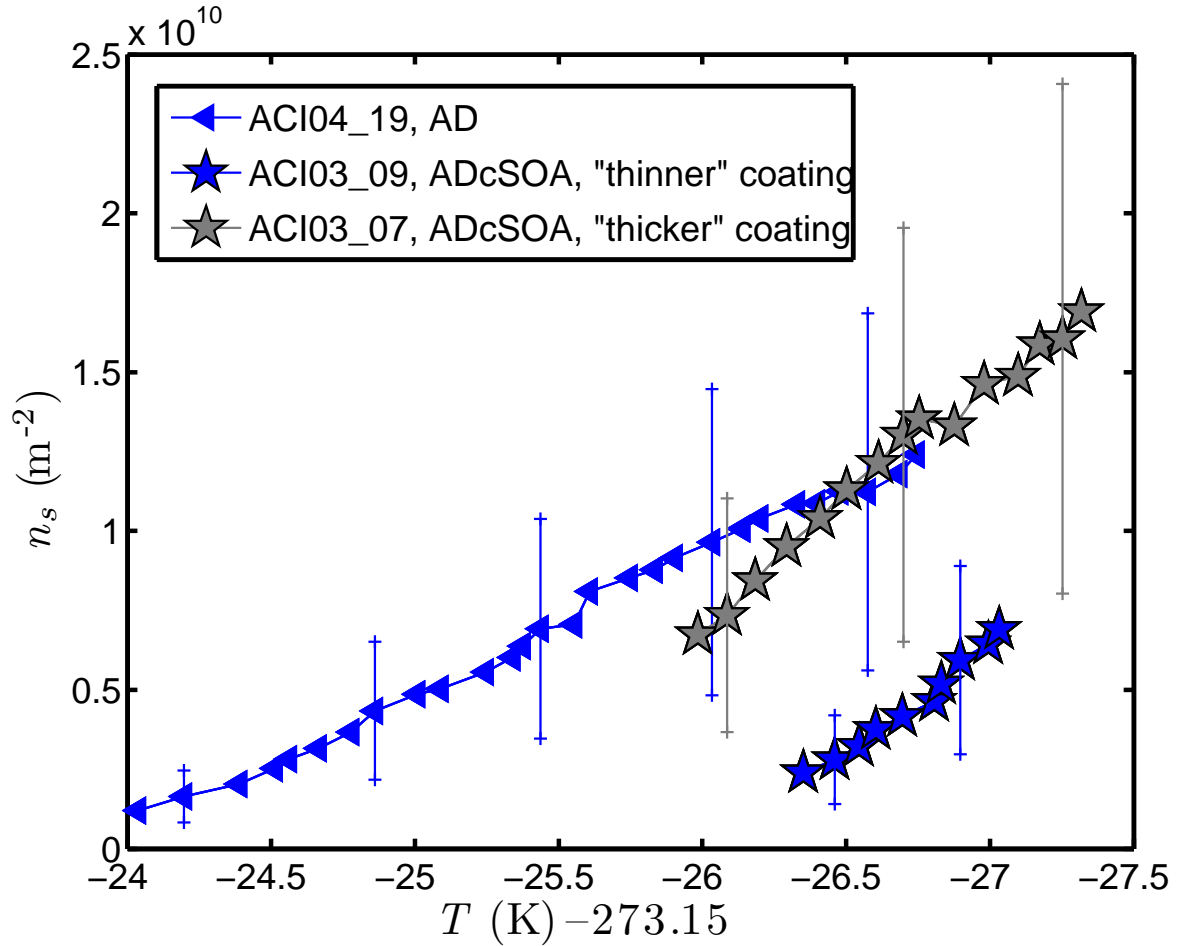Figure 5.12.: Ice-active surface site densities n_s of SOA coated (triangles) and un-coated desert (stars) dust particles (same as in Figure 5.9 and Figure 5.10, not averaged) on a linear scale. The plot compares desert dusts particles that were coated in the AIDA cloud simulation chamber only. The relative error in n_s is 50 % (see text for more details). For clarity, only a few error bars are plotted.

5.3. Summary and conclusion

The immersion freezing on Asian dust (AD) and Saharan dust (SD) coated with secondary organic aerosol (SOA) was investigated in the AIDA cloud simulation chamber in the temperature range between –22 °C and –29 °C. Four experiments were presented. The dust samples were either coated at room temperature in the Aerosol Preparation and Characterization (APC) chamber or in the AIDA cloud simulation chamber at about –22 °C. A "pure" SOA nucleation mode was observed after the coating procedure in all three experiments with AD. In the experiment with SD, no SOA nucleation mode was observed.

Time series of immersion freezing experiments in the AIDA cloud simulation chamber were presented. In the experiment with SD, all SOA coated dust particles were activated to form droplets, thus the total number concentration of SOA coated dust particles equaled the total number of droplets after droplet formation. In two out of three experiments with SOA coated AD, the number concentration of cloud droplets exceeded the number of coated desert dust particles. In these two experiments, the initial number concentration of coated desert dust particles was much less compared to the experiment with SOA coated AD, where the number of cloud droplets activated equaled the number of dust particles in the dust mode. Since droplet activation is mainly a function of supersaturation and particle size, the number concentration of the coated desert dust particles, which are larger than the pure SOA particles, was apparently too small to immediately decrease supersaturation after droplet activation, hence some of the largest "pure" SOA particles were also activated as droplets. Ice formation occurred shortly after or shortly before the cloud condensation nucleation threshold in the case of SD and AD, respectively. In the latter case, ice nucleation induced by background particles could have contributed to ice formation. Unfortunately, no experiments were conducted on pure SOA particles in this temperature range during this campaign. But other studies show that "pure" liquid SOA particles do not form ice heterogeneously (e.g. Möhler et al., 2008; Prenni et al., 2009). The highest ice-activated aerosol fraction in all experiments discussed in this chapter was about 1 %.

The results were interpreted in terms of ice-active surface site densities n_s. In general, the n_s results of the coated dust are well represented by the exponential fit function derived for uncoated desert dusts. However, a closer look at the data showed some effect of the SOA coating on the ice nucleation ability of desert dusts. The

result were distinguished according to the chamber they were coated in. The reason was the expected difference in chemical composition, due to the different coating temperatures. Experiments with uncoated dusts from the previous chapter 4, were used for the comparison to the SOA coated dust experiments. In general, the thinly coated AD and SD samples showed a suppression in the immersion mode ice nucleation by more than a factor of two in n_s. Thickly coated desert dust samples on the other hand, showed an enhanced freezing behavior (slightly larger slope) in comparison to the uncoated cases. Reasons could be

(1) that the larger amount of SOA coating covers a larger surface area fraction with thick SOA layers which take-up water at increasing relative humidity by hygroscopic growth and therefore activates a larger amount of immersion freezing sites below CCN activation compared to thinner coatings.

(2) Another aspect could be the formation of glasses—amorphous solid material—from organic liquid compounds. In this case, ice formation would occur on solid compounds by the deposition mode ice nucleation at some point of the experiment. The glass transition of organics and its relevance in the atmosphere has been investigated and discussed in recent publications, (e.g. Zobrist et al., 2008; Murray et al., 2010; Koop et al., 2011). Zobrist et al. (2008) suggest that organic-rich aerosols are capable of forming glasses, thus influencing the formation of clouds. However, their results are limited to cirrus cloud conditions. Koop et al. (2011) investigated the glass transition temperatures of a large variety of different species and show experimental evidence for the formation of glasses under ambient conditions. SOA generated by the ozonolysis of α–pinene has not yet been investigated for its glass transition in the temperature range –22 °C and –29 °C. Further studies are needed to verify the assumption that heterogeneous ice nucleation on glassy aerosols might influence the results presented in this chapter.

As a final remark, it has to be taken into account, that also larger differences in the freezing behavior were found among certain desert dusts (cf. chapter 4), that were greater than a factor of two. Therefore, the parameterization suggested in chapter 4 is suitable to describe the average freezing behavior of SOA coated desert dust particles.

6. Effect of SOA Coatings on the Deposition Ice Nucleation on Desert Dust Particles

Heterogeneous ice nucleation experiments on Asian dust (AD) and Saharan dust (SD) particles, coated with secondary organic aerosol (SOA) were accomplished at cirrus cloud temperatures during the Aerosol–Cloud Interaction campaign ACI03. In the following, three AIDA cloud simulation chamber experiments are presented and compared. The experiments were performed in the temperature range –39 °C to –45 °C. Section 6.1 describes the aerosol generation and characterization. Section 6.2 presents the results of the experiments. The findings are summarized in section 6.3.

6.1. Aerosol generation and characterization

The desert dust samples were dispersed with the rotating brush generator RBG–1000 and a dispersion nozzle into a flow of dry synthetic air. The resulting dust aerosol was then passed to the aerosol preparation and characterization (APC; chapter 3.1) chamber and coated with SOA as described before in chapter 5.1. Table 6.1 summarizes the coating conditions for the experiments with AD and SD, respectively. The table gives the initial dust particle surface area S_0 prior to the coating procedure. It is obtained from the log-normal distribution fits to the combined scanning mobility particle sizer (SMPS) and aerodynamic particle sizer (APS) size distribution measurement. A particle density of $2.6\,\mathrm{g\ cm^{-3}}$ and a shape factor of 1.2 for the AD sample and 1.4 for the SD sample were applied to match the SMPS and APS measured size distributions (cf. chapters 3.2 and 4.2.1). Furthermore, the amount of α–pinene added to the APC chamber to generate the coating and the estimated SOA yield are listed (cf. chapters 3.5 and 5.1). The coating thickness is estimated by equally distributing the amount of SOA material over the available dust particle surface area (cf. chapter

5.1). The estimated coating thickness is 5 nm in case of the AD sample and 9 nm in case of the SD sample. This estimation has an uncertainty of at least a factor of two. After the coating procedure, the respective aerosol was transferred into the AIDA cloud simulation chamber for the ice nucleation experiments at low temperatures. Figure 6.1 shows surface area size distributions of uncoated AD (experiment ACI03_14), SOA coated AD (experiment ACI03_18), and SOA coated SD (experiment ACI03_26), measured in the AIDA chamber prior to the expansion experiment. Good agreement between the SMPS and APS measured size distributions was found for a density of $2.3\,\mathrm{g\,cm^{-3}}$ and a shape factor of 1.0 for both, the SOA coated AD and the SOA coated SD sample, respectively. The log-normal fit parameters are listed in Table 6.2. Unfortunately, no experiment with uncoated SD was performed at this low temperatures. Therefore, a direct comparison to the experiment with SOA coated SD can not be made. In the following, the time series of the three experiments will be presented. The experimental results will be interpreted in terms of ice-active surface site densities (n_s; cf. chapter 4.2.2).
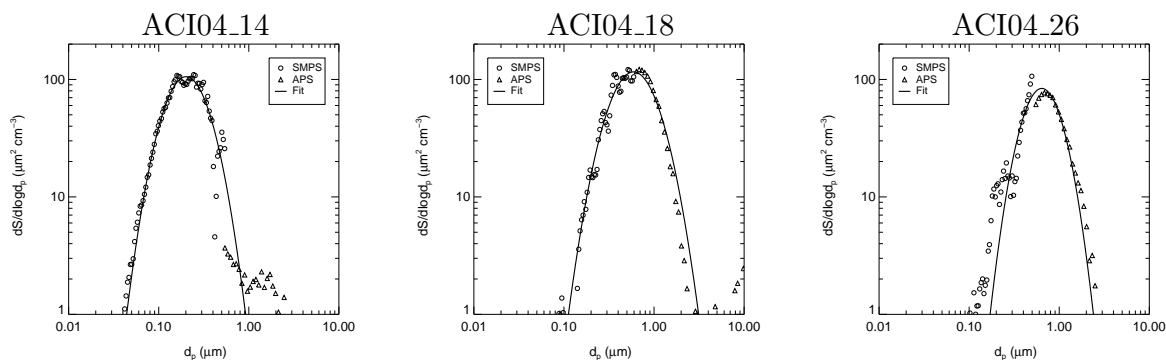

Figure 6.1.: Surface area size distribution of uncoated AD (experiment ACI03_14), SOA coated AD (experiment ACI03_18), and SOA coated SD (experiment ACI03_26), measured in the AIDA chamber prior to the expansion experiment.

Table 6.1.: Overview of the coating conditions for the two experiments with SOA coated Asian and Saharan dust particles, respectively. S_0 is the initial surface area concentration. The coating temperature, the amount of α–pinene added to the APC chamber, the calculated SOA yield γ_{SOA}, the corresponding SOA mass, and the estimated coating thickness are listed.

Exp. No.	Date	Aerosol	S_0	Where coated?	α–pinene (ppb)	γ_{SOA} (%)	SOA mass ($\frac{\mu g}{m^3}$)	estimated coating thickness (nm)
ACI03_18	13 Oct 2009	ADcSOA	2561	APC @ +22 °C	22.5	13	16	5
ACI03_26	15 Oct 2009	SDcSOA	1433	APC @ +22 °C	22.4	13	16	9

6.2. Experimental results

Table 6.2 summarizes the experimental conditions of all three experiments discussed in this chapter. All experiments started at about the same initial temperature and were performed at the same pumping speed. A temperature range of $6\,°C$ was covered in each experiment.

Figure 6.2 shows the experiment with uncoated AD (experiment ACI03_14). The initial temperature of the experiment is $–38.5\,°C$. The expansion cooling is induced at time $t = 0\,s$ by pumping at a constant rate (panel 1). For this experiment, no TDL measurement of water vapor pressure was available (section 3.2). Therefore, the relative humidity calculated from the frost point temperature measured with the chilled–mirror hygrometer, MBW_w and MBW_i, is shown in panel 2 (section 3.2). As mentioned and shown before in chapter 3.3, MBW_w and MBW_i compare well to the relative humidity from the TDL measurement until ice crystal formation. Thereafter, the difference between the total water measured with the chilled–mirror hygrometer and the gas–phase water measured with the TDL increases due to the nucleating and growing ice particles. The total number concentrations of dust, N_{tot}, and ice particles, N_i^{welas1} and N_i^{welas2}, are shown in panel 3. First ice crystals are formed after $53\,s$ (panel 3 and 4), and $MBW_i = 110\,\%$. The size threshold for the distinction between ice crystals and background particles is set to $10\,µm$ in this experiment. The number concentration of ice particles, N_i^{welas1} and N_i^{welas2}, remains almost constant

Table 6.2.: Overview of the cirrus regime ice nucleation experiments. p_0 and T_0 are the pressure and temperature inside the AIDA cloud simulation chamber at the start of the experiment. N_{dust} refers to the total number concentration and S_{dust} to the total surface area of dust particles prior to the expansion run. $d_{S,median}$ and σ are the median diameter and geometric standard deviation of the log-normal fit to the surface area size distribution, respectively.

Exp. No.	Aerosol	p_0 (hPa)	T_0 (K) -273.15	N_{dust} (cm^{-3})	S_{dust} $\left(\frac{µm^2}{cm^3}\right)$	$d_{S,median}$ (µm)	σ
ACI03_14	AD	1004.5	–38.5	930.4	57	0.20	1.65
ACI03_18	ADcSOA	1014.7	–38.7	106.7	68	0.59	1.72
ACI03_26	SDcSOA	1014.2	–38.7	80.2	41	0.64	1.56

until the pumping expansion is stopped at about $500\,\mathrm{s}$ and $800\,\mathrm{hPa}$.

Figure 6.3 depicts the experiment run with SOA coated AD (experiment ACI03_18). Two ice nucleation events are observed within this experiment (panel 3 and 4). The first mode occurs at about $62\,\mathrm{s}$ and a relative humidity with respect to ice of about $RH_i = 112\,\%$. The size threshold between droplets and ice crystals is at $d_p = 9\,\mu\mathrm{m}$. The second mode occurs after $170\,\mathrm{s}$, close to water saturation ($RH_w \approx 95\,\%$), and $RH_i = 138\,\%$. At about $RH_i = 114\,\%$ and $T = -40.8\,^\circ\mathrm{C}$, $0.1\,\%$ of the particles are activated to form ice crystals. The humidity (RH_i and RH_w in panel 2) is depleted quickly after the second mode appears.

Figure 6.4 shows the time series for the experiment with SOA coated SD (experiment ACI03_26). As in experiment ACI03_18, this experiment exhibits two distinct ice nucleation modes with mode one occurring after about $80\,\mathrm{s}$ and RH_i close to $120\,\%$ (panel 3 and 4). The size threshold between droplets and ice crystals is at $d_p = 15\,\mu\mathrm{m}$ in this experiment. An activated fraction of $0.1\,\%$ is exceeded at about $RH_i = 126\,\%$ and $T = -41.8\,^\circ\mathrm{C}$. The second mode occurs after about $190\,\mathrm{s}$, again close to water saturation and $RH_i = 144\,\%$.

The first mode in all three experiments is likely to be due to deposition mode ice nucleation. In case of the experiments with SOA coating, ACI03_18 and ACI03_26, deposition nucleation could occur on uncoated or incompletely coated desert dust particles. The second increase in ice crystal number concentration in experiment ACI03_14 with uncoated AD is possibly due to further deposition mode ice nucleation of smaller particles that become activated. The second ice nucleation mode observed in the case of the coated dusts occurs close to water saturation. The water soluble material presumably enhances water uptake and the particles nucleate ice via immersion freezing.

Figure 6.5 shows the development of ice-active surface sites n_s versus RH_i for all three experiments discussed above. In case of experiment ACI03_14 with uncoated AD (blue dashed line) no TDL measurement of water vapor pressure was available. Thus, the relative humidity calculated from the frost point temperature measured with the chilled–mirror hygrometer is shown. The onset point of ice formation ($RH_i \approx 110\,\%$) and the point at which an activated fraction of $0.1\,\%$ is exceeded ($RH_i \approx 138\,\%$) in experiment ACI03_14 are indicated. The total water (sum of droplets, ice crystals and water vapor) measured with the chilled–mirror hygrometer, MBW_i, and the gas–phase water measured with the TDL, RH_i, are in good agreement until the formation of ice crystals. In the immersion freezing experiment shown

in chapter 3.3, MBW_i starts to overestimate the relative humidity after an ice-active fraction of $0.1\,\%$ is exceeded. In contrast to the experiment shown in chapter 3.3, no droplet formation occurs in experiment ACI03_14, which started at a much colder temperature. The formation of droplets would deplete the gas–phase water concentration and therefore enhance the discrepancy between MBW_i and RH_i from the TDL measurement. For this reason, it can be assumed that MBW_i agrees well with RH_i even slightly after an ice-active fraction of $0.1\,\%$. However, it has not been systematically investigated at what ice-active fraction the MBW_i and RH_i start to deviate significantly.

Deposition ice nucleation was observed in the humidity range $RH_i \approx 110\,\%$ to $RH_i \approx 135\,\%$. In this range, the coated experiments ACI03_18 and ACI03_26 (blue and red solid line in Figure 6.5) exhibit lower values of n_s compared to experiment ACI03_14 with uncoated AD (blue dashed line), hence the SOA coating suppresses the ice nucleation in the deposition mode. At a relative humidity of $125\,\%$, n_s equals $0.8 \cdot 10^{10}\,\mathrm{m}^{-2}$ in the uncoated AD experiment, and $0.3 \cdot 10^{10}\,\mathrm{m}^{-2}$ in the coated AD experiment. Other than in the uncoated case (experiment ACI03_14, dashed line), experiments ACI03_18 and ACI03_26 both show a steep increase in n_s values within a small range of RH_i after $RH_i = 135\,\%$. For example, n_s increases from $10^{10}\,\mathrm{m}^{-2}$ at $135\,\%$ relative humidity, to almost $3.5 \cdot 10^{10}\,\mathrm{m}^{-2}$ at $140\,\%$ in experiment ACI03_18.

A quantitative comparison of n_s values between the experiment with coated AD and the experiment with coated SD can not be made. The dusts of different origin might have variable chemical compositions. Also, the size distributions differ significantly. For example, experiment ACI03_18 has a broader surface area size distribution compared to experiment ACI03_26 (cf. Figure 6.1). Even though the estimated average coating thickness is slightly higher for the experiment with SD (ACI03_26), the individual particle coating might differ, since it also depends on the particle size. As discussed before, in connection with the coating procedure in chapter 3.5, in the diffusion regime, the growth rate becomes inversely proportional to the particle radius, hence the coating thickness decreases with particle size.
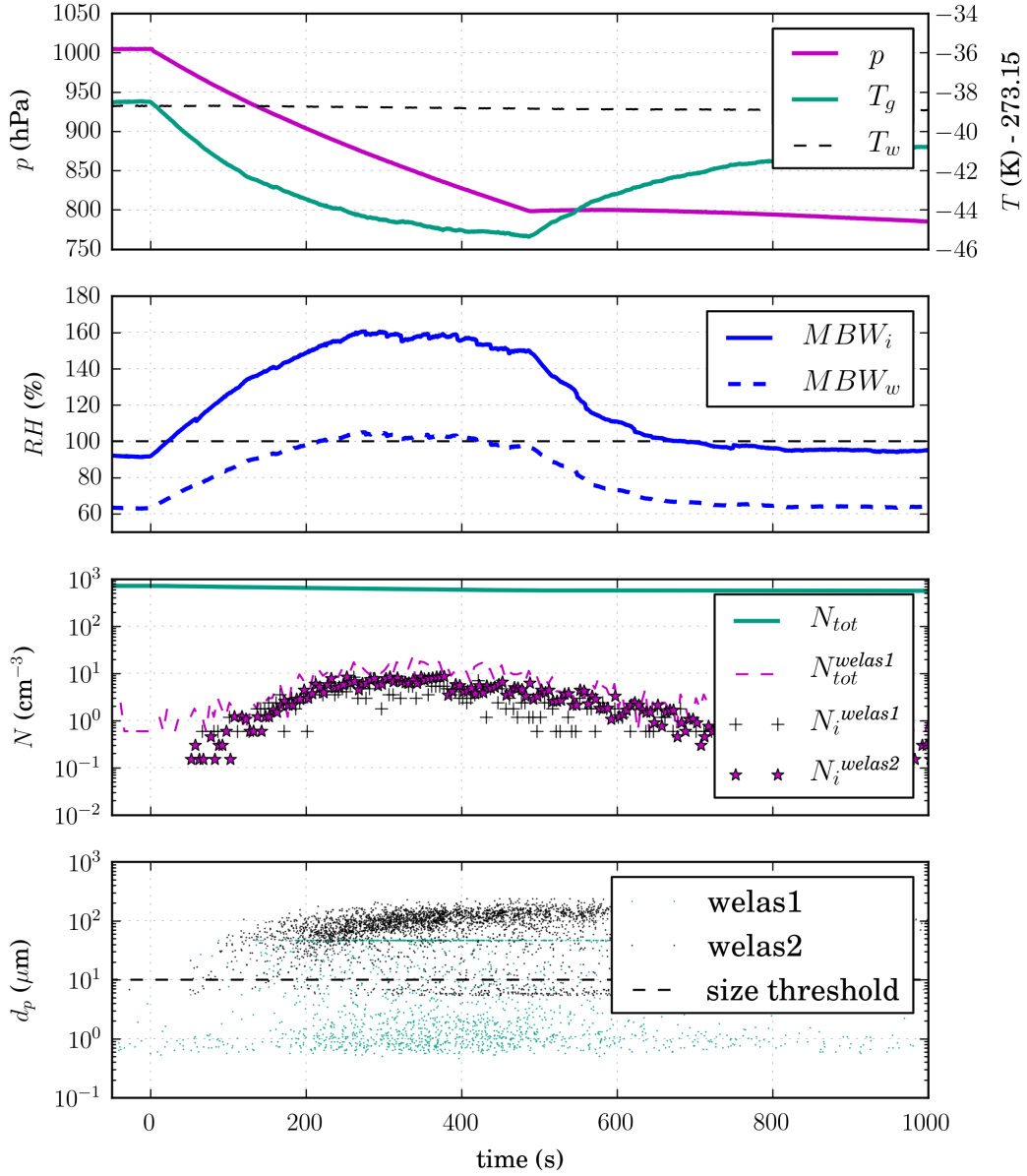
Figure 6.2.: AIDA time series of experiment ACI03_14 with AD. **Panel 1**: pressure p, wall temperature T_w, gas temperature T_g; **panel 2**: relative humidity with respect to water (RH_w) and ice (RH_i); **panel 3**: number concentration of total aerosol N_{tot} and ice crystals N_i^{welas1} and N_i^{welas2}; **panel 4**: particle size distribution with size threshold between droplets and ice crystals at $d_p = 10\,\mu m$.
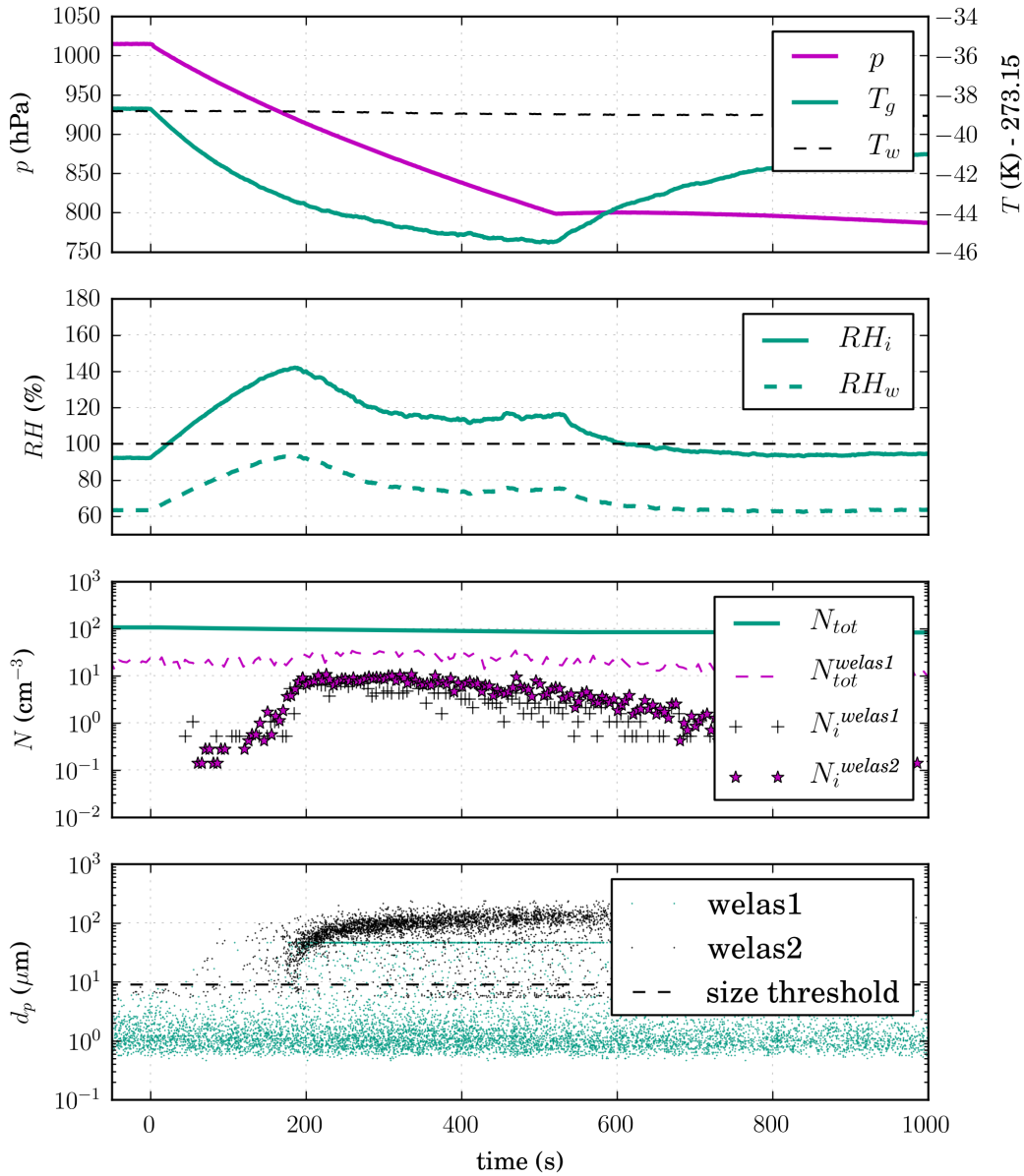
Figure 6.3.: AIDA time series of experiment ACI03_18 with SOA coated AD. **Panel 1**: pressure p, wall temperature T_w, gas temperature T_g; **panel 2**: relative humidity with respect to water (RH_w) and ice (RH_i); **panel 3**: number concentration of total aerosol N_{tot} and ice crystals N_i^{welas1} and N_i^{welas2}; **panel 4**: particle size distribution with size threshold between droplets and ice crystals at $d_p = 9\,\mu$m.
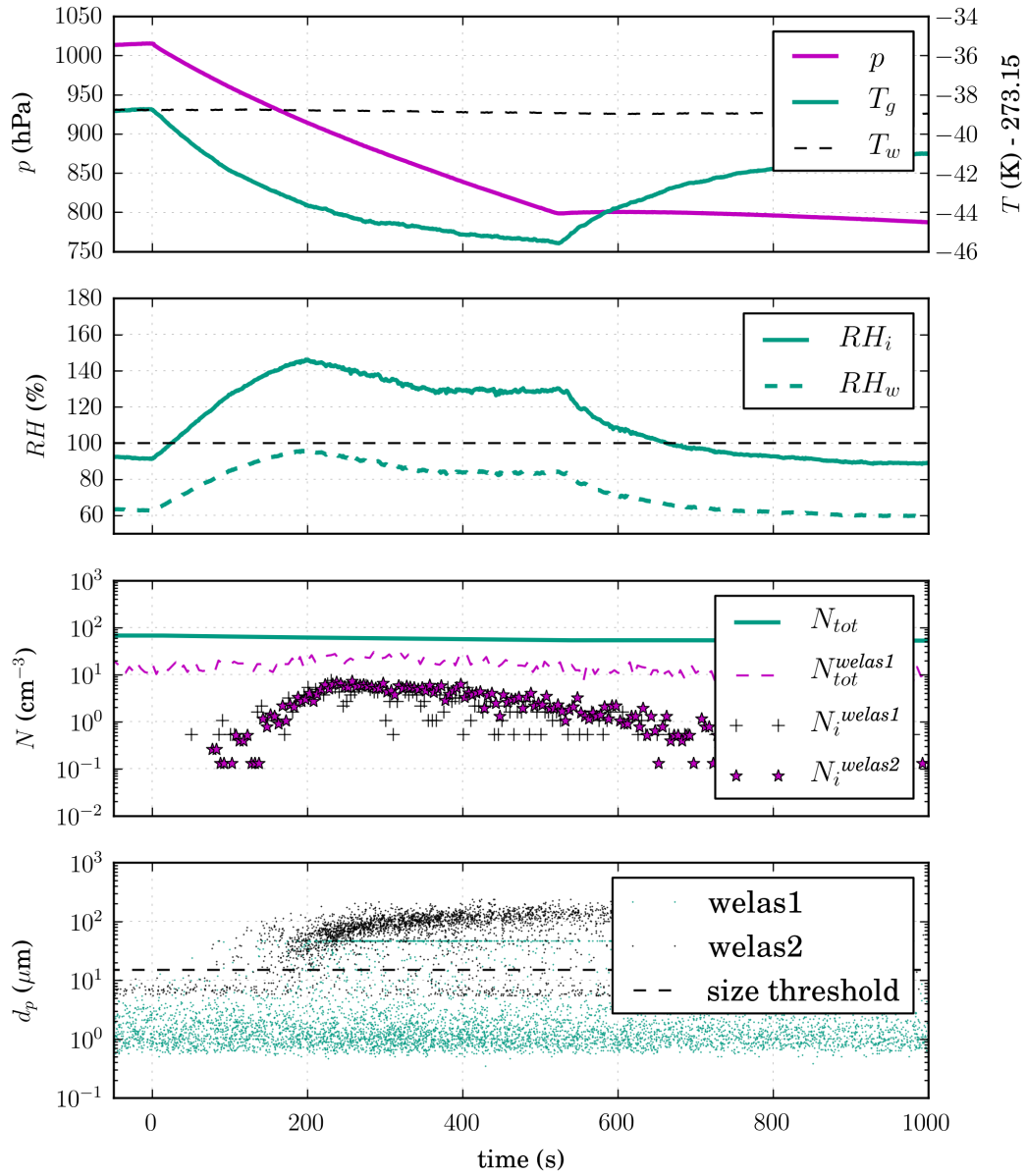
Figure 6.4.: AIDA time series of experiment ACI03_26 with SOA coated SD. **Panel 1**: pressure p, wall temperature T_w, gas temperature T_g; **panel 2**: relative humidity with respect to water (RH_w) and ice (RH_i); **panel 3**: number concentration of total aerosol N_{tot} and ice crystals N_i^{welas1} and N_i^{welas2}; **panel 4**: particle size distribution with size threshold between droplets and ice crystals at $d_p = 15\,\mu\mathrm{m}$.
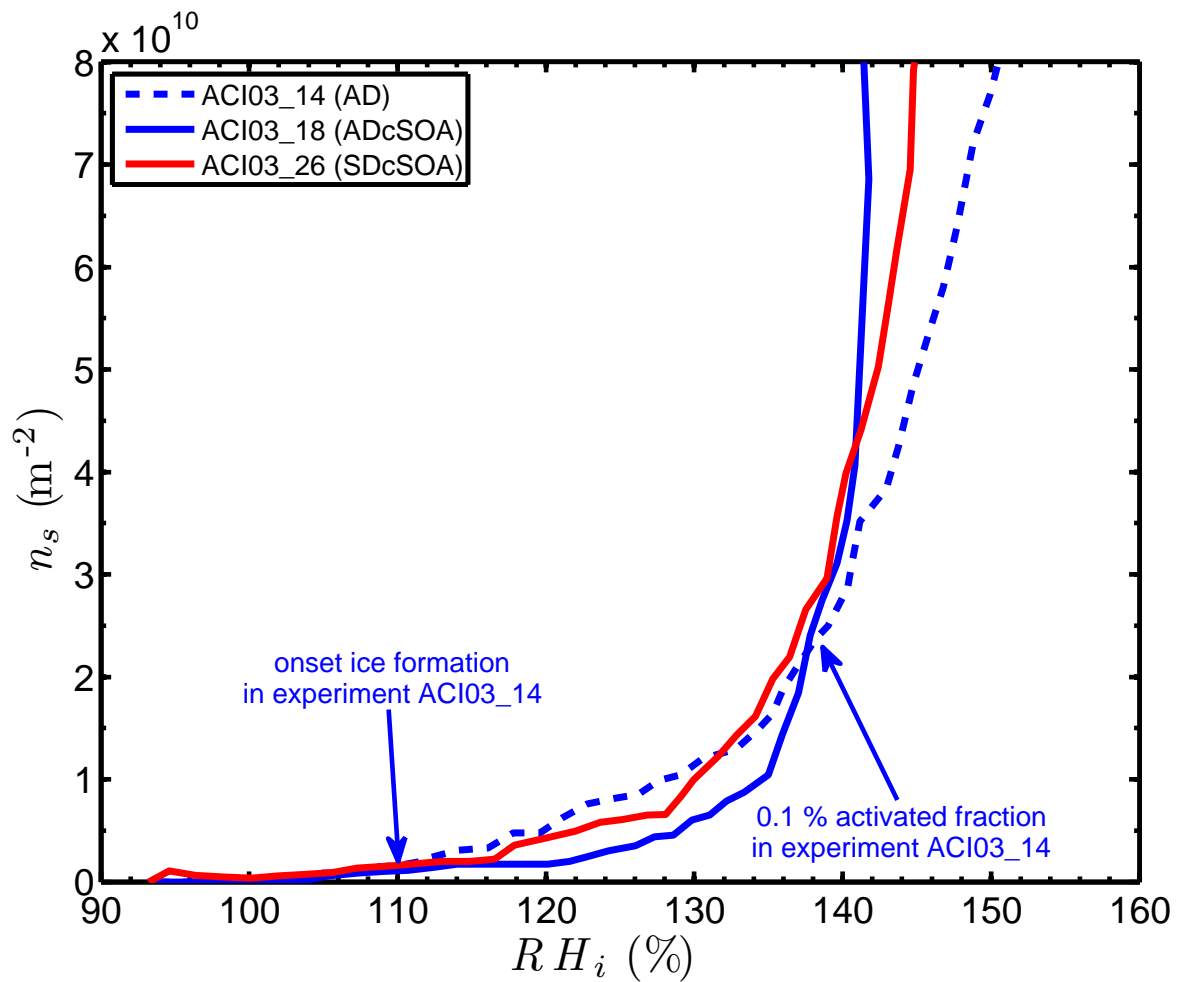
Figure 6.5.: Ice-active surface site density versus increasing relative humidity with respect to ice, RH_i. Comparison of an experiment with uncoated AD (dashed line) to experiments with SOA coated AD and SOA coated AD (solid lines).

6.3. Summary and conclusion

The ice nucleation efficiency of two desert dust samples, namely Asian dust (AD) and Saharan dust (SD), both coated with secondary organic aerosol (SOA), was investigated at the AIDA cloud simulation chamber in the temperature range –39 °C to –45 °C. The experiments were compared to an experiment with plain AD obtained during the same AIDA campaign. The pure AD sample nucleated ice through the deposition mode. The coated desert dust samples exhibited two distinct ice nucleation modes within one experiment. The first mode was likely due to deposition mode ice nucleation on uncoated or incompletely coated dust particles. The ice nucleation ability was suppressed by about a factor of two due to the organic coating compared to the uncoated case in the range 110 % to about 135 % relative humidity with respect to ice. The second mode appeared at relative humidities of about 138 % and 144 % for the AD and SD sample, respectively. In both cases, the second mode was observed close to water saturation where the water uptake was enhanced by the availability of water soluble organic products. The particles nucleated ice via immersion freezing. In the case of SOA coated AD, the number of ice-active surface sites showed a fivefold increase within 10 % relative humidity. In contrast, in the experiment with uncoated AD the number of ice-active surface sites only doubled within the same relative humidity range.

The same Asian and Saharan dust samples were previously investigated in the AIDA cloud chamber by Field et al. (2006). Below –40 °C, they observed ice formation via deposition nucleation for both desert dust samples, which is in good agreement with the experiments presented in this chapter. Möhler et al. (2008) investigated the deposition mode ice nucleation on uncoated and SOA coated Arizona test dust and illite (surrogates for mineral dust) at a starting temperature of –60 °C in the AIDA chamber. They observed a markedly suppression of the deposition mode ice nucleation by the SOA coating. The results from this study, although performed at higher temperatures, support their findings. A suppression of the ice nucleation efficiency due to the coating was observed in the deposition mode. Still some deposition mode ice nucleation occurred, presumably on uncoated or incompletely coated desert dust particles.

7. Summary & Outlook

The results of this thesis provide several suggestions for future scientific research. Some were already mentioned within the summary and conclusion section of each chapter. Referred to the introduction (chapter 1.2) four main objectives are listed below:

(1) **Investigation of the immersion freezing behavior of desert dust aerosols over a wide range of temperatures in the AIDA aerosol and cloud chamber.** The immersion freezing by desert dust particles, namely Asian dust, Saharan dust, Canary island dust, Israel dust and Arizona test dust (mineral dust surrogate) was investigated in the temperature range –10 °C to –28 °C.

It remains to be examined whether the surface soil samples used in this thesis are representative for long–range transported dust. Large differences in the freezing behavior were found among certain dust samples. Experiments with dust samples originating from other source regions could be investigated. Furthermore, the freezing behavior of desert dust samples should be investigated with other measurement techniques, e.g. continuous flow diffusion chamber (CFDC), and compared to the results of this thesis.

(2) **Deriving a new parameterization of immersion freezing on desert dust particles on the basis of AIDA laboratory experiments.** A new temperature and particle surface area dependent parameterization of immersion freezing on desert dust particles was derived from AIDA cloud chamber experiments. It is valid in the temperature range between –12 °C and –36 °C at or above water saturation.

It is planned to apply the ice-active surface site density approach to derive a parameterization of deposition ice nucleation as a function of ice supersaturation and temperature. More experiments, especially on desert dust particles are needed. Most deposition nucleation experiments were conducted on processed dust samples, such as Arizona test dust.

(3) **Application of the new parameterization.** An application of the new parameterization of immersion freezing was shown. It was used to calculate distribution maps of immersion freezing nuclei during a Saharan dust event based on model results from the regional scale online coupled model system COSMO-ART. This was then compared to measurements at the Taunus Observatory on Mount Kleiner Feldberg, and to other ice nucleation parameterizations, including the parameterizations by DeMott et al. (2010), Hoose et al. (2010) and Phillips et al. (2008), during a Saharan dust outbreak event in May 2008 (Klein et al., 2010). Furthermore, the new parameterization was compared to literature values of calculated ice-active surface site densities.

More simultaneous measurements of ice nuclei and aerosol number concentrations, also with different measurement devices, are needed to resolve the differences between the predicted and measured ice nuclei number concentrations. As mentioned earlier in this thesis, care has to be taken when comparing parameterizations derived from experiments with different dust samples. In order to resolve the differences among different parameterizations, more quantitative intercomparison studies between in situ IN measurements and model studies are needed.

(4) **Investigation of secondary organic aerosol coating on the ice nucleation efficiency of desert dust particles at mixed–phase and cirrus cloud temperatures.** The effect of secondary organic aerosol (SOA) coating on the ice nucleation ability of desert dust particles was investigated in the temperature range –22 °C to –29 °C and –39 °C to –45 °C, respectively.

In order to verify the results of the few experiments presented in this thesis, future studies should systematically investigate the effect of SOA coating on the ice nucleation ability of desert dusts over a wide range of temperatures. Furthermore, the coating thickness should be systematically varied. Also, it should be tested how different types of organic species affect the ice nucleation ability of desert dust particles.

A. Appendix

A.1. Diffusional growth rate of ice crystals in the presence of droplets

According to Pruppacher and Klett (1997), equation (13-10), the diffusional mass growth rate of a spherical ice crystal is described by

$$\frac{dm}{dt} = \frac{4\pi r D_v M_w}{R} \left(\frac{e_\infty}{T_\infty} - \frac{e_r}{T_r} \right), \tag{A.1}$$

where r is the ice crystal radius, M_w is the molecular weight of water, R is the universal gas constant, e_∞ and T_∞ are the water vapor pressure and temperature in great distance from the ice particle, respectively. e_r and T_r are the water vapor pressure and temperature at the ice particle surface. D_v describes the diffusivity of water vapor in air and is estimated by (Pruppacher and Klett, 1997, equation (13-3))

$$D_v = 0.211 \left(\frac{T_\infty}{T_0} \right)^{1.94} \left(\frac{p_0}{p} \right), \tag{A.2}$$

with $T_0 = 273.15\,\text{K}$ and $p_0 = 1013.25\,\text{hPa}$. p is the gas pressure. D_v is given in cm^2 s^{-1}. Equation A.1 is only applicable if the ice particles are much larger than the mean free path of water molecules in air, which is typically below 100 nm for AIDA experiments.

To calculate the size growth rate of an ice crystal, it is assumed that T_∞ and T_r are equal. Due to the latent heat release of condensation, T_r should be higher than T_∞ for $T_\infty > 230\,\text{K}$ and the actual ice particle growth rate should be lower than this estimate. With $dm = 4\pi \rho r^2 dr$, ρ being the mass density of ice, equation (A.1) becomes

$$\frac{dr}{dt} = \frac{D_v M_w}{\rho r R T_\infty} \left(e_\infty - e_r \right). \tag{A.3}$$

In the presence of liquid water droplets, thus water saturated conditions, e_∞ can be replaced by the saturation vapor pressure over water, $e_{w,sat}(T_\infty)$. e_r can be substituted by the saturation water vapor pressure over ice, $e_{i,sat}(T_\infty)$. $e_{w,sat}(T_\infty)$ and $e_{i,sat}(T_\infty)$ can be calculated using the equations by Murphy and Koop (2005), given in chapter 3.2. With $S_i = e_{w,sat}(T_\infty)/e_{i,sat}(T_\infty)$, one gets

$$\frac{dr}{dt} = \frac{D_v M_w e_{i,sat}(T_\infty)}{\rho r R T_\infty} \left(S_i - 1\right). \tag{A.4}$$

M_w is $18\,\text{g mol}^{-1}$ (Haynes, 2011). ρ equals the density of ice, and has a value of $0.9167\,\text{g cm}^{-3}$ (Pruppacher and Klett, 1997). R is $8.314\,\text{J mol}^{-1}\,\text{K}^{-1}$ (Haynes, 2011). Figure A.1 shows the estimated diffusional growth rate at a pressure $p = 1013.25\,\text{hPa}$ for ice particles of different radius, as a function of temperature.
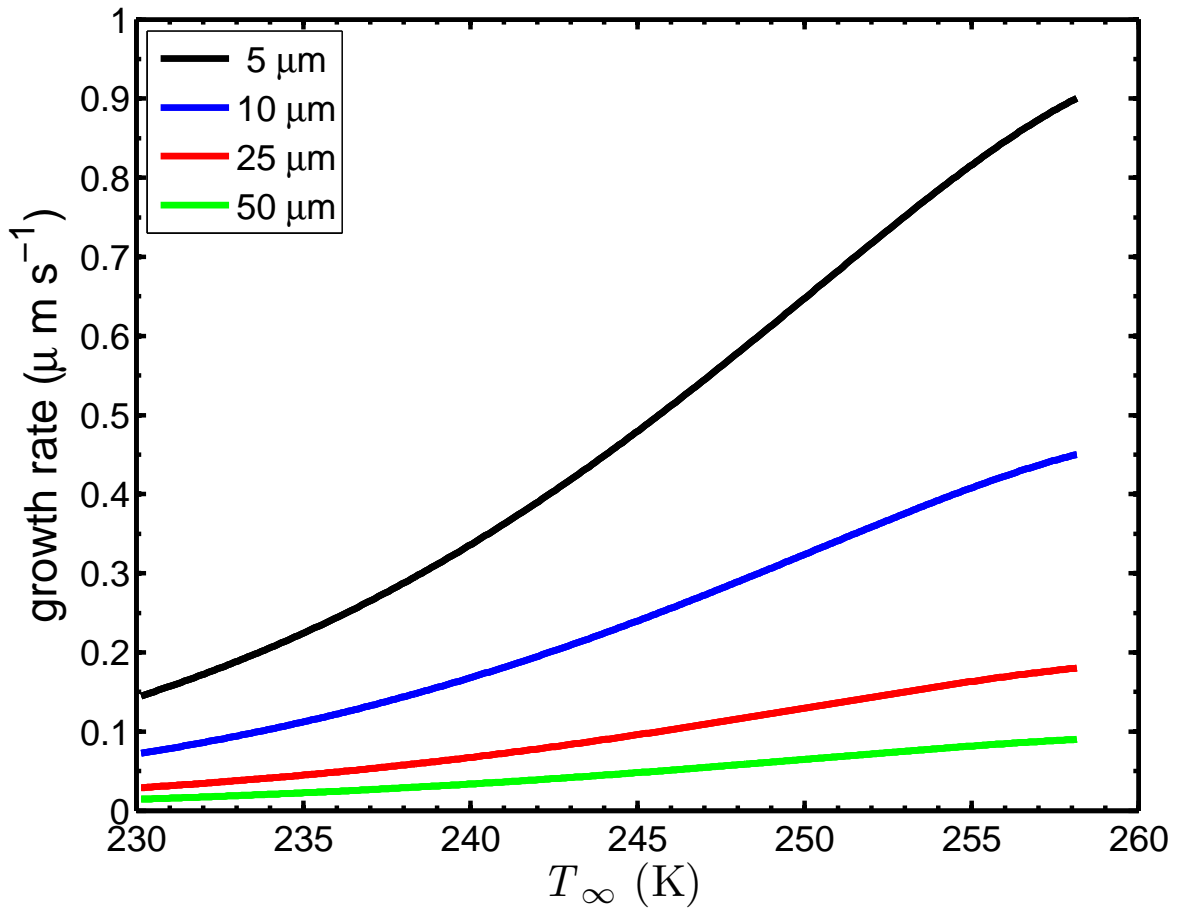

Figure A.1.: Estimated diffusional growth rate of ice particles of radii $5\,\mu\text{m}$, $10\,\mu\text{m}$, $25\,\mu\text{m}$ and $50\,\mu\text{m}$ in the presence of droplets as a function of temperature.

A.2. Table of symbols

Symbol	Unit	Description
d_a	(µm)	aerodynamic diameter
d_m	(µm)	mobility diameter
d_p	(µm)	volume–equivalent diameter
$d_{S,median}$	(µm)	median diameters
f_i		ice-active particle fraction
γ_{SOA}		calculated SOA yield
MBW_i	(%)	relative humidity with respect to ice calculated from the measured frost point temperature
MBW_w	(%)	relative humidity with respect to water calculated from the measured frost point temperature
N_0	(cm^{-3})	initial particle number concentration
N_{dust}	(cm^{-3})	number concentration of SOA coated particles
N_i	(cm^{-3})	number concentration of ice crystals
n_s	(m^{-2})	ice-active surface site density
N_{tot}	(cm^{-3})	total particle number concentration
N_{tot}^{welas1}	(cm^{-3})	total number concentration measured by welas1
N_i^{welas1}	(cm^{-3})	number concentration of ice crystals measured by welas1
N_i^{welas2}	(cm^{-3})	number concentration of ice crystals measured by welas2
N_d	(cm^{-3})	number concentration of droplets
p	(hPa)	pressure
p_0	(hPa)	initial pressure
RH_i	(%)	relative humidity with respect to ice
RH_w	(%)	relative humidity with respect to water
σ		geometric standard deviation
S_0	(µm^2 cm^{-3})	initial particle surface area
S_{ae}	(µm^2 cm^{-3})	individual particle surface area
S_{dust}	(µm^2 cm^{-3})	particle surface area of SOA coated particles
S_{tot}	(µm^2 cm^{-3})	total particle surface area concentration
T_0	(°C)	initial temperature
T_g	(°C)	gas temperature
T_{range}	(°C)	temperature range covered by the experiment
T_w	(°C)	wall temperature

Bibliography

Ansmann, A., et al., 2008: Influence of Saharan dust on cloud glaciation in southern Morocco during the Saharan Mineral Dust Experiment. *J. Geophys. Res.*, **113 (D4)**, doi:10.1029/2007JD008785, URL `http://www.agu.org/pubs/crossref/2008/2007JD008785.shtml`.

Archuleta, C. M., P. J. DeMott, and S. M. Kreidenweis, 2005: Ice nucleation by surrogates for atmospheric mineral dust and mineral dust/sulfate particles at cirrus temperatures. *Atmos. Chem. Phys.*, **5 (10)**, 2617–2634, doi:10.5194/acp-5-2617-2005, URL `http://www.atmos-chem-phys.net/5/2617/2005/`.

Bangert, M., C. Kottmeier, B. Vogel, and H. Vogel, 2011a: Regional scale effects of the aerosol cloud interaction simulated with an online coupled comprehensive chemistry model. *Atmos. Chem. Phys.*, **11 (9)**, 4411–4423, doi:10.5194/acp-11-4411-2011, URL `http://www.atmos-chem-phys.net/11/4411/2011/`.

Bangert, M., et al., 2011b: Saharan dust event impacts on cloud formation and radiation over Western Europe. *Atmos. Chem. Phys. Discuss.*, **11 (12)**, 31 937–31 982, doi:10.5194/acpd-11-31937-2011, URL `http://www.atmos-chem-phys-discuss.net/11/31937/2011/`.

Barahona, D., 2011: On the ice nucleation spectrum. *Atmos. Chem. Phys. Discuss.*, **11 (11)**, 29 601–29 646, doi:10.5194/acpd-11-29601-2011, URL `http://www.atmos-chem-phys-discuss.net/11/29601/2011/`.

Benz, S., 2006: Experimente zur Eisnukleation von Wassertröpfchen und Sulfatpartikeln bei Temperaturen zwischen –65 °C und –30 °C. Ph.D. thesis, Fakultät für Physik der Universität Karlsruhe (TH).

Benz, S., K. Megahed, O. Möhler, H. Saathoff, R. Wagner, and U. Schurath, 2005: T-dependent rate measurements of homogeneous ice nucleation in cloud

droplets using a large atmospheric simulation chamber. *J. Photochem. Photobio. A. Chem.*, **176 (1-3)**, 208–217, doi:10.1016/j.jphotochem.2005.08.026, URL `http://linkinghub.elsevier.com/retrieve/pii/S1010603005004181`.

Broadley, S. L., B. J. Murray, R. J. Herbert, J. D. Atkinson, S. Dobbie, T. L. Malkin, E. Condliffe, and L. Neve, 2012: Immersion mode heterogeneous ice nucleation by an illite rich powder representative of atmospheric mineral dust. *Atmos. Chem. Phys.*, **12 (1)**, 287–307, doi:10.5194/acp-12-287-2012, URL `http://www.atmos-chem-phys.net/12/287/2012/`.

Brunauer, S., P. H. Emmett, and E. Teller, 1938: Adsorption of gases in multimolecular layers. *J. Am. Chem. Soc.*, **60**, 309—-319.

Bundke, U., B. Nillius, R. Jaenicke, T. Wetter, H. Klein, and H. Bingemer, 2008: The fast Ice Nucleus chamber FINCH. *Atmos. Res.*, **90 (2-4)**, 180–186, doi:10.1016/j.atmosres.2008.02.008, URL `http://linkinghub.elsevier.com/retrieve/pii/S0169809508000318`.

Callot, Y., B. Marticorena, and G. Bergametti, 2000: Geomorphologic approach for modelling the surface features of arid environments in a model of dust emissions: application to the Sahara desert. *Geodinamica Acta*, **13 (5)**, 245–270, doi:10.1016/S0985-3111(00)01044-5, URL `http://linkinghub.elsevier.com/retrieve/pii/S0985311100010445`.

Chen, J., A. Hazra, and Z. Levin, 2008: Parameterizing ice nucleation rates using contact angle and activation energy derived from laboratory data. *Atmos. Chem. Phys.*, **8 (24)**, 7431–7449, doi:10.5194/acp-8-7431-2008, URL `http://www.atmos-chem-phys.net/8/7431/2008/`.

Chou, C., O. Stetzer, E. Weingartner, Z. Jurányi, Z. A. Kanji, and U. Lohmann, 2011: Ice nuclei properties within a Saharan dust event at the Jungfraujoch in the Swiss Alps. *Atmos. Chem. Phys.*, **11 (10)**, 4725–4738, doi:10.5194/acp-11-4725-2011, URL `http://www.atmos-chem-phys.net/11/4725/2011/`.

Conen, F., C. E. Morris, J. Leifeld, M. V. Yakutin, and C. Alewell, 2011: Biological residues define the ice nucleation properties of soil dust. *Atmos. Chem. Phys.*, **11 (18)**, 9643–9648, doi:10.5194/acp-11-9643-2011, URL `http://www.atmos-chem-phys.net/11/9643/2011/`.

Connolly, P. J., O. Möhler, P. R. Field, H. Saathoff, R. Burgess, T. Choularton, and M. Gallagher, 2009: Studies of heterogeneous freezing by three different desert dust samples. *Atmos. Chem. Phys.*, **9 (8)**, 2805–2824, doi:10.5194/acp-9-2805-2009, URL `http://www.atmos-chem-phys.net/9/2805/2009/`.

Cziczo, D. J., K. D. Froyd, S. J. Gallavardin, O. Moehler, S. Benz, H. Saathoff, and D. M. Murphy, 2009: Deactivation of ice nuclei due to atmospherically relevant surface coatings. *Environ. Res. Lett.*, **4 (4)**, 044 013, doi:10.1088/1748-9326/4/4/044013, URL `http://stacks.iop.org/1748-9326/4/i=4/a=044013?key=crossref.f0b33c2dbaef8b0dc49fb4ee48d5bf82`.

Davies, C., 1979: Particle-fluid interaction. *J. Aerosol Sci.*, **10 (5)**, 477–513, doi:10.1016/0021-8502(79)90006-5, URL `http://linkinghub.elsevier.com/retrieve/pii/0021850279900065`.

DeMott, P., 1995: Quantitative descriptions of ice formation mechanisms of silver iodide-type aerosols. *Atmos. Res.*, **38 (1-4)**, 63–99, doi:10.1016/0169-8095(94)00088-U, URL `http://linkinghub.elsevier.com/retrieve/pii/016980959400088U`.

DeMott, P. J., K. Sassen, M. R. Poellot, D. Baumgardner, D. C. Rogers, S. D. Brooks, A. J. Prenni, and S. M. Kreidenweis, 2003: African dust aerosols as atmospheric ice nuclei. *Geophys. Res. Lett.*, **30 (14)**, doi:10.1029/2003GL017410, URL `http://www.agu.org/pubs/crossref/2003/2003GL017410.shtml`.

DeMott, P. J., et al., 2010: Predicting global atmospheric ice nuclei distributions and their impacts on climate. *Proc. Natl. Acad. Sci. (USA)*, **107 (25)**, 11 217–11 222, doi:10.1073/pnas.0910818107, URL `http://www.pnas.org/cgi/doi/10.1073/pnas.0910818107`.

DeMott, P. J., et al., 2011: Resurgence in ice nuclei measurement research. *Bull. Amer. Meteor. Soc.*, **92 (12)**, 1623–1635, doi:10.1175/2011BAMS3119.1, URL `http://journals.ametsoc.org/doi/abs/10.1175/2011BAMS3119.1`.

Denman, K. L., et al., 2007: Couplings between changes in the climate system and biogeochemistry. *Climate Change 2007: The Physical Science Basis. Contribution of Working Group I to the Fourth Assessment Report of the Intergovernmental Panel on Climate Change*, S. Solomon, D. Qin, M. Manning, Z. Chen, M. Marquis, K. B.

Averyt, M. Tignor, and H. L. Miller, Eds., Cambridge University Press, Cambridge, United Kingdom and New York, NY, USA.

Després, V. R., et al., 2012: Primary biological aerosol particles in the atmosphere: a review. *Tellus B*, **64 (0)**, doi:10.3402/tellusb.v64i0.15598, URL `http://www.tellusb.net/index.php/tellusb/article/view/15598`.

Eastwood, M. L., S. Cremel, M. Wheeler, B. J. Murray, E. Girard, and A. K. Bertram, 2009: Effects of sulfuric acid and ammonium sulfate coatings on the ice nucleation properties of kaolinite particles. *Geophys. Res. Lett.*, **36 (2)**, doi:10.1029/2008GL035997, URL `http://www.agu.org/pubs/crossref/2009/2008GL035997.shtml`.

Ebert, V., H. Teichert, C. Giesemann, H. Saathoff, and U. Schurath, 2005: Fasergekoppeltes In-situ-Laserspektrometer für den selektiven Nachweis von Wasserdampfspuren bis in den ppb-Bereich. *Tech. Mess.*, **72**, 23–30.

Fahey, D. W., R. S. Gao, and O. Möhler, 2009: Summary of the AquaVIT Water Vapor Intercomparison: Static Experiments. *AquaVIT White Paper*, URL `https://aquavit.icg.kfa-juelich.de/AquaVit/AquaVitWiki`.

Falkovich, A. H., 2004: Adsorption of organic compounds pertinent to urban environments onto mineral dust particles. *J. Geophys. Res.*, **109 (D2)**, doi:10.1029/2003JD003919, URL `http://www.agu.org/pubs/crossref/2004/2003JD003919.shtml`.

Field, P. R., O. Möhler, P. Connolly, M. Krämer, R. Cotton, A. J. Heymsfield, H. Saathoff, and M. Schnaiter, 2006: Some ice nucleation characteristics of Asian and Saharan desert dust. *Atmos. Chem. Phys.*, **6 (10)**, 2991–3006, doi:10.5194/acp-6-2991-2006, URL `http://www.atmos-chem-phys.net/6/2991/2006/`.

Fletcher, N. H., 1958: Size effect in heterogeneous nucleation. *J. Chem. Phys.*, **29**, 572–576.

Fletcher, N. H., 1962: *The physics of rainclouds.* Cambridge University Press, 286 pp.

Fornea, A. P., S. D. Brooks, J. B. Dooley, and A. Saha, 2009: Heterogeneous freezing of ice on atmospheric aerosols containing ash, soot, and soil. *J. Geophys. Res.*, **114 (D13)**, doi:10.1029/2009JD011958, URL `http://www.agu.org/pubs/crossref/2009/2009JD011958.shtml`.

Forster, P., et al., 2007: Changes in atmospheric constituents and in radiative forcing. *Climate Change 2007: The Physical Science Basis. Contribution of Working Group I to the Fourth Assessment Report of the Intergovernmental Panel on Climate Change*, S. Solomon, D. Qin, M. Manning, Z. Chen, M. Marquis, K. B. Averyt, M. Tignor, and H. L. Miller, Eds., Cambridge University Press, Cambridge, United Kingdom and New York, NY, USA.

Goudie, A. and N. Middleton, 2001: Saharan dust storms: nature and consequences. *Earth-Science Reviews*, **56 (1-4)**, 179–204, doi:10.1016/S0012-8252(01)00067-8, URL http://linkinghub.elsevier.com/retrieve/pii/S0012825201000678.

Hallett, J. and S. C. Mossop, 1974: Production of secondary ice particles during the riming process. **249 (5452)**, 26–28, doi:10.1038/249026a0, URL http://www.nature.com/doifinder/10.1038/249026a0.

Hallquist, M., et al., 2009: The formation, properties and impact of secondary organic aerosol: current and emerging issues. *Atmos. Chem. Phys.*, **9 (14)**, 5155–5236, doi:10.5194/acp-9-5155-2009, URL http://www.atmos-chem-phys.net/9/5155/2009/.

Haynes, W. M., 2011: *CRC handbook of chemistry and physics.* CRC ; Taylor & Francis [distributor], Boca Raton, Fla.; London.

Heintzenberg, J., K. Okada, and J. Ström, 1996: On the composition of non-volatile material in upper tropospheric aerosols and cirrus crystals. *Atmos. Res.*, **41 (1)**, 81–88, doi:10.1016/0169-8095(95)00042-9, URL http://linkinghub.elsevier.com/retrieve/pii/0169809595000429.

Hinds, W., 1999: *Aerosol technology : properties, behavior, and measurement of airborne particles.* 2d ed., Wiley, New York.

Hoose, C., J. E. Kristjánsson, J. Chen, and A. Hazra, 2010: A Classical-Theory-Based parameterization of heterogeneous ice nucleation by mineral dust, soot, and biological particles in a global climate model. *J. Atmos. Sci.*, **67 (8)**, 2483–2503, doi:10.1175/2010JAS3425.1, URL http://journals.ametsoc.org/doi/abs/10.1175/2010JAS3425.1.

Hoose, C., U. Lohmann, R. Erdin, and I. Tegen, 2008: The global influence of dust mineralogical composition on heterogeneous ice nucleation in

mixed-phase clouds. *Environ. Res. Lett.*, **3 (2)**, 025 003, doi:10.1088/1748-9326/3/2/025003, URL `http://stacks.iop.org/1748-9326/3/i=2/a=025003?key=crossref.6947b2a0b61aa2ae89a946b6ec3f91b1`.

Hung, H., A. Malinowski, and S. T. Martin, 2003: Kinetics of heterogeneous ice nucleation on the surfaces of mineral dust cores inserted into aqueous ammonium sulfate particles. *J. Phys. Chem. A*, **107 (9)**, 1296–1306, doi:10.1021/jp021593y, URL `http://pubs.acs.org/doi/abs/10.1021/jp021593y`.

Jimenez, J. L., et al., 2009: Evolution of organic aerosols in the atmosphere. *Science*, **326 (5959)**, 1525–1529, doi:10.1126/science.1180353, URL `http://www.sciencemag.org/cgi/doi/10.1126/science.1180353`.

John, W., 2011: Size distribution characteristics of aerosols. *Aerosol Measurement*, P. Kulkarni, P. A. Baron, and K. Willeke, Eds., John Wiley & Sons, Inc., Hoboken, NJ, USA, 41–54, URL `http://doi.wiley.com/10.1002/9781118001684.ch4`.

Jones, H. M., M. J. Flynn, P. J. DeMott, and O. Möhler, 2011: Manchester Ice Nucleus Counter (MINC) measurements from the 2007 International workshop on Comparing Ice nucleation Measuring Systems (ICIS-2007). *Atmos. Chem. Phys.*, **11 (1)**, 53–65, doi:10.5194/acp-11-53-2011, URL `http://www.atmos-chem-phys.net/11/53/2011/`.

Kandler, K., et al., 2007: Chemical composition and complex refractive index of Saharan mineral dust at Izaña, Tenerife (Spain) derived by electron microscopy. *Atmos. Environ.*, **41 (37)**, 8058–8074, doi:10.1016/j.atmosenv.2007.06.047, URL `http://linkinghub.elsevier.com/retrieve/pii/S1352231007006061`.

Kandler, K., et al., 2009: Size distribution, mass concentration, chemical and mineralogical composition and derived optical parameters of the boundary layer aerosol at Tinfou, Morocco, during SAMUM 2006. *Tellus B*, **61 (1)**, 32–50, doi:10.1111/j.1600-0889.2008.00385.x, URL `http://doi.wiley.com/10.1111/j.1600-0889.2008.00385.x`.

Kanji, Z. A. and J. P. D. Abbatt, 2010: Ice nucleation onto Arizona Test Dust at cirrus temperatures: Effect of temperature and aerosol size on onset relative humidity. *J. Phys. Chem. A*, **114 (2)**, 935–941, doi:10.1021/jp908661m, URL `http://pubs.acs.org/doi/abs/10.1021/jp908661m`.

Kanji, Z. A., P. J. DeMott, O. Möhler, and J. P. D. Abbatt, 2011: Results from the university of toronto continuous flow diffusion chamber at ICIS 2007: instrument intercomparison and ice onsets for different aerosol types. *Atmos. Chem. Phys.*, **11 (1)**, 31–41, doi:10.5194/acp-11-31-2011, URL `http://www.atmos-chem-phys.net/11/31/2011/`.

Kanji, Z. A., O. Florea, and J. P. D. Abbatt, 2008: Ice formation via deposition nucleation on mineral dust and organics: dependence of onset relative humidity on total particulate surface area. *Environ. Res. Lett.*, **3 (2)**, 025 004, doi:10.1088/1748-9326/3/2/025004, URL `http://stacks.iop.org/1748-9326/3/i=2/a=025004?key=crossref.0411a868f7543ea0bb122b2fdafa23ce`.

Karydis, V. A., P. Kumar, D. Barahona, I. N. Sokolik, and A. Nenes, 2011: On the effect of dust particles on global cloud condensation nuclei and cloud droplet number. *J. Geophys. Res.*, **116 (D23)**, doi:10.1029/2011JD016283, URL `http://www.agu.org/pubs/crossref/2011/2011JD016283.shtml`.

Klein, H., et al., 2010: Saharan dust and ice nuclei over Central Europe. *Atmos. Chem. Phys.*, **10 (21)**, 10 211–10 221, doi:10.5194/acp-10-10211-2010, URL `http://www.atmos-chem-phys.net/10/10211/2010/`.

Knopf, D. A. and T. Koop, 2006: Heterogeneous nucleation of ice on surrogates of mineral dust. *J. Geophys. Res.*, **111 (D12)**, doi:10.1029/2005JD006894, URL `http://www.agu.org/pubs/crossref/2006/2005JD006894.shtml`.

Knote, C., et al., 2011: Towards an online-coupled chemistry-climate model: evaluation of trace gases and aerosols in COSMO-ART. *Geosci. Model Dev.*, **4 (4)**, 1077–1102, doi:10.5194/gmd-4-1077-2011, URL `http://www.geosci-model-dev.net/4/1077/2011/`.

Koehler, K. A., S. M. Kreidenweis, P. J. DeMott, M. D. Petters, A. J. Prenni, and O. Möhler, 2010: Laboratory investigations of the impact of mineral dust aerosol on cold cloud formation. *Atmos. Chem. Phys.*, **10 (23)**, 11 955–11 968, doi:10.5194/acp-10-11955-2010, URL `http://www.atmos-chem-phys.net/10/11955/2010/`.

Koop, T., J. Bookhold, M. Shiraiwa, and U. Pöschl, 2011: Glass transition and phase state of organic compounds: dependency on molecular properties and implications for secondary organic aerosols in the atmosphere. *Phys. Chem. Chem.*

Phys., **13 (43)**, 19 238, doi:10.1039/c1cp22617g, URL http://xlink.rsc.org/?DOI=c1cp22617g.

Kulkarni, P., P. A. Baron, C. M. Sorensen, and M. Harper, 2011: Nonspherical particle measurement: Shape factor, fractals, and fibers. *Aerosol Measurement*, P. Kulkarni, P. A. Baron, and K. Willeke, Eds., John Wiley & Sons, Inc., Hoboken, NJ, USA, 507–547, URL http://doi.wiley.com/10.1002/9781118001684.ch23.

Lamb, D. and J. Verlinde, 2011: *Physics and chemistry of clouds.* Cambridge University Press, Cambridge; New York.

Levin, Z., E. Ganor, and V. Gladstein, 1996: The effects of desert particles coated with sulfate on rain formation in the Eastern Mediterranean. *J. Appl. Meteor.*, **35 (9)**, 1511–1523, doi:10.1175/1520-0450(1996)035<1511:TEODPC>2.0.CO;2, URL http://journals.ametsoc.org/doi/abs/10.1175/1520-0450%281996%29035%3C1511%3ATEODPC%3E2.0.CO%3B2.

Linke, C., O. Möhler, A. 'Veres, A. Mohácsi, Z. Bozóki, G. Szabó, and M. Schnaiter, 2006: Optical properties and mineralogical composition of different Saharan mineral dust samples: a laboratory study. *Atmos. Chem. Phys.*, **6 (11)**, 3315–3323, doi:10.5194/acp-6-3315-2006, URL http://www.atmos-chem-phys.net/6/3315/2006/.

Lohmann, U. and K. Diehl, 2006: Sensitivity studies of the importance of dust ice nuclei for the indirect aerosol effect on stratiform Mixed-Phase clouds. *J. Atmos. Sci.*, **63 (3)**, 968–982, doi:10.1175/JAS3662.1, URL http://journals.ametsoc.org/doi/abs/10.1175/JAS3662.1.

Lüönd, F., O. Stetzer, A. Welti, and U. Lohmann, 2010: Experimental study on the ice nucleation ability of size-selected kaolinite particles in the immersion mode. *J. Geophys. Res.*, **115 (D14)**, doi:10.1029/2009JD012959, URL http://www.agu.org/pubs/crossref/2010/2009JD012959.shtml.

Marcolli, C., S. Gedamke, T. Peter, and B. Zobrist, 2007: Efficiency of immersion mode ice nucleation on surrogates of mineral dust. *Atmos. Chem. Phys.*, **7 (19)**, 5081–5091, doi:10.5194/acp-7-5081-2007, URL http://www.atmos-chem-phys.net/7/5081/2007/.

Marticorena, B., G. Bergametti, B. Aumont, Y. Callot, C. N'Doumé, and M. Legrand, 1997: Modeling the atmospheric dust cycle 2. Simulation of Saharan dust sources.

J. Geophys. Res., **102 (D4)**, 4387–4404, doi:10.1029/96JD02964, URL `http://www.agu.org/pubs/crossref/1997/96JD02964.shtml`.

Meyers, M. P., P. J. DeMott, and W. R. Cotton, 1992: New primary Ice-Nucleation parameterizations in an explicit cloud model. *J. Appl. Meteor.*, **31 (7)**, 708–721, doi:10.1175/1520-0450(1992)031<0708:NPINPI>2.0.CO; 2, URL `http://journals.ametsoc.org/doi/abs/10.1175/1520-0450%281992%29031%3C0708%3ANPINPI%3E2.0.CO%3B2`.

Möhler, O., et al., 2003: Experimental investigation of homogeneous freezing of sulphuric acid particles in the aerosol chamber AIDA. *Atmos. Chem. Phys.*, **3 (1)**, 211–223, doi:10.5194/acp-3-211-2003, URL `http://www.atmos-chem-phys.net/3/211/2003/`.

Möhler, O., et al., 2006: Efficiency of the deposition mode ice nucleation on mineral dust particles. *Atmos. Chem. Phys.*, **6 (10)**, 3007–3021, doi:10.5194/acp-6-3007-2006, URL `http://www.atmos-chem-phys.net/6/3007/2006/`.

Möhler, O., et al., 2008: The effect of organic coating on the heterogeneous ice nucleation efficiency of mineral dust aerosols. *Environ. Res. Lett.*, **3 (2)**, 025 007, doi:10.1088/1748-9326/3/2/025007, URL `http://stacks.iop.org/1748-9326/3/i=2/a=025007?key=crossref.d9430010506fa5292539821f7ee92ca3`.

Murphy, D. M. and T. Koop, 2005: Review of the vapour pressures of ice and supercooled water for atmospheric applications. *Quart. J. Roy. Meteor. Soc.*, **131 (608)**, 1539–1565, doi:10.1256/qj.04.94, URL `http://doi.wiley.com/10.1256/qj.04.94`.

Murray, B. J., S. L. Broadley, T. W. Wilson, J. D. Atkinson, and R. H. Wills, 2011: Heterogeneous freezing of water droplets containing kaolinite particles. *Atmos. Chem. Phys.*, **11 (9)**, 4191–4207, doi:10.5194/acp-11-4191-2011, URL `http://www.atmos-chem-phys.net/11/4191/2011/`.

Murray, B. J., et al., 2010: Heterogeneous nucleation of ice particles on glassy aerosols under cirrus conditions. *Nature Geosci.*, **3 (4)**, 233–237, doi:10.1038/ngeo817, URL `http://www.nature.com/doifinder/10.1038/ngeo817`.

Nickovic, S., G. Kallos, A. Papadopoulos, and O. Kakaliagou, 2001: A model for prediction of desert dust cycle in the atmosphere. *J. Geophys. Res.*, **106 (D16)**, 18 113–

18 129, doi:10.1029/2000JD900794, URL `http://www.agu.org/pubs/crossref/2001/2000JD900794.shtml`.

Nicolet, M., O. Stetzer, F. Lüönd, O. Möhler, and U. Lohmann, 2010: Single ice crystal measurements during nucleation experiments with the depolarization detector IODE. *Atmos. Chem. Phys.*, **10 (2)**, 313–325, doi:10.5194/acp-10-313-2010, URL `http://www.atmos-chem-phys.net/10/313/2010/`.

Niedermeier, D., et al., 2010: Heterogeneous freezing of droplets with immersed mineral dust particles – measurements and parameterization. *Atmos. Chem. Phys.*, **10 (8)**, 3601–3614, doi:10.5194/acp-10-3601-2010, URL `http://www.atmos-chem-phys.net/10/3601/2010/`.

Niemand, M., et al., 2012: A particle-surface-area-based parameterization of immersion freezing on desert dust particles. *J. Atmos. Sci.*, doi:10.1175/JAS-D-11-0249.1, URL `http://journals.ametsoc.org/doi/abs/10.1175/JAS-D-11-0249.1`.

Palas, 2008: Practical basic knowledge regarding aerosol technology. Palas® GmbH, Karlsruhe, URL `www.palas.de`.

Phillips, V. T. J., P. J. DeMott, and C. Andronache, 2008: An empirical parameterization of heterogeneous ice nucleation for multiple chemical species of aerosol. *J. Atmos. Sci.*, **65 (9)**, 2757–2783, doi:10.1175/2007JAS2546.1, URL `http://journals.ametsoc.org/doi/abs/10.1175/2007JAS2546.1`.

Prenni, A. J., M. D. Petters, A. Faulhaber, C. M. Carrico, P. J. Ziemann, S. M. Kreidenweis, and P. J. DeMott, 2009: Heterogeneous ice nucleation measurements of secondary organic aerosol generated from ozonolysis of alkenes. *Geophys. Res. Lett.*, **36 (6)**, doi:10.1029/2008GL036957, URL `http://www.agu.org/pubs/crossref/2009/2008GL036957.shtml`.

Prenni, A. J., et al., 2007: Examinations of ice formation processes in florida cumuli using ice nuclei measurements of anvil ice crystal particle residues. *J. Geophys. Res.*, **112 (D10)**, doi:10.1029/2006JD007549, URL `http://www.agu.org/pubs/crossref/2007/2006JD007549.shtml`.

Prospero, J. M., P. Ginoux, O. Torres, S. E. Nicholson, and T. E. Gill, 2002: Environmental characterization of global sources of atmospheric soil dust identified with the NIMBUS 7 Total Ozone Mapping Spectrometer (TOMS) absorb-

ing aerosol product. *Rev. Geophys.*, **40 (1)**, doi:10.1029/2000RG000095, URL `http://www.agu.org/pubs/crossref/2002/2000RG000095.shtml`.

Pruppacher, H. R. and J. D. Klett, 1997: *Microphysics of clouds and precipitation.* 2d ed., Kluwer Academic Publishers.

Saathoff, H., et al., 2009: Temperature dependence of yields of secondary organic aerosols from the ozonolysis of α-pinene and limonene. *Atmos. Chem. Phys.*, **9 (5)**, 1551–1577, doi:10.5194/acp-9-1551-2009, URL `http://www.atmos-chem-phys.net/9/1551/2009/`.

Sassen, K., P. J. DeMott, J. M. Prospero, and M. R. Poellot, 2003: Saharan dust storms and indirect aerosol effects on clouds: CRYSTAL-FACE results. *Geophys. Res. Lett.*, **30 (12)**, doi:10.1029/2003GL017371, URL `http://www.agu.org/pubs/crossref/2003/2003GL017371.shtml`.

Schütz, L. and M. Sebert, 1987: Mineral aerosols and source identification. *J. Aerosol Sci.*, **18 (1)**, 1–10, doi:10.1016/0021-8502(87)90002-4, URL `http://linkinghub.elsevier.com/retrieve/pii/0021850287900024`.

Seifert, M., R. Tiede, M. Schnaiter, C. Linke, O. Möhler, U. Schurath, and J. Ström, 2004: Operation and performance of a differential mobility particle sizer and a TSI 3010 condensation particle counter at stratospheric temperatures and pressures. *J. Aerosol Sci.*, **35 (8)**, 981–993, doi:10.1016/j.jaerosci.2004.03.002, URL `http://linkinghub.elsevier.com/retrieve/pii/S0021850204000308`.

Seinfeld, J. H. and S. N. Pandis, 2006: *Atmospheric Chemistry and Physics : From Air Pollution to Climate Change.* J. Wiley, Hoboken, N.J.

Shao, Y., et al., 2011: Dust cycle: An emerging core theme in Earth system science. *Aeolian Research*, **2 (4)**, 181–204, doi:10.1016/j.aeolia.2011.02.001, URL `http://linkinghub.elsevier.com/retrieve/pii/S1875963711000085`.

Stanelle, T., B. Vogel, H. Vogel, D. Bäumer, and C. Kottmeier, 2010: Feedback between dust particles and atmospheric processes over West Africa during dust episodes in March 2006 and June 2007. *Atmos. Chem. Phys.*, **10 (22)**, 10 771–10 788, doi:10.5194/acp-10-10771-2010, URL `http://www.atmos-chem-phys.net/10/10771/2010/`.

Stith, J. L., et al., 2009: An overview of aircraft observations from the pacific dust experiment campaign. *J. Geophys. Res.*, **114 (D5)**, doi:10.1029/2008JD010924, URL `http://www.agu.org/pubs/crossref/2009/2008JD010924.shtml`.

Sullivan, R. C., et al., 2010: Irreversible loss of ice nucleation active sites in mineral dust particles caused by sulphuric acid condensation. *Atmos. Chem. Phys.*, **10 (23)**, 11 471–11 487, doi:10.5194/acp-10-11471-2010, URL `http://www.atmos-chem-phys.net/10/11471/2010/`.

Targino, A. C., R. Krejci, K. J. Noone, and P. Glantz, 2006: Single particle analysis of ice crystal residuals observed in orographic wave clouds over Scandinavia during INTACC experiment. *Atmos. Chem. Phys.*, **6 (7)**, 1977–1990, doi:10.5194/acp-6-1977-2006, URL `http://www.atmos-chem-phys.net/6/1977/2006/`.

Tegen, I., 2003: Modeling the mineral dust aerosol cycle in the climate system. *Quat. Sci. Rev.*, **22 (18-19)**, 1821–1834, doi:10.1016/S0277-3791(03)00163-X, URL `http://linkinghub.elsevier.com/retrieve/pii/S027737910300163X`.

Tegen, I. and I. Fung, 1994: Modeling of mineral dust in the atmosphere: Sources, transport, and optical thickness. *J. Geophys. Res.*, **99 (D11)**, 22 897–22 914, doi:10.1029/94JD01928, URL `http://www.agu.org/pubs/crossref/1994/94JD01928.shtml`.

Twohy, C. H. and M. R. Poellot, 2005: Chemical characteristics of ice residual nuclei in anvil cirrus clouds: evidence for homogeneous and heterogeneous ice formation. *Atmos. Chem. Phys.*, **5 (8)**, 2289–2297, doi:10.5194/acp-5-2289-2005, URL `http://www.atmos-chem-phys.net/5/2289/2005/`.

Twohy, C. H., et al., 2009: Saharan dust particles nucleate droplets in eastern Atlantic clouds. *Geophys. Res. Lett.*, **36 (1)**, doi:10.1029/2008GL035846, URL `http://www.agu.org/pubs/crossref/2009/2008GL035846.shtml`.

Vali, G., 1985: Nucleation terminology. *Bull. Amer. Meteor. Soc.*, **66**, 1426–1427.

Vali, G., 1999: Ice nucleation—Theory. URL `http://www-das.uwyo.edu/~vali/nucl_th.pdf`, NCAR/ASP 1999 Summer Colloquium, URL `http://www-das.uwyo.edu/~vali/nucl_th.pdf`.

Vogel, B., C. Hoose, H. Vogel, and C. Kottmeier, 2006: A model of dust transport applied to the Dead Sea Area. *Meteor. Z.*, **15 (6)**, 611–624, doi:10.

1127/0941-2948/2006/0168, URL `http://openurl.ingenta.com/content/xref?genre=article&issn=0941-2948&volume=15&issue=6&spage=611`.

Vogel, B., H. Vogel, D. Bäumer, M. Bangert, K. Lundgren, R. Rinke, and T. Stanelle, 2009: The comprehensive model system COSMO-ART – Radiative impact of aerosol on the state of the atmosphere on the regional scale. *Atmos. Chem. Phys.*, **9 (22)**, 8661–8680, doi:10.5194/acp-9-8661-2009, URL `http://www.atmos-chem-phys.net/9/8661/2009/`.

Wagner, R., S. Benz, O. Möhler, H. Saathoff, and U. Schurath, 2006: Probing ice clouds by broadband mid-infrared extinction spectroscopy: case studies from ice nucleation experiments in the AIDA aerosol and cloud chamber. *Atmos. Chem. Phys.*, **6 (12)**, 4775–4800, doi:10.5194/acp-6-4775-2006, URL `http://www.atmos-chem-phys.net/6/4775/2006/`.

Welti, A., F. Lüönd, O. Stetzer, and U. Lohmann, 2009: Influence of particle size on the ice nucleating ability of mineral dusts. *Atmos. Chem. Phys.*, **9 (18)**, 6705–6715, doi:10.5194/acp-9-6705-2009, URL `http://www.atmos-chem-phys.net/9/6705/2009/`.

Wiacek, A., T. Peter, and U. Lohmann, 2010: The potential influence of Asian and African mineral dust on ice, mixed-phase and liquid water clouds. *Atmos. Chem. Phys.*, **10 (18)**, 8649–8667, doi:10.5194/acp-10-8649-2010, URL `http://www.atmos-chem-phys.net/10/8649/2010/`.

Young, K. C., 1974: A numerical simulation of wintertime, orographic precipitation: Part I. Description of model microphysics and numerical techniques. *J. Atmos. Sci.*, **31 (7)**, 1735–1748, doi:10.1175/1520-0469(1974)031<1735:ANSOWO>2.0.CO;2, URL `http://journals.ametsoc.org/doi/abs/10.1175/1520-0469%281974%29031%3C1735%3AANSOWO%3E2.0.CO%3B2`.

Yun, Y. and J. E. Penner, 2012: Global model comparison of heterogeneous ice nucleation parameterizations in mixed phase clouds. *J. Geophys. Res.*, **117 (D7)**, doi:10.1029/2011JD016506, URL `http://www.agu.org/pubs/crossref/2012/2011JD016506.shtml`.

Zobrist, B., T. Koop, B. P. Luo, C. Marcolli, and T. Peter, 2007: Heterogeneous ice nucleation rate coefficient of water droplets coated by a nonadecanol mono-

layer. **111 (5)**, 2149–2155, doi:10.1021/jp066080w, URL `http://pubs.acs.org/cgi-bin/doilookup/?10.1021/jp066080w`.

Zobrist, B., C. Marcolli, D. A. Pedernera, and T. Koop, 2008: Do atmospheric aerosols form glasses? *Atmos. Chem. Phys.*, **8 (17)**, 5221–5244, doi:10.5194/acp-8-5221-2008, URL `http://www.atmos-chem-phys.net/8/5221/2008/`.

Zuberi, B., A. K. Bertram, C. A. Cassa, L. T. Molina, and M. J. Molina, 2002: Heterogeneous nucleation of ice in $(NH_4)_2SO_4$-H_2O particles with mineral dust immersions. *Geophys. Res. Lett.*, **29 (10)**, doi:10.1029/2001GL014289, URL `http://www.agu.org/pubs/crossref/2002/2001GL014289.shtml`.

Conferences, Workshops & Contributions

2008

05/2008: **VI-ACI annual meeting in Frankfurt am Main**

10/2008: **VI-ACI workshop in Karlsruhe**

⟶ **Talk:** Pumped Counterflow Virtual Impactor (PCVI) - Experiment setup

2009

02/2009: **SCOUT-O3 workshop in Mainz**

03/2009: **DPG-Frühjahrstagung in Hamburg**

⟶ **Talk**: AIDA-Wolkenkammerexperimente zur heterogenen Eisnukleation in Zirruswolken

04/2009: **VI-ACI annual meeting in Karlsruhe**

⟶ **Talk:** Recent results of ACI02 campaign and a first comparison with MAID model calculations

06/2009: **SCOUT-O3 annual meeting in Schliersee**

⟶ **Poster:** Heterogeneous ice nucleation on mineral dust aerosols - A comparison of laboratory studies with process model calculations

07/2009: **MOCA-09 conference in Montréal**

⟶ **Talk:** The impact of sulfuric acid coatings on the deposition ice nucleation on mineral dust aerosols

08-09/2009: **1st IfT summer-school on Atmospheric Aerosol and Clouds**

09/2009: **EAC conference in Karlsruhe**

⟶ **Poster:** Deposition mode ice nucleation on atmospheric dust aerosols - A comparison of laboratory studies with detailed process model calculations

2010

01/2010: **Residence for research in Manchester**

⟶ ACPIM training

05/2010: **VI-ACI annual meeting in Zurich**

⟶ **Talk:** Heterogeneous ice nucleation on mineral dust aerosols

08-09/2010: **IAC conference in Helsinki**

⟶ **Talk:** Parameterization of immersion freezing on mineral dust particles: An application in a regional scale model

12/2010: **ACI-03 workshop in Karlsruhe**

12/2010: **AGU conference in San Francisco**

⟶ **Poster:** Parameterization of immersion freezing on mineral dust particles: An application in a regional scale model

2011

05/2011: **IN2clouds workshop in Ettlingen**

⟶ **Talk:** Parameterization of immersion freezing on mineral dust particles: An application in a regional scale model

Publications

- Skrotzki, J., P. Connolly, M. Schnaiter, H. Saathoff, O. Möhler, R. Wagner, **M. Niemand**, V. Ebert, and T. Leisner, 2012: The accommodation coefficient of water molecules on ice—cirrus cloud studies at the AIDA simulation chamber. Submitted to *Atmos. Chem. Phys.*

- **Niemand, M.**, M. Möhler, B. Vogel, H. Vogel, C. Hoose, P. Connolly, H. Klein, H. Bingemer, P. DeMott, J. Skrotzki, and T. Leisner, 2012: A particle-surface-area-based parameterization of immersion freezing on mineral dust particles. Accepted for publication in *J. Atmos. Sci.*

- Steinke, I., M. Möhler, A. Kiselev, **M. Niemand**, H. Saathoff, M. Schnaiter, J. Skrotzki, C. Hoose, and T. Leisner, 2011: Ice nucleation properties of fine ash particles from the Eyjafjallajökull eruption in April 2010. *Atmos. Chem. Phys.*, **11 (24)**, 12945–12958

- Murray, B. J., T. W. Wilson, S. Dobbie, Z. Cui, S. M. R. K. Al-Jumur, O. Möhler, M. Schnaiter, R. Wagner, S. Benz, **M. Niemand**, H. Saathoff, V. Ebert, S. Wagner, B. Kärcher, 2010: Heterogeneous nucleation of ice particles on glassy aerosols under cirrus conditions. *Nature Geosci.*, **3 (4)**, 233–237

- Möhlmann, D. T. F., **M. Niemand**, V. Formisano, H. Savijärvi, and P. Wolkenberg, 2009: Fog phenomena on Mars. *Planet. Space Sci.*, **57 (14-15)**, 1987–1992

Acknowledgements